ABSTRACT

GRAPHENE CHANNELS INTERFACED WITH DISTRIBUTED QUANTUM DOTS

by
Xin Miao

Previous research has elucidated the remarkable electrical and optical characteristics of graphene and pointed to the various applications of graphene-based devices. One of such applications is electro-optical graphene-based elements. In this work, the optoelectronic properties of field-effect transistors are explored. These are composed of surface graphene guides, which are interfaced with an array of individual semiconductor quantum dots. The graphene guide also serves as a channel for the field-effect transistor (FET) while the dots provide for fluorescence markers. They may be placed either within the capacitor formed between the graphene and the gate electrode, or on top of the graphene. Electrical characteristics under white light illumination and the device's photoluminescence (PL) properties at various biasing conditions are studied.

The graphene's channel conductivity as a function of gate bias and drain-source bias under illumination are obtained. A minimum in source-drain current signifies the Dirac point. Under a low intensity of white light, the photocurrent changes signs as a function of gate bias, which suggests that the photocurrent may have originated from the graphene channel rather than the QDs. Negative differential photo-conductance is observed under illumination at large negative gate voltages. Changes in the fluorescence are noted as a function of both the drain-source and gate-source potentials. The fluorescence is more pronounced when the incident or the emission wavelengths are coupled to surface modes.

Luminescence lifetimes and linewidths from an array of individual quantum dots (QDs) that are either interfaced with graphene surface guides or dispersed on

aluminum electrodes are studied. The observed fluorescence quenching is consistent with screening by charge carriers. Fluorescence quenching is typically mentioned as a sign that chromophores are interfaced with a conductive surface (metal or graphene). The QDs interfaced with the metal film indeed exhibits shorter lifetime and line-broadening compared to QDs on a dielectric substrates but not necessarily fluorescence quenching; the latter may be impacted by molecular concentration, reflectivity considerations and conductor imperfections.

GRAPHENE CHANNELS INTERFACED WITH DISTRIBUTED QUANTUM DOTS

by
Xin Miao

A Dissertation
Submitted to the Faculty of
New Jersey Institute of Technology
in Partial Fulfillment of the Requirements for the Degree of
Doctor of Philosophy in Electrical Engineering

Helen and John C. Hartmann Department of
Electrical and Computer Engineering

August 2019

APPROVAL PAGE

GRAPHENE CHANNELS INTERFACED WITH DISTRIBUTED QUANTUM DOTS

Xin Miao

Dr. Haim Grebel, Dissertation Advisor Date
Professor of Electrical and Computer Engineering, NJIT

Dr. Leonid Tsybeskov, Committee Member Date
Professor of Electrical and Computer Engineering, NJIT

Dr. Marek Sosnowski, Committee Member Date
Professor of Electrical and Computer Engineering, NJIT

Dr. Bipin Rajendran, Committee Member Date
Associate Professor of Electrical and Computer Engineering, NJIT

Dr. John Federici, Committee Member Date
Distinguished Professor of Physics, NJIT

BIOGRAPHICAL SKETCH

Author: Xin Miao

Degree: Doctor of Philosophy

Date: August 2019

Undergraduate and Graduate Education:

- Doctor of Philosophy in Electrical Engineering,
  New Jersey Institute of Technology, Newark, NJ, 2019
- Master of Science in Electrical Engineering,
  New Jersey Institute of Technology, Newark, NJ, 2013
- Bachelor of Science in Physics,
  University of Science and Technology of China, Hefei, China, 2007

Major: Electrical Engineering

Presentations and Publications:

X. Miao, D. J. Gosztola, A. V. Sumant, and H. Grebel, Lifetime and Linewidth of Individual Quantum Dots Interfaced with Graphene. *Nanoscale*, 10:7040-7046, March 2018.

X. Miao, and H. Grebel, Graphene Channels Interfaced with an Array of Individual Quantum Dots. *Mesoscale and Nanoscale Physics*, arXiv:1705.05910, May 2017.

X. Miao, S. Trivedi, and H. Grebel, Graphene Channels Interfaced with Quantum Dots in Field Effect Transistors: Electrical and Photo-Induced Effects. *MRS Advances*, 1(22), 1597-1603, February 2016.

X. Miao, S. Trivedi, and H. Grebel, Electrical and Photo-Induced Effects in Graphene Channels When Interfaced with Quantum Dots. *MRS Proceedings*, 1727, Mrsf14-1727-k05-08, March 2015.

X. Miao, and H. Grebel. Photo-Induced Effects and Raman Spectrum of Graphene Channels Interfaced with Quantum Dots in Field Effect Transistors. *Poster*, Material Research Society Symposium, Boston, Massachusetts, December 2016.

X. Miao, S. Trivedi, and H. Grebel, Photoelectronic Effects with Graphene Channels Interfaced with Quantum Dots Arrays. *Poster*, ECS Meeting, San Diego, California, June 2016.

X. Miao, S. Trivedi, and H. Grebel, Graphene Channels Interfaced with Quantum Dots in Field Effect Transistors: Electrical and Photo-induced Effects. *Poster*, Material Research Society Symposium, Boston, Massachusetts, December 2015.

X. Miao, S. Trivedi, and H. Grebel. Electrical and Photo-induced Effects in Graphene Channels interfaced with Quantum Dots. *Poster*, Material Research Society Symposium, Boston, Massachusetts, December 2014.

To my family, for their continuous love and support.

ACKNOWLEDGMENT

I would like to express my gratitude to many people for accompanying me through the Ph.D. Completion of my doctoral dissertation would not be possible without their support.

First of all, I am extremely grateful to the valuable guidance of my supervisor, Dr. Haim Grebel, for his continuous support and encouragement through all my graduate work. From the beginning, Dr. Grebel has been providing opportunities, guiding me over the hard times of research and paper writing, but also showing me how to live a happy and healthy life. And most importantly, he set an example for me on how to be a professional in research with a rigorous scientific attitude. Without his encouragement and constant guidance, I could not have finished this dissertation. He has been a wonderful mentor, and it is an honor to have been his student.

I would like to thank Dr. Leonid Tsybeskov, Dr. Marek Sosnowski, Dr. Bipin Rajendran and Dr. John Federici for serving on my committee and taking the time to read the drafts and give feedback on this dissertation. I thank Dr. Roberto Rojas-Cessa for providing me ideas and advice for my simulation project. I thank Dr. David J. Gosztola, Dr. Anirudha V. Sumant from the Argonne National Laboratory for their valuable data of the lifetime measurement.

Thanks to Dr. Tazima S. Chowdhury and all the group members I have worked with for their suggestions and discussions which have contributed to the improvement of my knowledge and research. Also, thanks to my friends and colleagues for the their company.

Thanks to Dr. Samarth Trivedi for the SEM figures. This work was performed, in part, at the Center for Nanoscale Materials, a U.S. Department of Energy Office of Science User Facility, and supported by the U.S. Department of Energy, Office of Science, under Contract No. DE-AC02-06CH11357.

Last, but not least, I would like to thank my parents, Jianhua Miao and Xianghua Meng for their unconditional love and being great models in my life. My thanks to them for giving me the determination to overcome my hesitation in pursuing my dream. Therefore, this work is dedicated to them.

TABLE OF CONTENTS

Chapter **Page**

TABLE OF CONTENTS
(Continued)

Chapter **Page**

LIST OF TABLES

LIST OF FIGURES

LIST OF FIGURES
(Continued)

Figure **Page**

LIST OF FIGURES
(Continued)

Figure **Page**

LIST OF FIGURES
(Continued)

LIST OF FIGURES
(Continued)

Figure **Page**

LIST OF FIGURES
(Continued)

Figure **Page**

CHAPTER 1

INTRODUCTION

1.1 Graphene

Graphene is a monolayer or few layers of graphite, in which the SP^2 hybridized carbon atoms are arranged in a planar, hexagonal pattern [151]. Graphite has a layered structure; within the layer, each carbon atom forms covalent σ bonds with each of the three nearby carbon atoms whose length is 0.142nm. Atoms between two graphitic layers are bonded via van der Waals forces at a distance of 0.335nm. The weak force between layers of graphite makes it possible to isolate a single layer of graphite. Back in 1961, this honeycomb structure in graphite was observed by German scientist Hanns-Peter Boehm under the electron microscope and was coined ”graphene” [110]. In 2004, Professor Andre Geim and Professor Konstantin Novoselov working at the UK's University of Manchester were able to produce monolayer graphene by using cellotape to successively detach layers of graphite to reach a single layer on a substrate. The material sparked much interest due to its potential electronic and chemical applications. Theoretically, a perfect two-dimensional crystal structure can not be stable as a free standing film due to thermal fluctuations instabilities [119]. In a model for a suspended graphene proposed by J.C. Meyers in 2007 [100], the graphene sheet is not perfectly flat but exhibits intrinsic microscopic roughening; the roughness becomes smaller as the stacks number becomes larger. Multi-layer graphene behaves as graphite graphite. The bandgap structure of graphene is highly related to the stack number. Beyond 10 layers of graphene may be considered as a three-dimensional graphite [88]. Only one layer and two layers of graphene are discussed in this dissertation.

1.1.1 Structure and property of graphene

Graphene is exceptionally strong and inert material due to its bond structure [36,110]. The Young's modulus of a free-standing monolayer graphene is approximately 1000 GPa [81], which is 5 times stronger than steel. A single layer of graphene is found to transmit 97.7% of the incident light [106] but the graphene sheet can also work like carbon atomic nets which can stop other large molecules from penetrating through. The atomic symmetry of the graphene lattice makes it easier to conduct electrons and minimize heat during charge transfer. The thermal conductivity of suspended monolayer graphene is in the range of 4.84 to 5.30×10^3 W/mK [6], which is over ten times better than heat conductors, such as copper and silver. The electron mobility of graphene could reach 15,000 $\mathrm{cm}^2/\mathrm{V{\cdot}s}$ at room temperature, which is almost ten times larger than that of silicon. These structural characteristics indicate that the graphene is an excellent conductor and a promising candidate for future electronic devices.

Graphene is semi-metal; namely, neither metal nor a semiconductor [26]. Figure 1.1 shows the hexagonal lattice structure of a single layer graphene. The figure also shows the reciprocal lattice, which represents the Fourier transform of the direct lattice (and known as the k-space).

The band structure of graphene is commonly based on tight-binding model (TB model) [151] through calculations of the coupling energy between nearest and next nearest neighboring atoms. Because the de Broglie relation $p = \hbar k$ (where p is the momentum vector; $\hbar$ is the reduced Plank constant; k is the wave vector), so this reciprocal lattice is essential, and all the electron movement of graphene will be discussed in this space.

In Figure 1.1, if a is the distance between the nearest atoms in the graphene lattice, the primitive lattice vectors $\vec{a_1}$ and $\vec{a_2}$ can be written as:

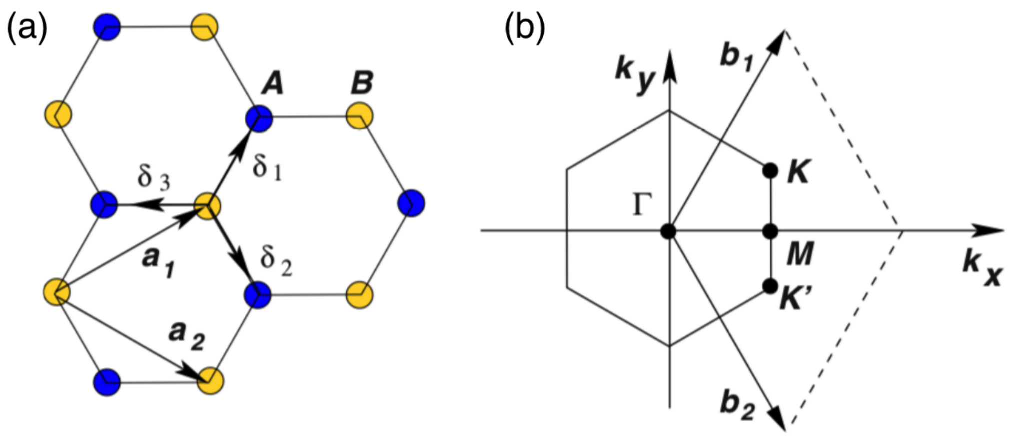

Figure 1.1 Honeycomb lattice and its Brillouin zone. (a) lattice structure of graphene, made out of two interpenetrating triangular lattices (a_1 and a_2 are the lattice unit vector, and δ_i, i=1,2,3 are the nearest neighbor vectors). (b) corresponding Brillouin zone. The Dirac cones are located at the K and K' points.
Source: [109].

$$\vec{a_1} = \frac{a}{2}(3, \sqrt{3}); \vec{a_2} = \frac{a}{2}(3, -\sqrt{3}); \tag{1.1}$$

And the reciprocal lattice vectors are $\vec{b_1}$ and $\vec{b_2}$, where,

$$\vec{b_1} = \frac{2\pi}{3a}(1, \sqrt{3}); \vec{a_2} = \frac{2\pi}{3a}(1, -\sqrt{3}); \tag{1.2}$$

By calculating the energy for an electron hopping to the nearest and next nearest neighbor atoms, the full band structure of graphene is shown in Figure 1.2. A zoom-in view of the figure showed that near the K or K' point (at the corners of the graphene Brillouin zone), which can be called the Dirac point. The K and K' points can be represented by:

$$\vec{K}_1 = \frac{2\pi}{3a}(1, \frac{1}{\sqrt{3}}); \vec{K'} = \frac{2\pi}{3a}(1, -\frac{1}{\sqrt{3}}); \tag{1.3}$$

The energy band diagram can be written as [151]:

$$E_{\pm}(\vec{k}) = \pm t\sqrt{3 + f(\vec{k})} - t' f(\vec{k}) \tag{1.4}$$

where $\vec{k}$ is the reciprocal wavevector, t is the nearest-neighbor coupling energy (hopping between nearby sublattices), and t' is the coupling energy between the next nearest neighbors. And,

$$f(\vec{k}) = 2cos(\sqrt{3}k_{\mathrm{y}}a) + 4cos(\frac{\sqrt{3}}{2}k_{\mathrm{y}}a)cos(\frac{3}{2}k_{\mathrm{x}}a) \tag{1.5}$$

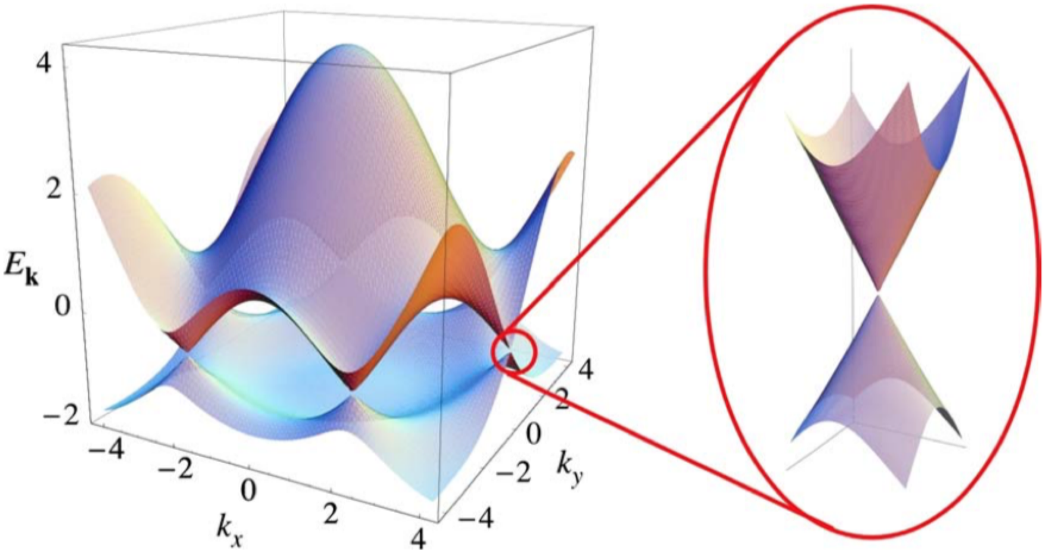

Figure 1.2 Electron dispersion in the honey comb lattice. (a) energy spectrum (in units of t) for finite values of t and t’, with t = 2.7 eV and t’ = - 0.2 t. (b) zoom in of the energy bands close to one of the Dirac points.
Source: [26].

The energy dispersion can be obtained by expanding the Hamiltonian around each of the K and K' points, as $k = K + q$, and assuming $|q| \ll K$, where q is the momentum measured relatively to the Dirac points [151].

$$E_{\pm}(q) = \pm\hbar v_{\mathrm{F}}|q| + O[(q/K)^2] \tag{1.6}$$

So close to the K, K' points, the energy dispersion relation is approximately linear, which means the relation between the momentum and energy is linear, and the velocity of the electron is a constant, does not affect by the momentum or energy. This velocity can be defined as Fermi velocity, v_{F}, with a value $v_{\mathrm{F}} \simeq 1\times10^{6}$m/s.

When analyzing the electron movement in a lattice, the behave of the electron can be converted to electron movement in free space except with a different mass. This mass can be called the effective mass m_{*} and $1/m_{*} \sim d^2E/dk^2$. Because the dispersion relation is linear and symmetric on the zero-energy point, so $E(k)$ is discontinuous at K point and the second derivative is infinite, so the effective mass is zero at this point.

The existence of Dirac points in graphene can also explain the high electron mobility. Based on the quantum tunneling effect, the electron has a probability of passing through a barrier that is higher than its energy. Assume the Dirac electrons scatter to a square potential of width D [70, 71], like shown in Figure 1.3. The transmission through the barrier can be calculated as:

$$T(\phi) \simeq cos^2\phi/(1 - cos^2 D q_{\mathrm{x}} sin^2\phi) \tag{1.7}$$

When $\phi \to 1$, the transmission is 1, which is a manifestation of the Klein paradox [23, 63]. The barriers in graphene are almost entirely transparent, so the holes and electrons have long mean free path, thus very high electron mobility. The electron movement in graphene also limited by the acoustic phonons scattering, which is rather weak and becomes crucial at high applied electric fields.

1.1.2 Fabrication of graphene

The fabrication of high quality, low-cost graphene becomes an urgent topic of research. Multiple methods have been developed since the discovered of graphene:

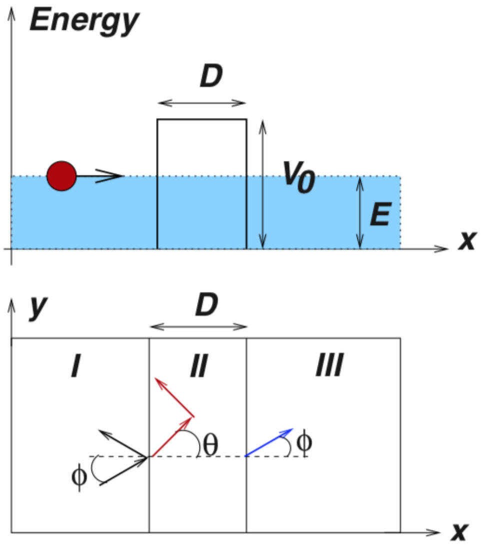

Figure 1.3 Klein tunneling in graphene. Top: schematic of the scattering of Dirac electrons by a square potential. Bottom: definition of the angles ϕ and θ used in the scattering formalism in regions I,II and III.
Source: [26].

Exfoliation The Geim group first isolated graphene from graphite by the exfoliation method [110]. They used a tape to pull small flakes from domes of highly ordered pyrolytic graphite (HOPG) on a substrate. After repeating the process numerous times, they ended up with few-layer graphene (FLG). The thinnest flakes contain one, two or three atomic layers of graphene. This method is easy to implement, and inexpensive, but it is not very efficient. The size of the graphene cannot be controlled and is limited to the crystalline size of the HOPG. The method is inappropriate for a large scale production. Another method is to use chemical exfoliation, which proceeds by treating graphite with acid followed by sonication [2,112]. Graphene can be separated from the solution by centrifugation [60]. A surfactant may be needed in order to prevent the graphene from restacking together. A 'writing' method, takes advantage of the ease at which graphite sheds its layers and followed by sonication at relatively low temperature is also known (our paper and patent). We note that the graphene produced by the exfoliation method has fewer structure defects and high electron mobility [78] and has been adopted for research projects.

Silicon carbide epitaxial growth Graphene can be epitaxially formed by heating silicon carbide (SiC) to a high temperature in vacuum [144]. The bonding in SiC is broken upon heating to over 1000°C under low pressures. The Si atoms was sublimed from the surface and left a layer of C atoms. The graphene grown this way was found to be with optimal band structure [20,113,162] but its resistivity is not as low as the graphene produced by exfoliation [127,132].

Chemical vapor deposition Chemical vapor deposition (CVD) of graphene production is the process of depositing graphene onto a transition metal substrate from carbon-containing gas [47,87,128,156]. When the gas is passing over the heated substrate in the chamber, a reaction occurs, and a layer of graphene is deposited on to the metal surface. The coupling of the graphene to the metal surface is weak and it retains a two-dimensional band structure [40, 41]. Moreover, the process is self-terminating and can support growth of up to two-layer graphene. Methane or acetylene are normally used as carbon source; copper (Cu) [5, 86] and nickel (Ni) [74, 126] are used as transition metals. CVD grown graphene exhibits good quality at relatively low cost and large coverage, so it became a commonly used method for industrial production.

Other techniques There are some other graphene growth techniques, such as, graphene oxide reduction [27], Hydrothermal self-assembly [159], Langmuir-Blodgett method [89], supersonic spray [72] and highly oriented pyrolitic graphite (HOPG) lapping [8]. These methods are not as popular the other methods mentioned earlier.

1.1.3 Characterization of graphene

Graphene was discovered over ten years after the discovery of carbon nanotubes. This may attribute in part to the lack of characterization methods. Unlike other allotrope materials, graphene is only one atom thick and highly transparent. Many measurement tools, such as the optical microscope, scanning electron microscope (SEM), Raman spectroscopy, Atomic force microscope (AFM) and Transmission electron microscopy (TEM) have been used to characterize graphene.

Optical microscope and SEM methods The scanning electron microscopy (SEM) uses a high-energy focused electron beam instead of light to scan the solid sample and collect the signals derived from the electron scattering on the sample surface. The variation of signals can be used to generate an image of the surface and also obtain the information of the morphology and composition of the sample.

Typically, a scanning electron microscopy consists an electron source, electromagnetic lenses, a sample chamber and electron detectors. Electrons are produced from the source, accelerated through a serious of electron lenses and hit on the sample in the vacuum chamber. The position of the electron beam was controlled by coil above the objective lens which allow the beam to scan over the sample surface. Secondary electrons and backscattered electrons are generated from the interactions between the high-energy electron and sample atoms. These signals can be selectively detected by different detectors to form images. Figure 1.4 shows a schematic of the SEM.

Graphene may be directly observed by an optical microscope when it is deposited on 300-nm oxide on Si wafer. The internal reflection between the relatively high refraction coefficients of graphene (n∼2.5) and silicon (n∼3.5). When one layer of graphene is transferred onto a SiO_2 surface, the color contrast between the graphene film and the SiO_2 make it possible to identify the graphene sheet [108]. A total color

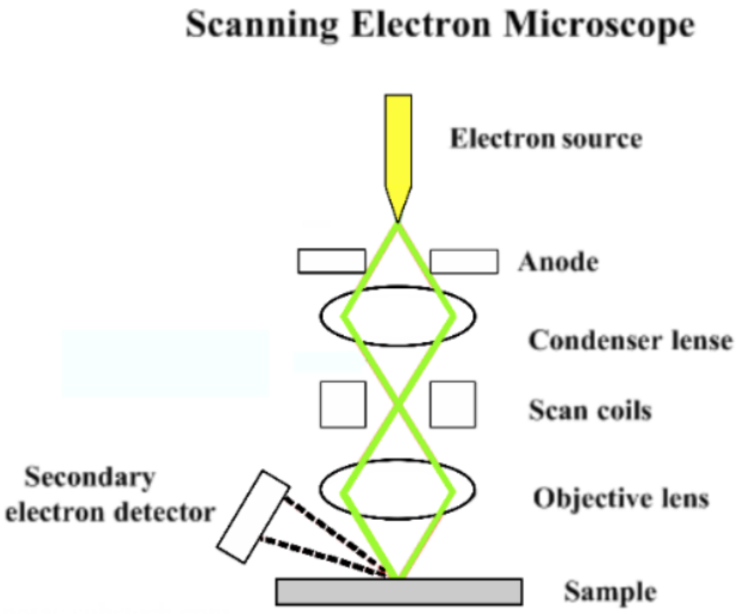

Figure 1.4 Schematic representation of a basic scanning electron microscope.

difference (TCD) method has been developed to characterize large-area graphene samples [43]. The graphene film can also be identified by the color depth on the substrate surface under SEM. Figure 1.5 shows that the thin graphene layer has a larger contrast under SEM and less so under an optical microscope [32].

Raman spectroscopy Raman microscopy is a microscopic imaging technique which is used to characterize the vibrational modes of the molecules. It is based on Raman scattering of monochromatic light. When the incident laser light interacts with the molecule vibrations in the sample, the energy of the laser photons will shift down (Stokes shift) or up (anti-Stokes shift) due to inelastic scattering. As shown in Figure 1.6, in a Stokes Raman scattering process, the photon from the laser excite the molecule in the sample from the initial state to a higher energy state for a short time. When the molecule loses the energy and drop to a state whose energy is higher than the initial state, the scattered photon shifts to a lower frequency (lower energy). In an anti-Stokes process, the molecule drops back to a state whose energy is lower

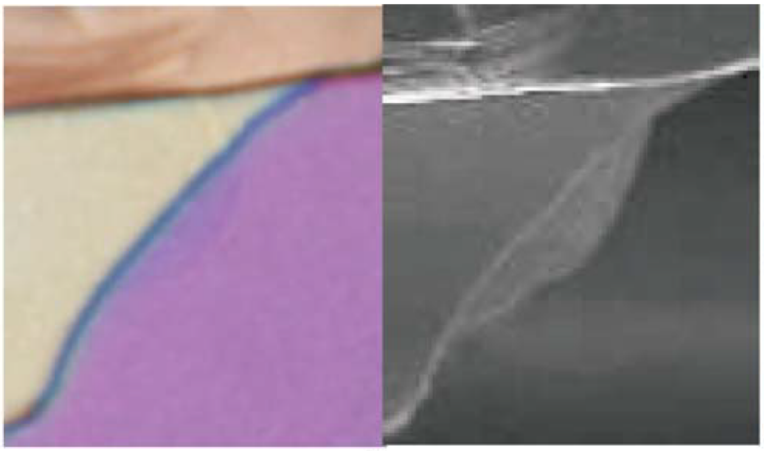

Figure 1.5 Image of a thin graphitic flake in optical (left) and scanning electron microscopes (right). A few-layer graphene is clearly visible in SEM but not with the optical system.
Source: [32].

than the initial state after the excitation. Therefore, the scattered photon is of higher frequency than the incident photon.

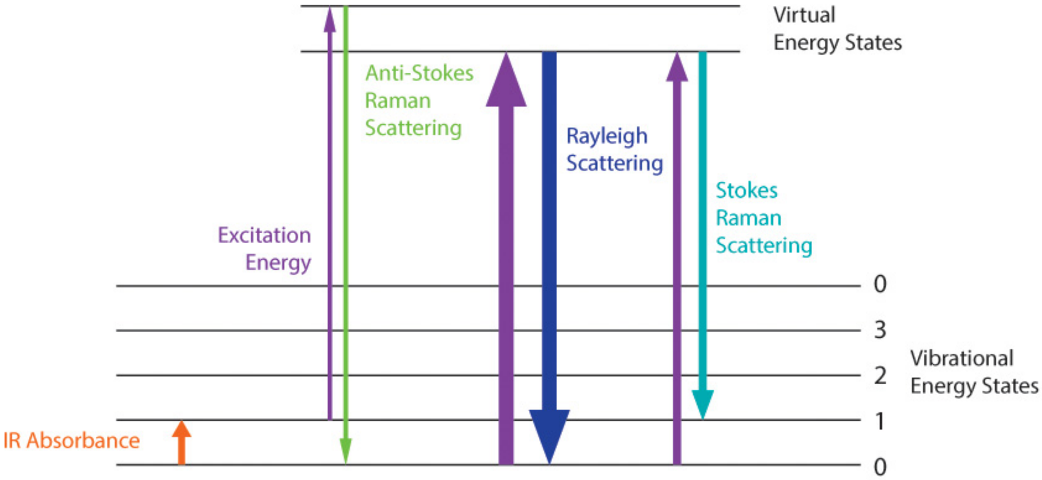

Figure 1.6 Energy-level diagram showing the states involved in Raman spectra.

The Raman microscope usually include an excitation laser, a beam splitter, a bandpass filter, a spectrometer and a charge-coupled detector (CCD). The laser is focused on the sample by a lens system and a beam splitter. Then the laser beam travels through the bandpass filter to make sure that only the desired frequency reaches the sample. Scattered light from the sample is collected through the same lens system. And an edge or a notch filter is used to eliminate the photons close to the incident beam that contribute to Rayleigh scattering. The remaining scattering light is directed into the spectrometer and are captured by a CCD detector for spectral analysis. Figure 1.7 shows a schematic of the SEM.

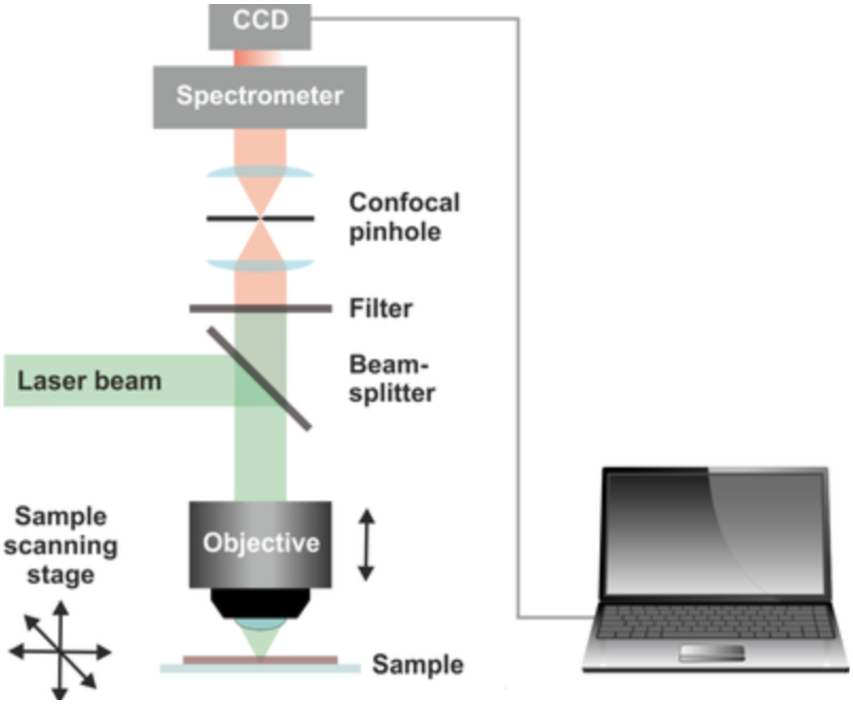

Figure 1.7 Instrument schematic for Raman microscope.

The common features in the Raman spectra of graphite and graphene are the G peak (around 1580 cm^{-1}) and 2D peak (around 2700 cm^{-1}) [155]. The G peak is due to the stretching of the SP^2 bond and the 2D peak is the result of a second order Raman process of the graphitic defect line (typically at ∼1300 cm^{-1}). Monolayer graphene has a lower G peak and the 2D line is twice as intense. Monolayer graphene lacks the graphitic defect line at 1300 cm^{-1}. The shape and position of the 2D peak changes with the number of layers [36, 54]. As shown in Figure 1.8, the intensity of the 2D peak will decrease, and the position of the peak will shift to the higher frequency as the layer number of layers increases. Bi-layer and multi-layer graphene have a much broader 2D peak than a single-layer graphene, yet not as broad as the bulk graphite. Since Raman spectroscopy can easily identifies graphene from other material and detect whether the graphene has a single layer or multi-layer structure, it is a widely used to characterization graphene tool.

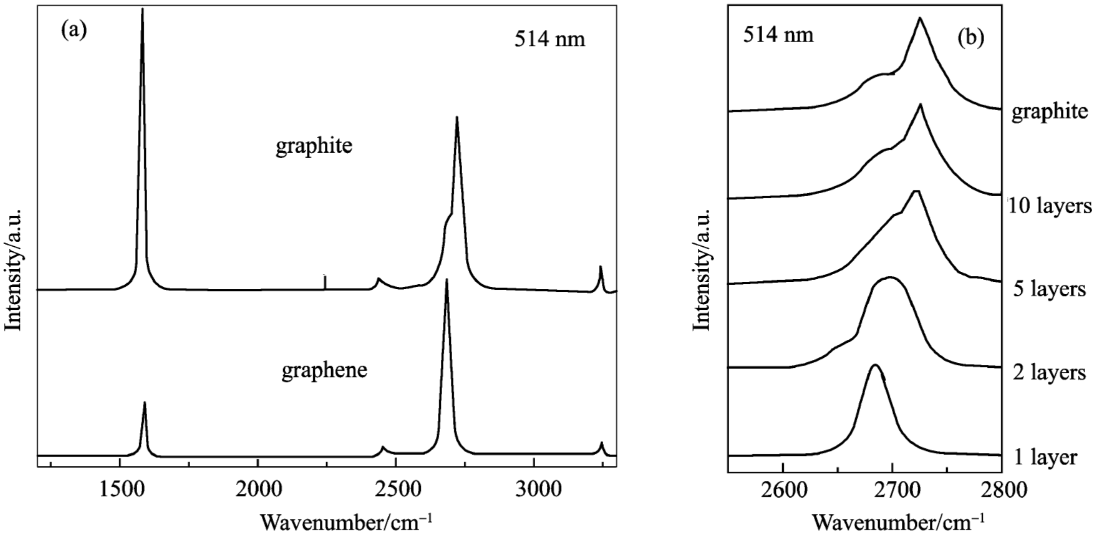

Figure 1.8 (a) Comparison of Raman spectra at 514 nm for bulk graphite and graphene; (b) Evolution of the G' band at 514 nm with the number of layers.
Source: [36].

AFM and TEM Compared to SEM, AFM has much higher resolution, and it is capable to detect nanoscale graphene films [149]. Not only the graphene layer can be detected by measuring the step of graphene edges, but the number of layers may also be estimated from this height measurement. Because the graphene layer thickness under ambient conditions is not ideal 0.335nm, the layer number calculated by AFM is not accurate. In this case, a TEM can estimate the film thickness and hence the number of graphene layers more precisely through observations of the film cross-section [74].

1.1.4 Applications of graphene

Graphene research has substantially impacted industries like medicine, energy, environment and electronics.

Medicine Biosensors have been widely used to detection and diagnosis of diseases at an early stage. graphene-based biosensors are very promising in this field due to the extreme sensitivity, biocompatibility and minimal invasion to biomolecules. The large surface area and the carbon bonds of graphene make it possible to bind drug molecules and achieve drug delivery [107, 134]; High biocompatibility and low toxicity of graphene-based nanomaterials also make it possible to fabricate fast and ultrasensitive biosensors by combining with other biomolecules, like antibodies, enzymes and DNAs (Figure 1.9) [120]. These biomolecules serve as receptors to interact with the target molecules, and the graphene serve as the transducer to convert chemical signals into electrical output. Some aspects of the graphene properties should be considered when designing the graphene biosensors, such as the synthesis methods of graphene, the number of graphene layers and the orientation between the graphene and the biomolecules.

Environment The surface property of graphene makes it an excellent material for processing involving surface reaction or adsorption in the environment field. First, a single-layer graphene possesses two planes available for the interaction to the environment. Second, even though there are no dangling bonds in perfect graphene sheet, it's a great support for anchoring effective chemical functionalities which are responsible for the adsorption of ions. This tunable surface chemistry makes it possible to use graphene-based materials as adsorbents for removal contaminants from aqueous solutions or gas [129, 139]. The delocalized electron clouds of π orbitals obstruct the gap in the hexagonal ring of carbon atoms in graphene, so it can block the passage of the small molecular species, which make graphene a versatile candidate

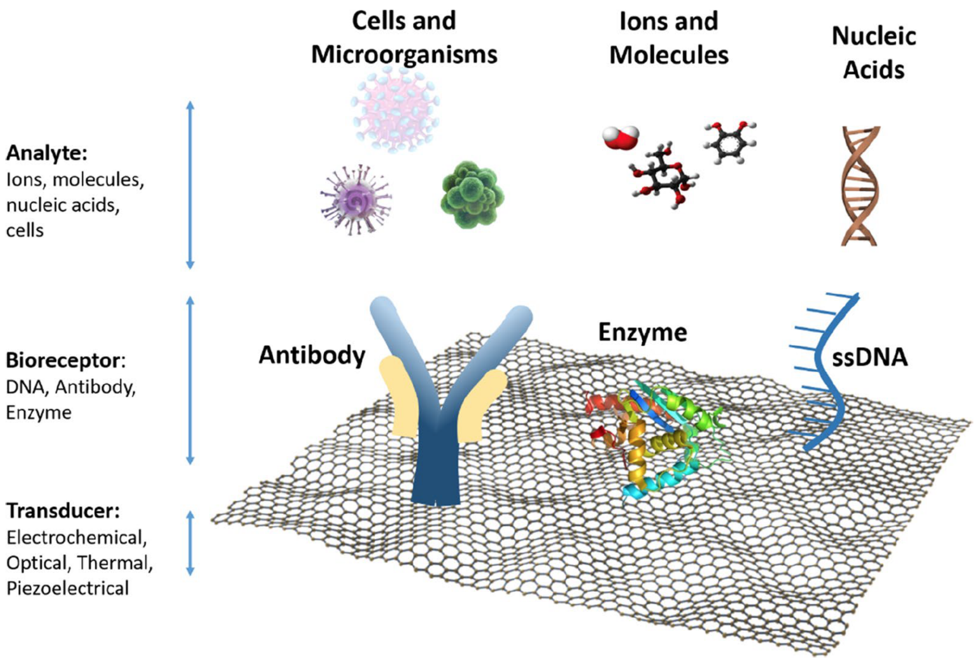

Figure 1.9 Examples of biosensors and components on a graphene platform.
Source: [120].

as a barrier for gas and liquid permeation [17]. The graphene-based membranes can offer a thinner and stronger surface in the fast flow of liquid than aligned carbon nanotube membranes [53]. Examples of graphene-based membranes are shown in Figure 1.10. In addition, owing to the unique electronic properties of graphene, it has been used to develop sensors for the detection of environmental pollutants, like heavy metal ions and toxic gases [135]. The metallic and gas molecule residues on graphene surface can significantly alter the electrical properties. The sensitivity and the limit of detection can be evaluated by measuring the change of the electrical resistance during the exposure of various gas molecules [99].

Energy The unusual size and surface-dependent properties of graphene can significantly enhance the performance of energy conversion devices (e.g. solar cells) and energy storage devices (e.g. supercapacitors and lithium-ion batteries). Single-layer or few-layer graphene sheets with good transparency and low resistance offer a potential

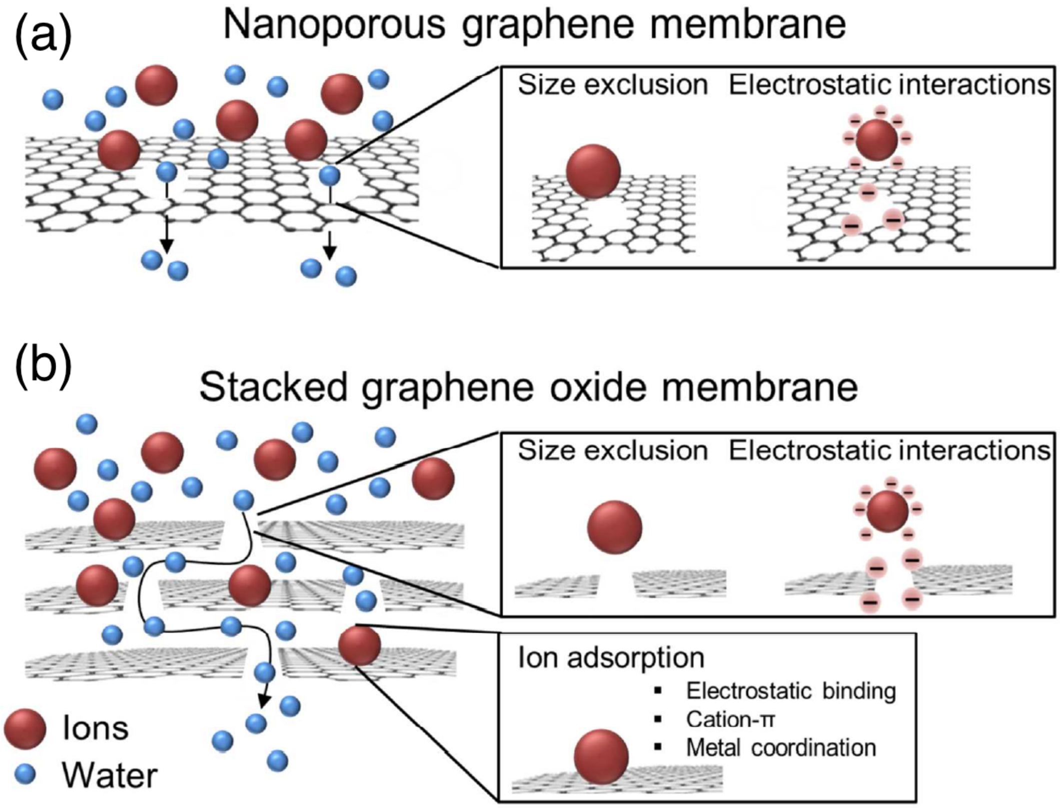

Figure 1.10 Schematic representation of the two types of graphene-based membranes. (a) Nanoporous graphene membranes consist of a single layer of graphene with nanopores of defined pore size. Selectivity is achieved by size exclusion and electrostatic repulsion between charged species and the pores. (b) Membranes composed of stacked GO sheets. In stacked GO membranes, the size of the pores is determined by the interlayer distance between the sheets. In addition to size exclusion and electrostatic interaction, selectivity in stacked GO membranes also results from adsorption of ionic species to the GO sheets.

Source: [121].

alternative for the conventional material used in solar cells. The integration of graphene provides several advantages, like flexibility, environmental compatibility and tunable optical transparency or color. For example, layered graphene grown on a copper foil was reported to replace the ITO transparent electrode in polymer solar cells. The performance of the device can be affected by the concentration of graphene, the annealing time and the annealing temperature [66, 154].

Supercapacitors can store and release energy with high power capability in a short time. Figure 1.11 shows a schematic of the graphene supercapacitor. The capacitance of the device is proportional to the effective surface area of the electrode material. So, graphene is great choice for the supercapacitor electrodes due to its high specific surface area and excellent conductivity [142, 163]. Also, such features of graphene make it a very promising material to be used in lithium-ion batteries which are rechargeable batteries with high energy-storage capacity. The two-dimensional plane of graphene sheet could aid the lithium-ion adsorption and diffusion which means it may help reducing the charging time and increasing the power output of the batteries [117].

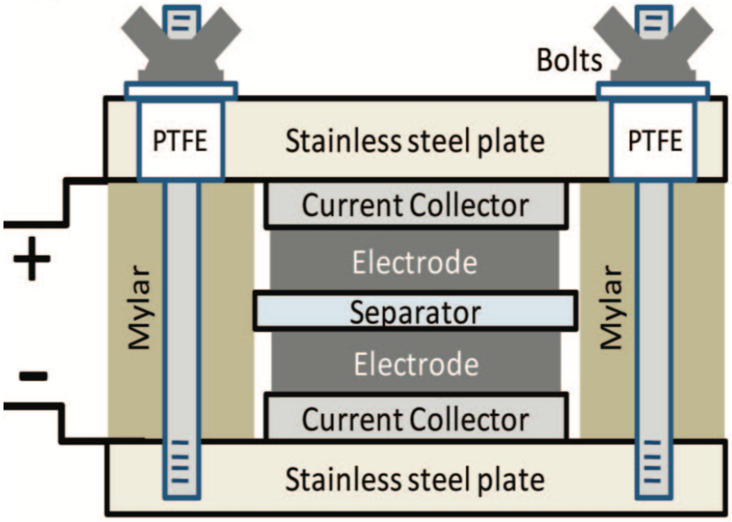

Figure 1.11 Schematic illustration of the graphene based supercapacitor.
Source: [142].

Electronics Due its unique band structure and its extraordinary electric properties, graphene is considered as a possible replacement material for silicon in electronics applications. Table 1.1 showed some of the applications of the graphene electronic devices [109].

Table 1.1 Electronics Applications of Graphene

Application	Drives	Issues to be addressed
Touch screen	Graphene has better endurance than benchmark materials	Requires better control of contact resistance, and the sheet resistance needs to be reduced
E-paper	High transmittance of monolayer graphene could provide visibility	Requires better control of contact resistance
Foldable OLED	Improved efficiency due to graphene's work function tunability; The atomically flat surface of graphene helps to avoid electrical shorts and leakage current	Requires better control of contact resistance, the sheet resistance needs to be reduced
High-frequency transistor	No manufacturable solution for InP high-electron-mobility transistor (low noise) after 2021, according to the 2011 ITRS	Need to achieve current saturation, and $f_T = 850$ GHz, $f_{max} = 1{,}200$ GHz should be achieved
Logic transistor	High mobility	New structures need to resolve the bandgap-mobility trade-off and an higher on/off ratio needs to be achieved

Source: [109]

1.2 Graphene Field Effect Transistor and Graphene Optoelectronic Devices

The basic block of modern electronic devices is the transistor, and in particular, the Field Effect Transistor (FET). Minimization of FET has resulted in performance improvement of integrated circuits; yet, the transistor dimensions approach the scale limit for the material and fabrication integrity. Introducing graphene, the nanoscale material, into the construction of transistors will hopefully break the limitation [73]. Graphene field effect transistor (GFET) is composed of a graphene channel between source and drain electrodes [160]. The one-atom thick graphene can be interfaced with ultra-thin barrier between channel and gate, which would counteract short channel limitations with good carrier mobility.

Similarly, incorporating graphene elements into optoelectronic devices, e.g., photodetectors, can significantly enhance the performance of these devices [95, 152]. because key to improving them is to increase their photocurrent. Due to its considerable mobility, graphene channel may minimize unintentional recombinations.

1.2.1 Field effect transistor

The field effect transistor (FET) is an electronic device using electric field to control the current passing through the channel [102]. It contains a channel and three terminals which are respectively denoted as source, drain, and gate. Charges flow from the source to the drain through the channel, whose conductivity can be modulated through the voltage applied through the gate terminal. Some silicon FET are fabricated with a thin layer of insulator between the gate and the channel, which provides high input impedance. This type of FET is called metal oxide semiconductor FET (MOSFET).

The MOSFET operates in three regions depending on the voltages provided to the device terminals: the cut-off region, the linear region, and the saturation region [42], shown in Figure 1.12. In the cut-off region, the channel current is zero, so the device is in a non-conductive OFF state. In the linear region, the device is turned on, and the channel current is controlled by the gate voltage relative to the source and drain voltages; In the saturation region, the channel current is primarily controlled by the gate bias and barely dependent on upon the drain voltage. There are some key parameters to describe the FET device, such as mobility, on/off ratio and threshold voltage, which can be assessed by the transfer characteristics of the device (i.e., drain-source current (I_{ds}), drain-source voltage (V_{ds}), gate-source voltage (V_{gs})).

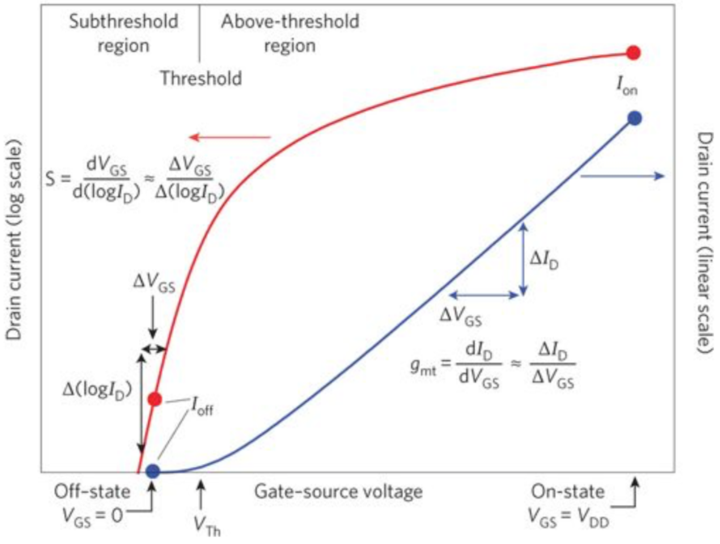

Figure 1.12 MOSFET transfer characteristics showing I_d (on a logarithmic scale on the left and a linear scale on the right) versus the gate-source voltage (V_{gs}).
Source: [136].

Device Mobility The carrier mobility (μ) is the average drift velocity of the charge carriers under the influence of the applied electric field. From the transfer characteristics in the linear region, the mobility can be determined by the formula [147]:

$$\mu = \frac{L}{W C_{\text{ox}} V_{\text{ds}}} \frac{\partial I_{\text{ds}}}{\partial V_{\text{g}}} \tag{1.8}$$

where L and W is the length and the width of the channel respectively, C_{ox} is the capacitance per unit area, and $(1/V_{\text{ds}})(\partial I_{\text{ds}}/\partial V_{\text{g}})$ is the slop of the linear fit of the $I_{\text{ds}} - V_{\text{gs}}$ characteristics.

On/Off ratio The On/Off ratio ($I_{\mathrm{on}}/I_{\mathrm{off}}$) is the ratio between the maximum available source-drain current $\mathrm{I_{ds}}$ at "ON" state and the $\mathrm{I_{ds}}$ at the "OFF" state ($\mathrm{I_{ds}}$ at $\mathrm{V_{gs}}$=0). For the FET, a high $I_{\mathrm{on}}/I_{\mathrm{off}}$ ratio means more stability, higher speed and smaller leakage.

Threshold voltage The threshold voltage ($\mathrm{V_{th}}$) is the minimum gate-source voltage ($\mathrm{V_{gs}}$) that is required to conduct current from the source terminal to the drain terminal. Devices with lower threshold voltage can be turned on with less gate bias and work with less power. The $\mathrm{V_{th}}$ can be determined from x-axis intercept of the linear trend of the $I_{\mathrm{ds}} - V_{\mathrm{gs}}$ characteristics.

1.2.2 Band-gap opening of graphene

The creation of a band-gap in graphene is the basis for these electronic applications of graphene. Generally speaking, electrical materials can be divided into three groups base on their electrical conductivity: conductors, insulators, and semiconductors. In a conductor, the conduction band and the valence band overlap so a fraction of the electrons from valence band can move freely through the material. For an insulator, the conduction band and the valence band are well separated by a large forbidden band-gap $\mathrm{E_g}$ that limits transitions into the conduction band at relatively low temperatures. For semiconductors, the $\mathrm{E_g}$ is relatively small and can be controlled by doping, which makes the conductivity easy to control. The relatively small bandgap of semiconductors makes them very appealing for electronic applications.

As mentioned in Section 1.1.1, graphene is a semi-metal material: neither a metal nor a semiconductor. The band-gap $\mathrm{E_g}$ of graphene is zero, which means the conduction band and valence band touch each other at the Dirac point, where the energy dispersion is linear. Without an energy band-gap, there will no OFF state for logic gates. Pure graphene is limited to only conduction applications, sort of a thin and efficient metal film. A finite energy band-gap should be opened at the Dirac points before it may be put into use. The energy band structure of pure graphene and graphene with a non-zero band-gap are shown in Figure 1.13. Several methods have been created for the band-gap opening in graphene. When graphene was doped with boron nitride (BN) or silicon carbide (SiC), a small band-gap was observed [45]. The doping atoms will alter the graphene conventional crystallographic structure, similar to localized defects. Bilayer graphene possesses a zero-band-gap structure similar to single layer graphene, yet an applied electric field can be used to open a band-gap at the Dirac point [114]. Graphene nanoribbons (GNR) [22], graphene quantum dots [123] have also been used to address this problem.

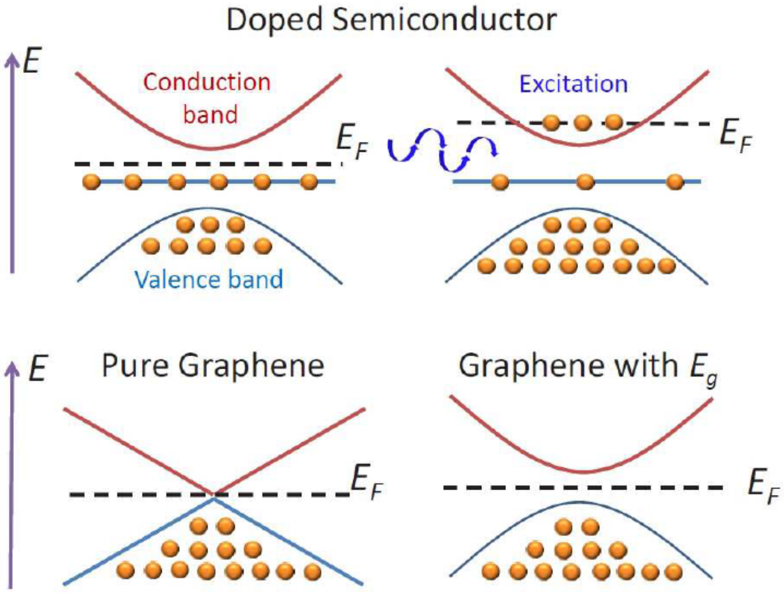

Figure 1.13 The upper half of this figure depicts the electronic band structure of a doped semiconductor. Typically, the band-gap for a doped semiconductor is very small, with only a small energy being required to excite an electron from the valence to conduction band. The lower figure shows the electronic band structure for graphene. For pure samples, no energy band-gap E_g exists. A band gap is possible though through doping or use bias.
Source: [78].

1.2.3 Photonic properties of graphene

Linear and nonlinear optical effects in graphene Graphene exhibits a strong nonlinear optical response over a broad spectral range, which can be observed by nonlinear dynamics of the applied electric field [59]. In general, two types of optical excitations contribute to the process: intraband and interband transitions [46]. An intraband transition refers to a transition between electronic states within the same band while interband band transition is an electronic transition between conduction and valence bands. When the energy of the incident photon $h\nu$ is less than $2E_{\mathrm{F}}$ (E_{F} is the graphene's Fermi energy), the intraband transitions dominate the absorption process. Excitations at high-frequency conditions ($h\nu > 2E_{\mathrm{F}}$), the carriers will undergo interband transitions. There are no intraband transitions in intrinsic graphene. Doping will shift the Fermi level and will alter its frequency response.

Typically, the optical response of a material scales linearly with the incident radiation field. Yet, some materials exhibit a nonlinear optical behavior. When the electric field of the incident light interacts with the electrons in the carbon atoms, it will displace the electron cloud and create a polarized moment in the lattice. The displacement D can be written as:

$$D = \epsilon_0 \epsilon_{\mathrm{r}} E = \epsilon_0 E + P(E) \tag{1.9}$$

where, ϵ_0 is the electric permittivity of free space, ϵ_{r} is the relative permittivity. E is the applied electric field, and $P(E)$ is the polarization. The polarization response $P(E)$ also can be written as:

$$P(E) = \epsilon_0 \sum_{j=1}^{\infty} \chi^{(j)} (E)^j = \epsilon_0 \chi^{(1)} E + \epsilon_0 \chi^{(2)} E^2 + \epsilon_0 \chi^{(3)} E^3 + ... \tag{1.10}$$

where, $\chi^{(j)}$ is the dielectric susceptibility of the j-th order correction, and $(E)^j$ is the j-th power of E. In the linear optics region, the relationship between the polarization

P and the applied field E is linear, $P = \epsilon_0 \chi^{(1)} E$. The first-order susceptibility $\chi^{(1)}$ describes the excitation by a single photon, and can also be expressed as a real part $\chi^{(1)R}$ and imaginary part $\chi^{(1)I}$. Then the relative dielectric constant $\epsilon_{\mathrm{r}} = 1 + \chi^{(1)R}$, optical refractive index n is determined by the real part of first-order susceptibility, $n \approx \sqrt{\epsilon_{\mathrm{r}}} = \sqrt{1 + \chi^{(1)R}}$.

The second-order susceptibility $\chi^{(2)}$ is very small in graphene due to its symmetric lattice structure. Specifically, because the unit cell of graphene is center-symmetric, the second-order optical excited current will cancel each other with opposite momenta. On the other hand, if interface effects break the inversion symmetry, nonuniformity of optical field, or the presence of DC component [30] may allow second-order effects.

The third-order susceptibility $\chi^{(3)}$ is the major contributor to the nonlinear response of graphene [9, 98]. Considering a zero-temperature perturbative calculation at the independent particle level, the third-order effective bulk susceptibility ${\chi_{\mathrm{eff}}}^{(3)}$ can be written as:

$$ {\chi_{\mathrm{eff}}}^{(3)}(\omega_1, \omega_2, \omega_3) = \sigma^{(3)}(\omega_1, \omega_2, \omega_3) / (-i \omega_{\mathrm{t}} \epsilon_0 d_{\mathrm{gr}}) \tag{1.11} $$

where $\omega_{\mathrm{t}} = \omega_1 + \omega_2 + \omega_3$, $\omega_1, \omega_2, \omega_3$ are the incident frequencies, $\sigma^{(3)}(\omega_1, \omega_2, \omega_3)$ is the third order conductivity and $d_{\mathrm{gr}} \approx 0.33nm$ is the effective thickness of single layer graphene. For pure graphene, the third order conductivity can be written as:

$$ \sigma^{(3)}(\omega_1, \omega_2, \omega_3) = \frac{\sigma_0 (\hbar \nu_{\mathrm{F}} e)^2}{\hbar^4 (\omega_1 + \omega_2)(\omega_2 + \omega_3)(\omega_3 + \omega_1)\omega_{\mathrm{t}}} \tag{1.12} $$

where $\nu_{\mathrm{F}} \approx c/300$ is the Fermi velocity and $\sigma_0 = e^2/4\hbar$ is the universal conductivity. The third order nonlinearities in graphene have been experimentally proved, and it is responsible for many nonlinear phenomena in like saturable absorption, self-focusing and nonlinear refractive index change [9,12].

Surface plasmons Surface plasmons (SPs) in graphene are collective oscillations of charges and photons or phonons propagating at the surface of the graphene to form the composite particles of surface plasmon polaritons (SPP) [64], as shown in Figure 1.14. Similar to traditional plasmonic materials (such as, copper, silver, and gold), graphene is considered as a plasmonic waveguide at infrared and terahertz frequencies [131,146].

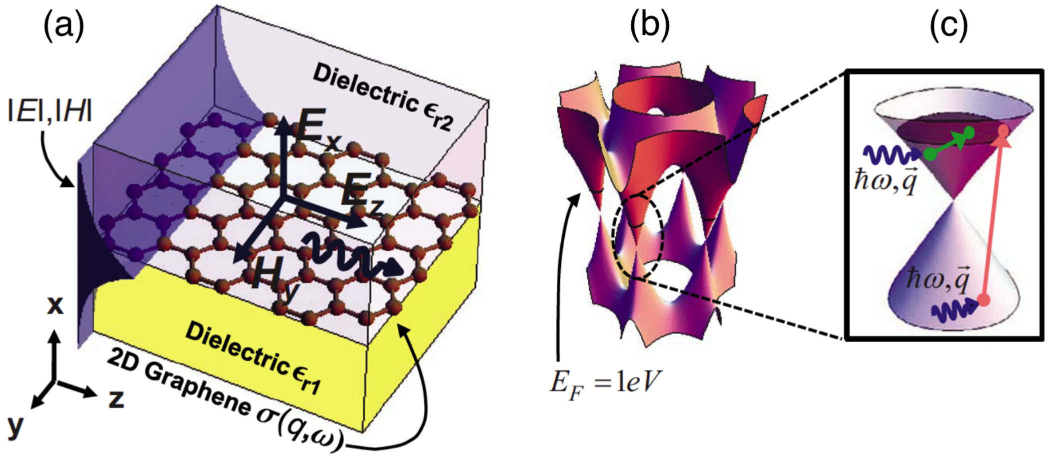

Figure 1.14 (a) Schematic of the graphene system and transverse magnetic (TM) plasmon modes. Note that the profile of the fields looks the same as the fields of an SP. (b) Electronic band structure of graphene; to indicate the vertical scale we show the Fermi energy level for the case E_{F} =1eV. (c) Sketch of the intraband (green arrows) and interband (red arrows) single particle excitations that can lead to large losses; these losses can be avoided by implementing a sufficiently high doping.
Source: [64].

Due to its two-dimensional structure, the surface plasmon excited in graphene is confined more tightly to the surface than the other plasmonic materials. The SPPs on the graphene surface has a long lifetime reaching hundreds of optical cycles and low losses during propagation, which is a remarkable advantage compared with noble-metal plasmonics [77]. Also, the propagation of SP in graphene depends on the incident frequency, chemical potential and relaxation time of excited electrons. The plasmonic frequency ω_{SPP} is proportional to the square root of the Fermi level of graphene: $\omega_{\mathrm{SPP}} \propto \sqrt{E_{\mathrm{F}}} \propto n^{\frac{1}{4}}$. Where n is the carrier density of graphene. So the SPPs can be easily controlled by changing the carrier densities in graphene by electrical gating and chemical doping.

Because there is no intraband transmission in pristine graphene (the valence band is filled and the conduction band is empty), graphene with larger chemical potential (i.e., doped graphene) has a much stronger plasmonic effect than pristine graphene. Compare to pristine graphene, chemical doping can increase the carrier density of graphene and reduce the plasmon damping rate. In graphene, the SPP wavelength λ_{SPP} is much smaller than the incident wavelength λ_{in} with the ratio $\lambda_{\mathrm{in}}/\lambda_{\mathrm{SPP}}$ of approximately 10 to 100 times smaller, which indicates that the SPP wave is confined. For SPP propagating along a highly doped graphene with wave vector $k_{\mathrm{sp}} \approx i(\varepsilon+1)\omega/4\pi\sigma$, the dispersion relation can be written as:

$$k_{\mathrm{sp}} \approx (\hbar^2/4e^2E_{\mathrm{F}})(\varepsilon+1)\omega(\omega+i/\pi) \tag{1.13}$$

where ω is the radial frequency, σ is the energy conductivity, ε is the effective dielectric constant. Therefore, the ratio of the wavelength of SP λ_{sp} to free-space-light wavelength λ_0 can be written as:

$$\lambda_{\mathrm{sp}}/\lambda_0 \approx [4\alpha/(\varepsilon+1)](E_{\mathrm{F}}/\hbar\omega) \tag{1.14}$$

where $\alpha = e^2/\hbar c \approx 1/137$ is the fine structure constant of graphene. It is clear that the SPs in graphene can be tuned by the dielectric constant.

1.2.4 Graphene field effect transistor

Field effect transistor is an electronic device in which the gate terminal controls the current flow in a conductive channel between the source and the drain terminals via an electric field. In graphene field-effect transistors (GFETs) the typical semi-conductive channel is replaced by the graphene. [153]. The basic structure of GFETs is shown in Fig 1.15.

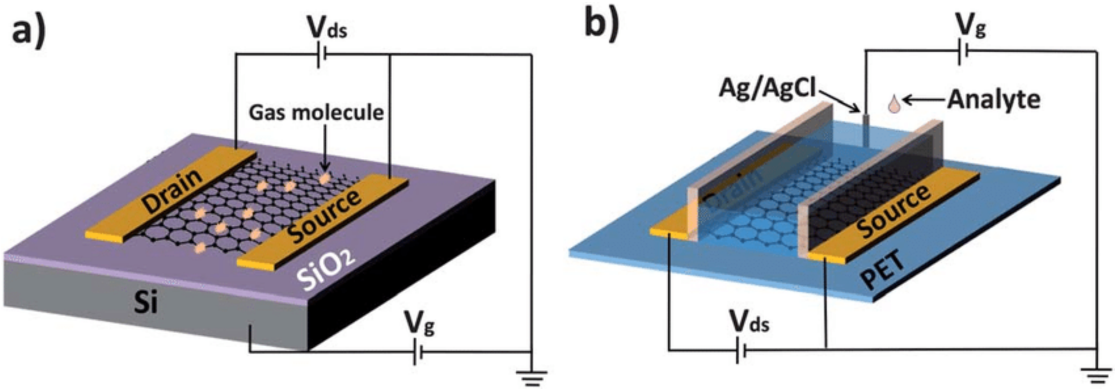

Figure 1.15 (a) Typical back-gate GFET on Si/SiO_2 substrate used as gas sensor. (b) Typical solution-gate GFET on flexible polyethylene terephthalate (PET) substrate used as chemical and biological sensor in aqueous solution.
Source: [58].

Current-Voltage characteristics Graphene is ambipolar: the graphene channel can be tuned continuously between electrons and holes by the gate voltage. For an ideal graphene FET, the Fermi level is at the Dirac point when the gate voltage (V_g) is zero [153], as shown in Figure 1.16. At this time, the conductivity of the channel is at the minimum. When the gate voltage is negative, holes are induced and the Fermi level of the graphene channel moves to the valence band. When the gate voltage is positive, the Fermi level moves to the conduction band and the majority carrier become electrons. Depending on the gate bias, the graphene channel can provide both n-type and p-type performance. The transfer characteristics of the GFET exhibit a V-shape curve, which is a feature of an ambipolar FETs. During the fabrication of the transistor, graphene may absorb carboxyl groups from the environment which act as dopants shift the Fermi level to the valence band and hence the Dirac point to the positive gate range [110, 147].

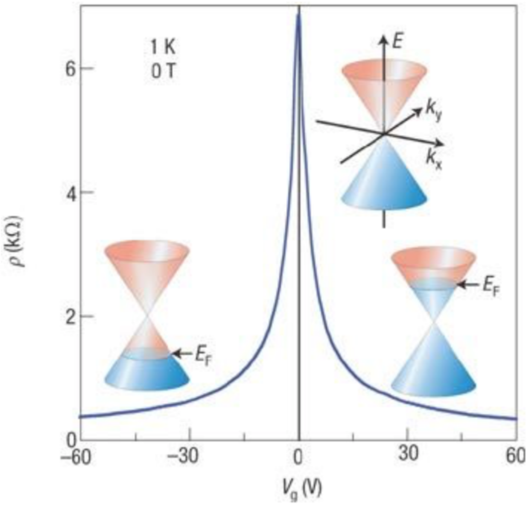

Figure 1.16 Ambipolar electric field effect in single layer graphene. It shows the low-energy spectrum, indicating changes in the position of the Fermi energy with changing gate voltage.
Source: [44].

Advantages The GFETs have many advantages over conventional bulk semiconductor transistors. For a three-dimensional bulk semiconductor device, the penetration depth of the electric field which is generated by the gate is limited. This will affect the response of the transistor. In GFET, the penetration field depth covers the entire monolayer channel, thus detection of molecules will create a large effect. The response will be immediate due to the large graphene's mobility. In general, graphene has fewer surface defects than the thin silicon channels because it is a perfect crystal and thus less false positive readouts [136].

Graphene may be grown by CVD techniques. After transfer onto the oxide of a silicon wafer, the remain of the GFET is defined photolithographically. Integration is made by using process common to the semiconductor industry [91, 93]. GFETs are used as biosensors, chemical sensors, gas sensors, and high-frequency communication devices.

1.2.5 Graphene optoelectronic devices

The extraordinary electronic and photonic properties of graphene make it a great candidate for varies optoelectronic applications, such as photodetector [158], optical modulator [95], mode-locked laser [140] and optical polarizer [13].

A photodetector absorbs photons and converts the energy into electrical current. Compared with the semiconductor photodetectors which suffer from narrow detecting spectral ranges, graphene-based photodetector covers the ultraviolet to far-infrared spectra. The high-speed carrier dynamics in graphene makes the graphene photodetectors very appealing to ultrafast applications.

Graphene is candidate for optical modulators. These modulators transform electrical signals into optical waves. The properties of the light generated from the modulator can be modified by doping or tuning of the incident wave. The wide absorption bandwidth and the tunability of the Fermi level enable graphene applications, such as optical modulators. The graphene optical modulators provide a high optical modulation index comparing to conventional modulators [137].

Graphene may serve as an optical polarizer. Graphene can selectively support electromagnetic modes depending on Fermi level and incident energy, thus transforming unpolarized incident light into polarized light, and the structure and high refractive index can trap the light inside the waveguide. Besides, unlike bulk materials, the two-dimensional nature of graphene allows the fabrication of an in-line fiber polarizer (shown in Figure 1.17).

The high transmittance, high carrier mobility, broadband optical opacity and tunable conductivity properties of graphene make it the most promising material for the future optoelectronic academic researches and industrial innovations.

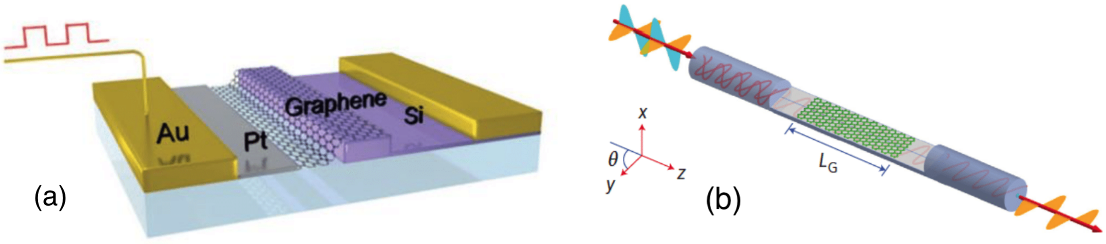

Figure 1.17 (a) Three-dimension schematic illustration of a electroabsorption modulator. a monolayer graphene sheet is on top of a silicon bus waveguide, separated from it by a 7-nm-thick Al_2O_3 layer (not shown). The silicon waveguide is doped and connected to the electrode through a thin layer of silicon defined by selective etching (Figure from [95]). (b) Schematic model of fibre-to-graphene coupler based on a side-polished optical fibre. L_G, propagation distance (length of covered graphene film). Polarization angle θ is defined as the angle between the polarization direction of the analyser.
Source: [13].

1.3 Quantum Dots

1.3.1 Quantum confinement in QDs

Quantum dots (QDs) are nanoscale crystals of semiconductor with the diameter in the range of 2-100 nanometers. They display a unique optical and electronic properties that between bulk semiconductors and atoms or molecules. This is the result of the quantum confinement of carriers [4,133]. These properties of QDs can be modified by changing the chemical composition, size, shape and surface functionalization of the individual QDs [105].

Theoretically, the QDs can be considered as a zero-dimensional entity. When the semiconductor absorbs a photon, whose energy is larger than the bandgap, a quasi-free electron-hole (e-h) pair, or an exciton will be generated. Quantum confinement in QDs means that the size of semiconductor dot is smaller than the exciton's Bohr radius, or the average size of the electron-hole pair. According to Pauli's exclusion principle, the energy levels of the electrons are quantized and depend on the size of the dot. The density of states (DOS) or the number of energy states at a given energy at zero-dimension confinement can be described as:

$$g_{\mathrm{QD}}(E) = \sum_{n,m,l} \delta(E - E_{\mathrm{n}} - E_{\mathrm{m}} - E_{\mathrm{l}}), n, m, l = 1, 2, 3, ... \tag{1.15}$$

The bandgap and the spacing of the energy levels increases as the size of the quantum dot decreases, as shown in Figure 1.18. Absorbance and emission spectrums are blue shifted with decreasing particle size.

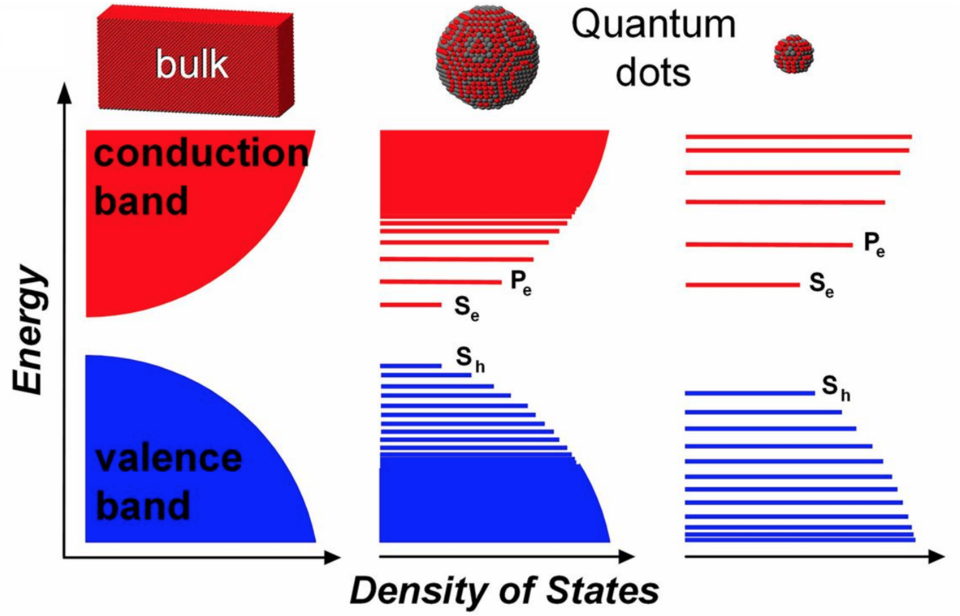

Figure 1.18 Evolution of the electronic structure of inorganic semiconductors from bulk material to QDs of different sizes.
Source: [68].

1.3.2 Fluorescence of QDs

The most obvious properties of QDs is fluorescence, in which excitation of an e-h pair is typically made with a more energetic photon than the photon emitted upon their recombination [79]. Fluorescence can be described by Jablonski diagram (Figure 1.19).

Unlike the bulk semiconductor state, the emission wavelength of QDs is not only dependent on the chemical composition but also on the size and shape of the dot [21, 34]. Smaller QDs posse a larger bandgap which means it requires more

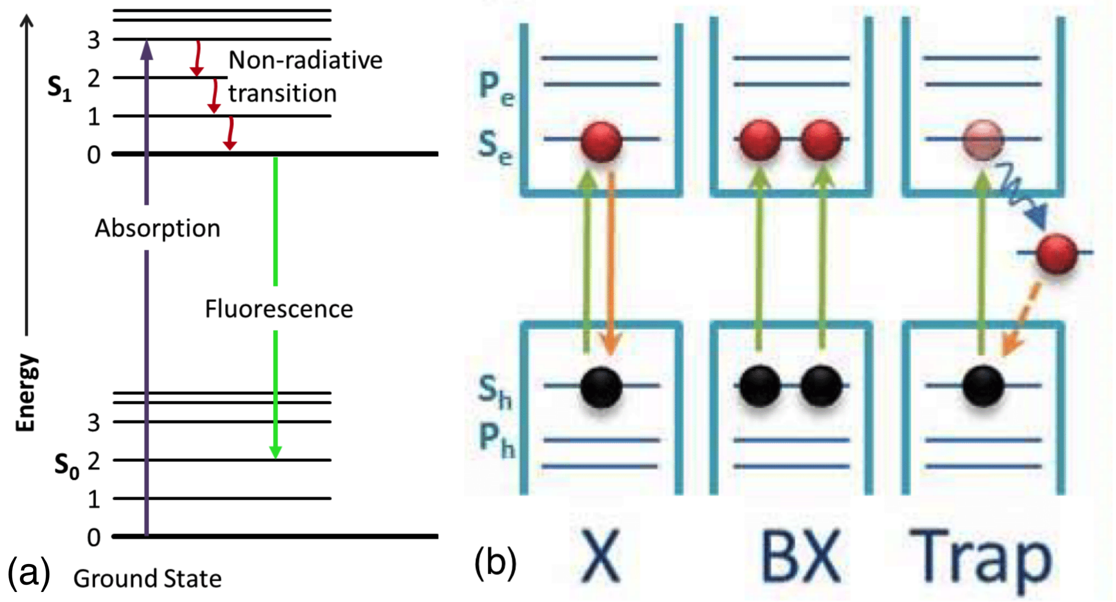

Figure 1.19 (a) Jablonski diagram. After an electron absorbs a high-energy photon the system is excited electronically. The system relaxes vibrationally, and eventually fluoresces at a longer wavelength. (b) Schematic of absorption and emission processes in QDs. From left to right: band-edge absorption and emission of a single exciton (X); sequential absorption of two photons in resonance with the bandgap energy for the formation of a biexciton (BX); nonradiative decay of an electron into a mid-gap trap state followed by trap-to-band recombination (Trap).

Source: [68].

energy to excite an electron to higher energy state and concurrently more energy will be released when the particle return to the ground state. The phenomenon makes it possible to modify the emission colors of QDs just by tuning the dot size during manufacturing. The strong quantum and dielectric confinement in QDs enhance the band-to-band transitions and creating single excitons or multiple excitons. Because the quantization of the electronic states in QDs, the emission illumination from the electron-hole recombination is nearly monochromatic [116]. However, the dangling bonds on the relatively large area surface of QDs can create mid-gap states in the bandgap, which may cause band-edge recombination. Covering a semiconductor core of QD with another epitaxial shell with higher bandgap to form a core-shell structure QD is a solution to this problem.

Compared with conventional organic fluorophores, the QDs have a broader excitation spectrum and a narrower emission peak [1, 28]. This allows a single light source to simultaneously excite multicolor QDs. QDs have a larger emission intensity and stability than organic dyes. They have been reported to be 10-20 times brighter [104] and up to 100 times more stable [7] than convention dyes. The large Stoke shift of QDs reduces the auto fluorescence thus increasing the sensitivity to absorption of light [38].

1.3.3 Manufacturing methods of QDs and their potential applications

Based on production methods, QDs can be categorized into several types.

Colloidal QDs are commonly made of II-VI, III-V, and IV-VI semiconductors by wet chemical synthesis [105, 145]. Precursors are decomposed into monomers in a heated solution following by crystallization. The method is low cost, less toxic and can create large batches of QDs. QDs with two layers, also called core-shell dots may be made by this method.

Epitaxial growth is another method of producing QDs. A semiconductor substrate acts as the seed crystal. Lattice strain between a deposited film and the substrate results in islands, which are subsequently buried to form the QDs [48]. This method can be used to fabricate QD films and core-shell QDs but is limited by cost. One cannot control the position of the QDs.

QD may also be made by lithographically patterned gate electrodes [19]. An external voltage at the electrodes is used to confine these lateral quantum dots. It is hard to produce commercial QDs by this method and its use is limited to research labs.

The electronic and optical tunability of QDs make them very appealing for various applications.

In biomedical applications, QDs are an attractive alternative to the conventional fluorophores or biomarkers. In the fluorescent biosensors or medical imaging, QDs can provide brighter and more stable fluorescence signal than traditional organic dyes [101]. QDs have a good bio-conjugation with ligands, e.g., antibodies used extensively for biosensors [33, 35].

Quantum dots have tunable spectrum and high extinction coefficients, so it is also a proper material for photovoltaic devices. The absorption of one high energy photon can generate more than one exciton. In most current photovoltaic cells, the single exciton transition is resulting in one e-h pair while the rest of the energy is lost as heat [111]. Quantum dot solar cells may lead to more efficient light harvesting and energy conversion due to this multi-photon effect [69].

The QD light emitting diodes (LEDs) and laser diodes offer high color purity and durability due to the relative narrow emission [24,143]. The wavelength of the QD LEDs can be easily tuned over the entire visible wavelength, even in the near-infrared by changing the size of the particles [3].

1.4 Scientific Goals

There is still a long way to go before graphene could be used as a practical replacement for silicon. The lattice structure makes graphene an excellent electronic conductor. But, the suppression of reflection at potential barriers (the Klein tunneling effect) make the charge carriers unstoppable. Currently, the ON/OFF ratio for graphene field effect transistors is less than 10, much less than the ideal ratio of $\sim 10^3$ at room temperature for silicon devices [57, 94]. The absence of a bandgap also complicates the use of graphene as an effective field effect transistor.

To improve performances of graphene-based transistors, opening an energy bandgap in the graphene is a good option. As discussed in Section 1.2.2, a bandgap could be accomplished by inducing quantum confinement in the graphene. The graphene nanoribbons behave more like semiconductors, rather than large-area graphene sheet [56, 141]. Biased bilayer graphene will also have bandgap tunability [25, 115].

Graphene based opto-electronic device may place graphene in contact with light absorbing material as a carrier extractor. Quantum dot film may be used for that purpose. Such core/shell QDs in contact with graphene is shown in Figure 1.20. Since the graphene is all but a surface, an interface with the QDs makes a tremendous impact on its conductivity and its light response. Surface plasmons polaritons (SPP) are charge waves at the vicinity of the conductor/dielectric interface. The electric field decays exponentially away from the surface. Such a high concentration of field may interact strongly with QD at the interface [11, 84, 85].

This research is mainly focused on the graphene channels interfaced with an array of semiconductor quantum dots under irradiation of light. Specific research goals of this dissertation are presented in the following:

- To study the electrical characteristics of the graphene channel under different illumination.

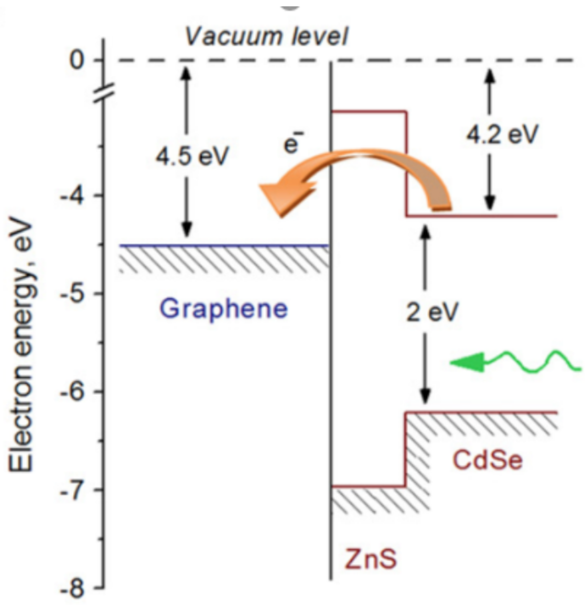

Figure 1.20 Energy level diagram of CdSe/ZnS quantum dots in contact with single layer graphene.
Source: [75].

- To study the interaction between the graphene and the quantum dot with surface plasmon.
- To answer whether this graphene device operation be different from the old graphene photodetector.

CHAPTER 2

EXPERIMENT AND METHODS

2.1 Sample Preparation

2.1.1 Graphene production and transfer

The main methods of graphene production include mechanical exfoliation, liquid-phase exfoliation, chemical vapor deposition (CVD), synthesis on SiC, etc. In our research, graphene was produced on a copper (Cu) substrate using CVD and coated with Poly (methyl methacrylate) (PMMA) as a transfer medium to an alternate substrate [90].

CVD synthesis of graphene The graphene was grown on one side or both sides of the 25μm thick polycrystalline copper foils. First, the bare copper foil was annealed in flowing hydrogen atmosphere at 1000 °C to increase the grain size of the Cu in a tube reactor. After the annealing, graphene is grown on the copper foil by adding methane as a carbon source, with flow rate of 50 standard cc per minute at 1 Torr for a few minutes. After the growth, the furnace is cooled from the growth temperature to room temperature in flowing hydrogen atmosphere at 300 Torr.

Transfer of graphene The CVD graphene on Cu was transferred using polymer assisted transfer method (shown in Figure 2.1). The graphene-deposited Cu substrate is typically coated with a thin layer of polymer to protect it through the transfer stages. A 150nm thick poly (methyl methacrylate) (PMMA, 75,000 molecular weight, 15-20 wt% in toluene) was spin-coated on the graphene film at 2500rpm for 30 seconds. The Cu/graphene/PMMA foil was baked at 180°C on a hot plate for over 2 mins to improve adhesion between the graphene and PMMA. In order to remove the Cu foil, the film was floating in a bath of Ferric Chloride solution for 45 mins. The graphene coated PMMA was scooped up and immersed in deionized (DI) water for 15 minutes while replacing the water 3 times to remove the residual copper etchant. The target substrate was cleaned with acetone, methanol and isopropyl alcohol (IPA) for 30 mins and dried up. Subsequently, the graphene/PMMA film was scooped up from the DI water with the target substrate and dried up in the room temperature for 24 hours. The PMMA layer was removed by immersing it in acetone at 40°C for 20 mins or Anisole at room temperature for 30 mins.

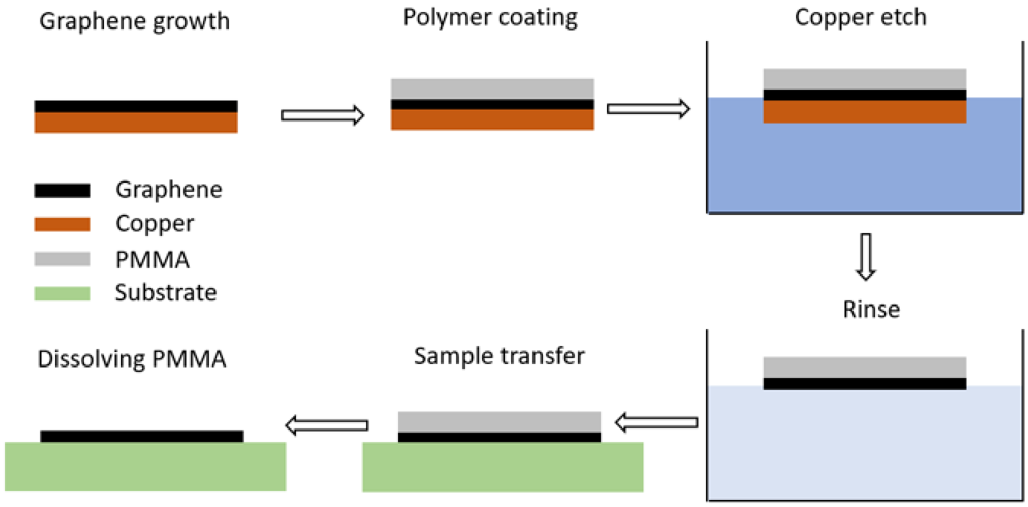

Figure 2.1 Schematic diagram of graphene transfer based on PMMA technique.

Characterization The Raman spectra of the graphene was taken using the Thermo Fisher DXRxi Raman imaging microscope. The graphene film was deposited on a 2 cm^2 × 2 cm^2 glass slide for better observation. Raman data were taken at 5 seconds exposure time and averaged over four cycles. The pump laser was 25 mW 532 nm doubled Nd:YAD laser focused by ×100. Another Raman system was used as well: this was a home-made system with a 10-mW argon (Ar) ion laser at 514.5 nm. A 75 cmm spectrometer in a confocal arrangement was used with cooled CCD silicon detector array at -35°C. A 514.5 bandpass filter placed before the sample (to remove the plasma lines) and an edge filter at 520 nm placed after the sample (to isolate the scattered light from the more energetic 514.5 nm laser line).

2.1.2 Anodic aluminium oxide

Anodized aluminum oxide (AAO) substrates were used to incorporate the QDs in them. An AAO film has a dense honeycomb-like array of pores. Porous oxide films may be fabricated on SiO2/Si wafer by depositing a 1μm film of Al following by anodization.

An experimental setup for the anodic oxidation is shown in Figure 2.2. Oxidation of the aluminum in an acid is induced by a potential bias. When oxide dissolution at the oxide/electrolyte interface and the oxide growth at the metal/oxide interface reach equilibrium, the oxidation growth rate is steady. The pore diameter depends on the electrolyte, the anodizing voltage. The oxide's film thickness depends on the duration time of the process.

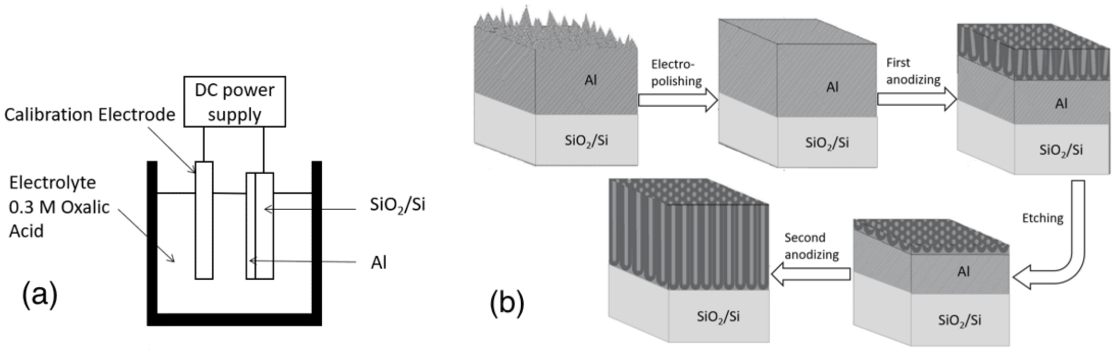

Figure 2.2 (a) Schematic of a typical experimental setup for anodization of aluminum. (b) Scheme of AAO process: (i) high purity aluminum sheet, (ii) electropolished aluminum sheet, (iii) First anodized aluminum sheet, (iv) chemical etched alumina layer, (v) prepared AAO after two-step anodization process.

In our research, the AAO film is fabricated by the two-step anodization process (shown in Figure 2.2). First, a 1μm Al film is deposited on a SiO_2/Si wafer. The wafer is rinsed in ethanol and degreased with acetone. The $Al/SiO_2/Si$ sample is then annealed in a nitrogen atmosphere at 500°C for 5 hours to initiate re-crystallization of Al. Before anodizing, the sample was electropolished in a 1:4 volume ratio of perchloric acid (60 wt%) and ethanol (96 wt%) solution at 5 °C, at a DC voltage of 60 V, applied for 2 mins. Then, the sample is cleaned and dried in room temperature.

A thin layer of nail polish is applied on the Si side of the wafer, in order to protect it from side oxidation. In the first anodization step, the Al/SiO_2/Si sample is anodized under a DC voltage bias of 60 V (Harrison 6204B DC power supply) in a 0.3M oxalic acid solution at 5 °C for 5 mins. When the first anodization is complete, the sample is immersed in a mixture solution of the phosphoric acid (70ml/L) and chromic acid (20g/L) at 65 °C for 15 mins in order to remove the thin oxide layer. The purpose of this step is to remove the first oxide layer and expose the highly periodic indentations on the Al surface; the final oxide layer will grow on that template. The second anodization step is performed under the same conditions as for the first anodization stage however for much a longer time (2 hours) to make sure that the pore depth reaches the SiO_2 layer.

Characterization The structure of the AAO membranes on SiO_2/Si wafer was examined under a field emission scanning electron microscopy (FE-SEM, EM JSM-7900F, JEOL). A very thin layer of carbon was coated on the sample surface and the in-lens emission gun of the microscopy was operate under 5 KV to prevent charging.

2.1.3 Quantum dots preparation and deposition

The CdSe/ZnS core-shell type quantum dots (purchased from Ocean NanoTech, LLC) of various fluorescence wavelength were used in our research. The QD solution was prepared by dispersing 2-5 mg of the quantum dots in 20 ml of toluene and were sonicated for 10-15 mins until fully dissolved. The AAO/SiO_2/Si substrates were cleaned by sonication in ethanol for 5 min and degreased in acetone for 5 min before the deposition of the QDs. The deposition of QDs was made using two coating methods: spin coating and dip coating.

Spin coating process A coating systems P-6000 programmable tabletop spin coater (Integrated Technologies, Inc.) was used for the spin coating process. The substrates were cut into 2cm^2×2cm^2 pieces before the deposition. For each layer of deposition, 1 or 2 drops (about 1 ml) of the QD solution were dropped on the substrate with spinning speed of 2500 rpm for 30 seconds. After the deposition, the surface was lightly wiped with ethanol-soaked Q-tips to remove the excess residue of the QD outside the pore region. The film was later annealed on a hot plate at 100 °C for 1 minute and cooled down to room temperature. The process can be repeated several times to achieve the desired concentration of QDs.

Dip coating process A KSV NIMA dip coater single vessel (small) system was used for the dip coating process. Before deposition, the QD solution was prepared in a beaker to make sure that depth of the solution is larger than the length of the target substrate (2cm^2×2cm^2). The dip-coating process was controlled by a Window based KSV DipCoater control software. For each cycle of the program, the sample substrate was immersed in the QD solution at a constant speed of 50 mm/min until the whole exposed area was under the solution surface. The substrate was kept in the solution for 10 seconds and then was pulled up. The withdrawing is carried out at a constant speed of 2 mm/min and a thin layer of QDs coating was formed during this step. The thickness of the QD coating layer is determined by the withdraw speed: slower withdrawal speed produce thinner coating layer. Most of the QDs were imbedded inside the pores of the AAO while some remained outside the pores. After the whole substrate was pulled out of the solution, the sample was left in that position for 1 min to drain the excess liquid and let the coating dry out. The program repeated the process until the desired film thickness was achieved.

Characterization The fluorescence of the QD solution was carried out by a Cary 100 UV-vis spectrophotometer in the wavelength range of 500 to 1000 nm. The spectra were recorded by a charge coupled device (CCD) camera (ST-6,7,8,9 CCD cameras from the Santa Barbara Instrument Group) controlled by the KestrelSpec

SBIG for windows (version 3.91) software (written by Catalina Scientific Corp.). The scanning electron microscopy (SEM) image of the QDs coating on AAO/ SiO_2/Si substrate was taken with EM JSM-7900F SEM.

2.2 Device Assembly

The substrates were thermally grown 20 nm of SiO_2 (or in some cases, 150 nm) on <100> p-type Si wafers; the Si served as a back-gate electrode. For the anodization, a 1-micron Al film was deposited on top of the SiO_2 layer; the Al was later anodized completely per previous recipe [85]. Anodization of the Al resulted in a hole-array with a pitch of ca 100 nm and a hole-diameter of less than 30 nm. The hexagonal hole-array was polycrystalline with a typical domain size of a few microns. The CdSe/ZnS QD either with peak luminescence at 590 nm, or at 670 nm were suspended in toluene and spin-casted into the anodized porous substrate. The QDs were coated with octadecylamine to prevent agglomeration while in suspension. Excess dots lying on the substrate surface were wiped away. The graphene was manufactured by chemical vapor deposition technique (CVD) on copper foil and was transfer onto the QD embedded substrate. We retained the 250 nm thick PMMA layer - used for the graphene transfer - as a protective upper coating. The deposition method yielded no more than a two-layer film, as determined by Raman spectroscopy. The schematic and picture of the device are shown in Figure 2.3.

To form the graphene FET, the drain and source electrodes are made of one side conductive copper tapes, and the gate electrodes are made of double side conductive copper tape with one side connect to the Si back gate and the other side attached to the glass slide hold (as shown in Figure 2.3 right). The electrode width is 3-5mm, and the graphene channel between the drain and source electrodes is about 1cm^2.

To study the fluorescence resonance energy transfer (FRET), another porous template was used as the substitution of the AAO. Periodical nanoscale pores with a

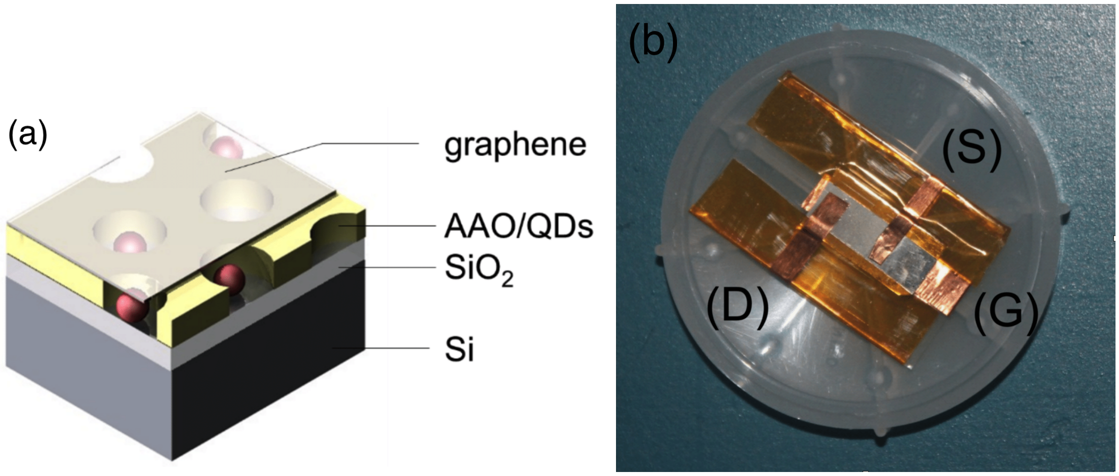

Figure 2.3 (a) Schematics of the graphene FET device configuration. (b) 1cm^2 channeled device with a transferred CVD grown graphene: (D), (S), and (G) are Drain, Source and Gate electrodes, respectively. The graphene was deposited at the region between the D and S on top of the Cu electrodes.

diameter of 30nm were etched on the oxide layer of a Si wafer. The pitch of the pores is 250 μm and the depth of each hole is 10-20 nm. One layer of core-shell CdSe/ZnS QDs was deposited in the pores with graphene film on top. The PMMA layer on top of the graphene was removed by acetone at 40°C or Anisole at room temperature. Another layer of CdSe/ZnS QDs with longer wavelength was deposited on top of the graphene film by spin coating.

2.3 Measurement

2.3.1 Photoconductivity measurement

Photocurrent was regulated by the radiation luminance and applied voltage. To measure the photocurrent, a 532nm Nd:YAG laser was used as the light source. The samples were kept in completely darkness for a few hours to attain equilibrium before the measurement. A 150V Fluke 415B High Voltage DC power supply was served as the bias power supply. A Hewlett Packard 34401A multimeter and an Keithley 175 Auto-ranging Multimeter were connected to a probe station to measure the the current-Voltage curves (I-V curves). Contacts to the graphene layer was made either by a direct contact with the probes, by using Cu conductive tapes, or, by contacting Au/Pd sputtered films on top of the graphene. The linear current voltage (I-V) characteristics of the sample was measured in complete darkness. The channel resistance was in the range of MOhms across a 1 cm^2 films. The samples, with an expose area of approximately 1 cm^2, were illuminated by a white light source equipped with a tungsten halogen lamp at the level of 50 mW/cm^2. Its light was focused and placed approximately 20 cm from the samples. The source had two arms: one was used as a reference while the other was used to illuminate the sample. The schematics of photocurrent measurement equipment setup was shown in Figure 2.4.

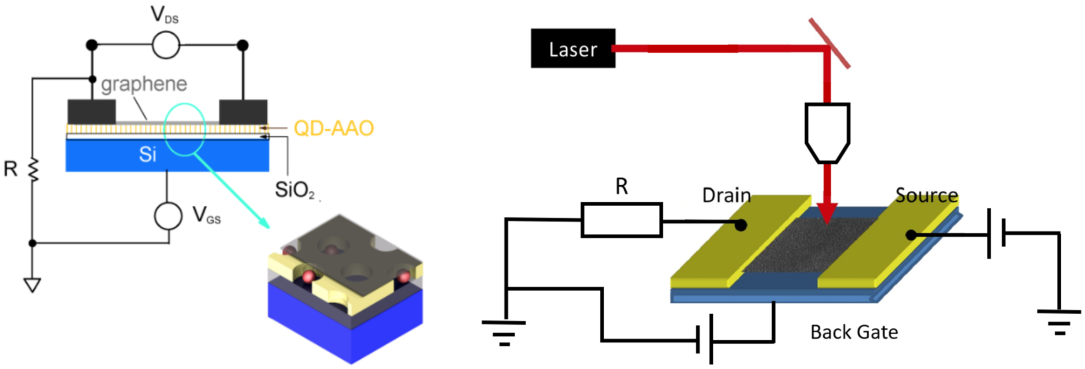

Figure 2.4 Schematics of photocurrent measurement equipment setup.

2.3.2 Lifetime measurement

Lifetime and spectral line width data were obtained using a microscope system (Olympus IX71) coupled to both a spectrometer with a CCD detector array and to a single photon avalanche photodiode (SPAD). The sample was excited with 488 nm pulses (19 μW, 5 MHz, 200 ps) from a supercontinuum laser (Fianium WhiteLase SC-390). The excitation wavelength was selected using an acousto-optic tunable filter (AOTF) along with a bandpass filter. A 5× objective (Olympus NeoSPlan, 0.13 NA) was used to both focus the excitation and collect the emission. A dichroic filter (Semrock FF506-Di03) was used to separate the excitation and emission wavelengths. For spectral measurements, the collected emission was directed to the entrance slit of a 300 mm focal length spectrometer (Acton, SP2300) equipped with a 150 l/mm diffraction grating and a 1320×100 channel CCD (Princeton Instruments, PIXIS 100BR). Time-resolved data was collected using the time-correlated single photon counting technique (TCSPC). For the TCSPC measurements, the collected emission from the sample was sent to a SPAD (MPD SPD) after passing through a long pass filter (Chroma, HQ520LP). The pulses from the SPAD were recorded using a computer controlled TCSPC system (Picoquant, PicoHarp300). For the angle-resolved measurements, the sample was tilted with respect to the p-polarized laser.

2.3.3 Confocal fluorescence microscope

In our experiments, fluorescence (FL) data were obtained with a confocal fluorescence microscope system. A 25 mW, CW, 532nm Nd: YAG laser (LaserGlow Technologies) was used as the light source and the green light was focused to a $25\mu\mathrm{m}^2$ area on the sample (the graphene-channel region). A dichroic mirror and a laser cut-off filter isolated the fluorescence from the laser wavelength. The signal was captured by a CCD camera connected to a computer. The sample was tilted as needed for proper coupling to the surface modes. Tilting of the sample was made by modifying the optical microscope to include a rotational stage instead of the tradition microscope platform. The spot position of the focused 488 nm pump beam was monitored by a separate CCD camera to help minimizing spot wobbling. Due to the relatively large pump spot, re-focusing was found un-necessary for angles smaller than 10 degrees; however, this may be of concern for tightly focused beams.

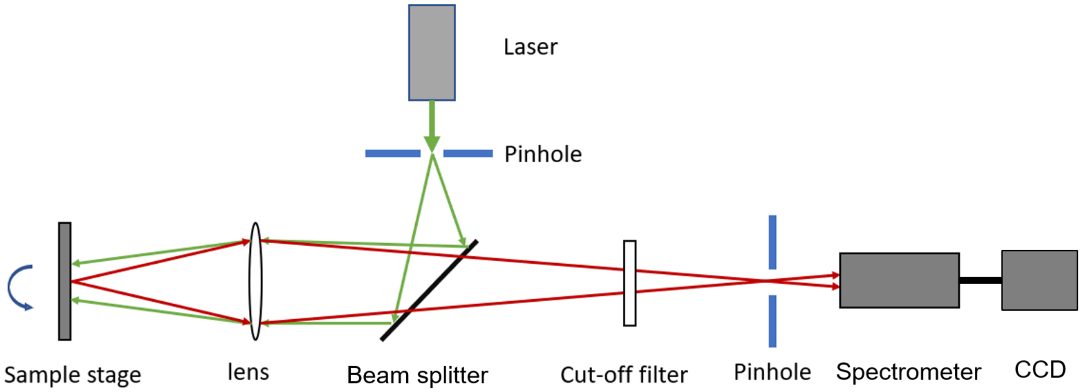

Figure 2.5 Experimental setup of the confocal fluorescence microscopy.

CHAPTER 3

CHARACTERIZATION

This chapter is devoted to the characterization of the graphene, anodic aluminum oxide and quantum dots. Several analytical techniques including SEM, Raman spectroscopy were used to confirm the properties of the devices.

3.1 Characterization of Graphene

3.1.1 SEM

As mentioned in Section 1.1.3, the graphene film deposited on a substrate can be identified by the color contrast between the graphene and the substrate surface under SEM. Since mono layer graphene sheet is only one atom thick and its optical transmittance is high, a suitable substrate is necessary to distinguish the graphene by SEM. Low beam voltage is also needed because of charging. Transferred graphene on a <100> Si wafer with a 50 nm SiO_2 oxide layer and 10 nm alumina layer is shown in Figure 3.1. The figure shows the color contrast of the graphene edge and the substrate surface.

3.1.2 Raman spectra

Raman spectra of the graphene grown on copper film by the CVD process was measured in our research were obtained. Figure 3.2 shows the Raman spectra of single layer and bi-layer graphene samples using a 532 nm laser line. It is clear that all three spectrum show the Raman characteristic lines of graphene at ~ 1580 nm^{-1} (G band) and at ~ 2700 nm^{-1} (2D band). The peaks below 1000 nm^{-1} are from the copper film substrate underneath the graphene. The intensity ratio of the 2D band and the G band decreases from spectra Figure 3.2(a) to Figure 3.2(c), which indicate that the graphene increases from a single layer to a bilayer. Some defect-induced

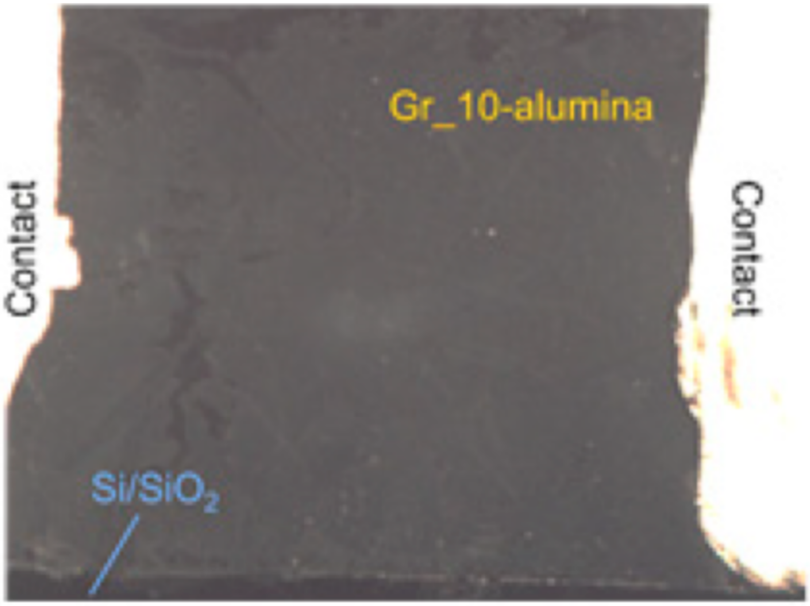

Figure 3.1 A SEM image of a transferred graphene sheet on the alumina/SiO_2/Si wafer.
Source: [52]

Raman peaks can be seen in the bi-layer graphene samples, (Figure 3.2 (b) and (c)). Defects are exhibited through the D band at $\sim$ 1350 nm^{-1}. A stronger D band and another defect line at $\sim$ 2950 nm^{-1} was observed in the spectra (c) implying defects [157].

3.2 Characterization of Nanoporous Template

3.2.1 AAO

The nanoscale pore diameter and the regular interpore distance make anodized aluminium oxide (AAO) a good template to isolate quantum dots in our device fabrication. In our research, the AAO template was produced using the process mentioned in Section 2.1.2. Figure 3.3 is the SEM images of the obtained AAO template on a 2 cm × 2 cm Si substrate with 50 nm oxide. It is clearly shown that the periodic nanoscale pores were formed and arranged in hexagonal arrays on the substrate surface. The arrays of pores of AAO were 25-30 nm in diameter, separated by a pitch of ca 100 nm. From the cross-section SEM images, the thickness of the

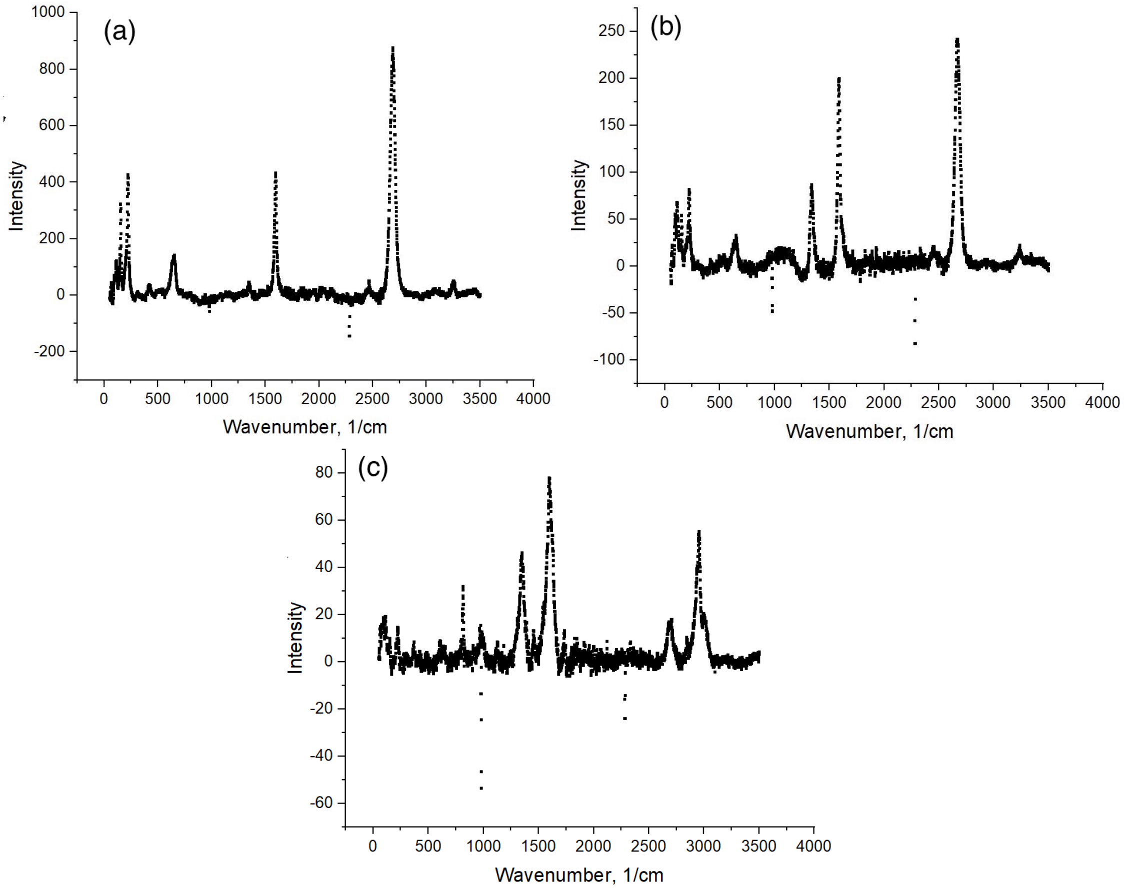

Figure 3.2 Raman spectra of (a) a single layer graphene sample. G band:1589 nm^{-1}, 2D band: 2680 nm^{-1} (b) a bi-layer graphene sample. G band: 1586 nm^{-1}, 2D band: 2670 nm^{-1}. defect band: 1336 nm^{-1}. and (c) a defective bilayer graphene sample. G band: 1578 nm^{-1}, 2D band: 2687nm^{-1}. defect band: 1381 nm^{-1} and 2989nm^{-1}.

AAO layer which is also the depth of the AAO pores is ~2.5μm. The pore diameter, depth and pitch can be modified by changing the produce process parameters such as oxidation time, operating temperature and voltage applied on the electrodes.

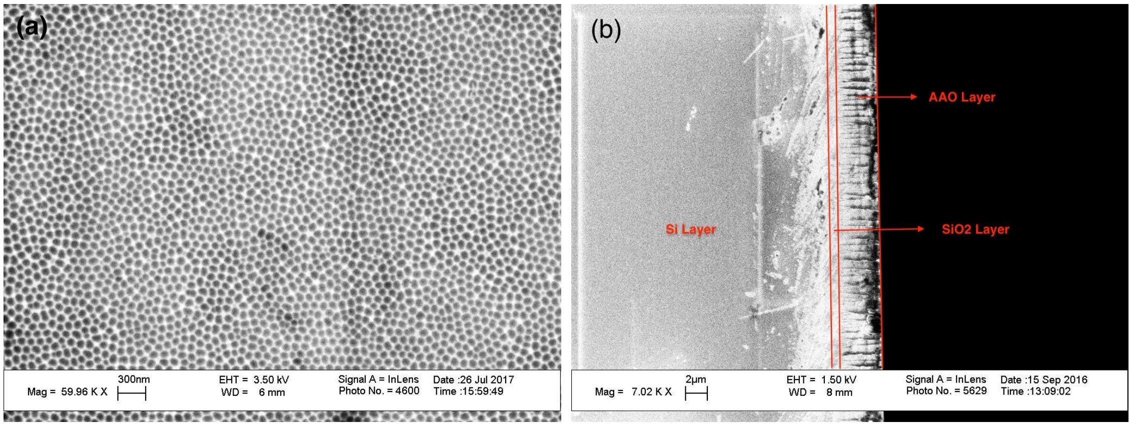

Figure 3.3 SEM image of AAO layer on SiO_2/Si wafer. (a) top view (b) cross section view.

3.2.2 Nanoporous Si oxide

A 20 nm nanopore Si oxide template grown on a p-type Si wafer was fabricated at the Argon National Laboratory (ANL) using e-beam lithography. The SEM image of the nanopore structure is shown in Figure 3.4. The pitch of the pore arrays is 250 μm, the nanopore diameter is 30 nm and the depth is 10-20 nm. Compare to the AAO template, the pore is shallower and the inter pore distance is larger. more QDs are dispersed on the surface than in the pores.

3.3 Characterization of QD

3.3.1 Photoluminescence spectroscopy

Photoluminescence (PL) spectroscopy provide a contactless and nondestructive way to characterize the quantum dots (QDs). CdSe/ZnS core-shell QDs with various emission wavelength were used. Each kind of QDs was dissolved in toluene at different concentration levels and were deposited on glass slides using spin coating. The PL spectra of CdSe/ZnS QD samples measured at room temperature are shown in Figure

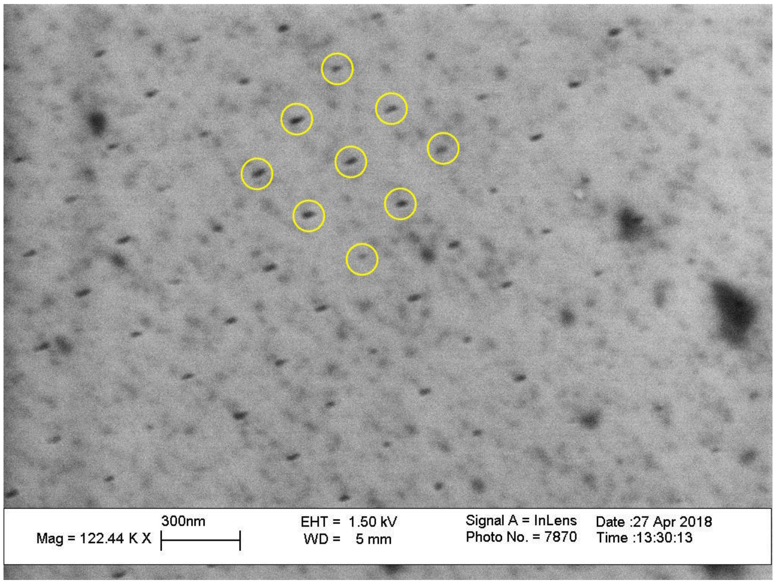

Figure 3.4 SEM image of lithographically defined nano-pores. The yellow circles mark some aligned nano-pores.

3.5. The full width half maximum (FWHM) of the emission spectra of the 580 nm, 630 nm and 680 nm QDs are 33 nm, 21nm, 25nm, respectively. Compared to organic dyes (FWHM=35∼100 nm for dyes with emission spectra between 500 to 700 nm [130]), these QDs have narrow emission spectra.

3.3.2 SEM

Figure 3.6 shows SEM image of diluted solution of CdSe/ZnS in toluene deposited on the AAO substrate using spin coating. The toluene was let to evaporate completely. The black dots in the image are the QDs and it imply that most of the QDs are embedded in the pores of the AAO template, while only ∼5% of the QDs laid outside of the pores. The minimum distance between two QDs is about the pitch of the AAO template, which is much larger than the diameter of the QDs.

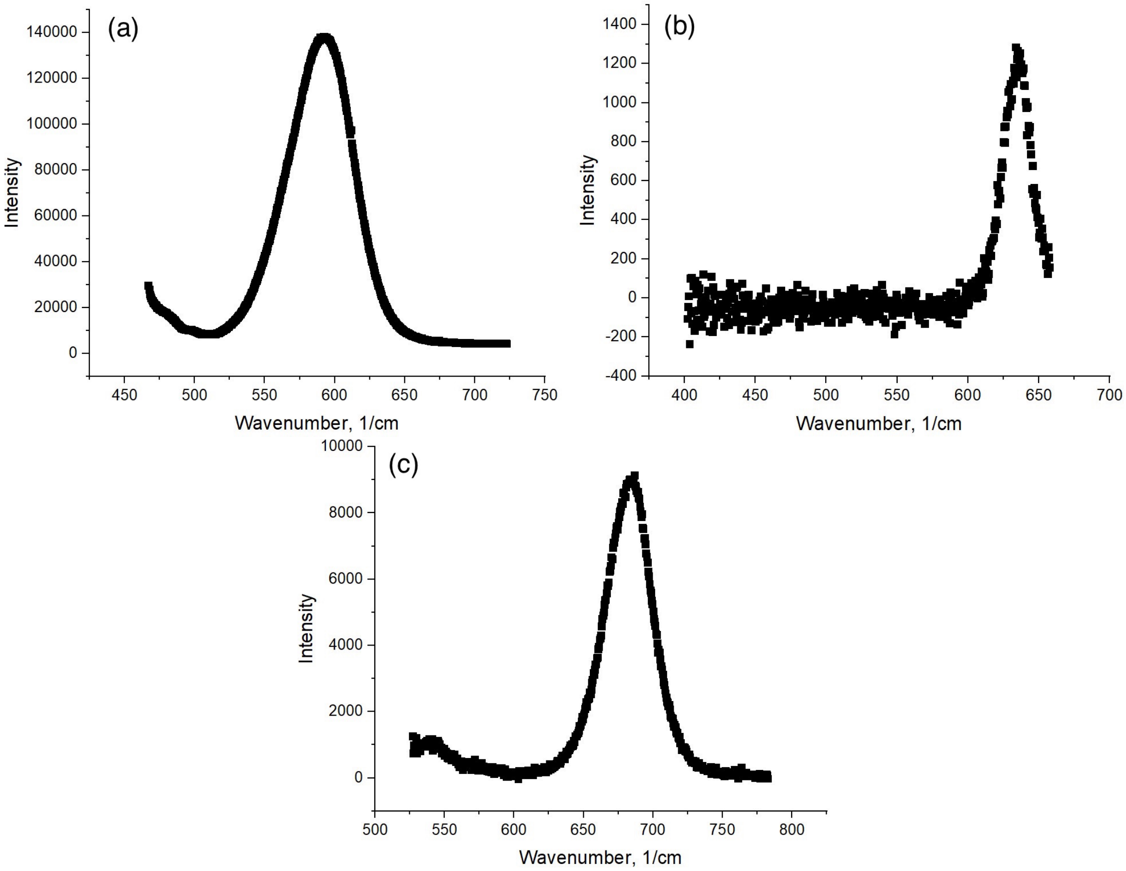

Figure 3.5 PL spectra of (a) CdSe/ZnS QDs with emission peak at 580 nm, the exposure time is 2.5 s; (b) CdSe/ZnS QDs with emission peak at 630 nm, the exposure time is 2 s; (c) CdSe/ZnS QDs with emission peak at 680 nm, the exposure time is 10 s. The excitation laser is 25mV, λ=532 nm.

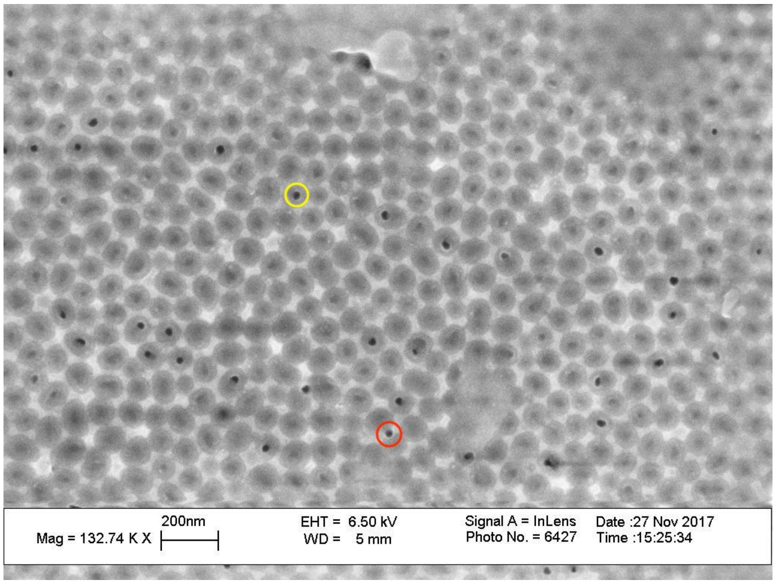

Figure 3.6 SEM picture of QD-filled AAO. The yellow circle marks a QD filled right into a pore on the AAO template, while the red circle marks a QD laying outside the pore.

CHAPTER 4

ELECTRICAL AND PHOTO-INDUCED EFFECTS OF GRAPHENE CHANNEL

Field effect transistors with graphene channels were interfaced with arrays of semiconductor quantum dots (QD). In this chapter, we assess the the electrical characteristics of the elements. The channel response to white light illumination was also assessed as a function of drain-source and gate-source biases.

The device was fabricated as described in Chapter 2. The substrates were composed of 150 nm of SiO_2 on <100>p-type silicon. The Si substrate served as a back-gate electrode. 250 nm of Al layer was deposited on the SiO_2 layer; the Al was later anodized completely per our previous recipe. As a result of anodization, 50-100 nm thick perforated alumina layer was formed on top of the SiO_2 layer. The arrays of holes were 25-30 nm in diameter, separated by a pitch of ca 100 nm. Core-shell semiconductor CdSe/ZnS QDs were imbedded in the pores. The QDs were suspended in an acetone-diluted acrylic polymer and were depositing the holes by drop casting. The peak fluorescence of the QDs was assessed at 520 nm when pumped with a 488 nm ion Ar laser. The graphene films were transferred onto the various substrates [90] to serve as a device channel. Two metal contacts were used as drain and source electrodes. Contacts to the graphene layer were made either by a direct contact with the probes, by using Cu conductive tapes, or, by contacting Au/Pd sputtered films on top of the graphene. The I_{ds}-V_{ds} curve was linear in all cases. The channel resistance was in the range of MOhms across a 1 cm films (see for example, Figure 4.1). The ca 1 cm^2 samples were illuminated by a white light source equipped with a tungsten halogen lamp at the level of 50 mW/cm^2.

4.1 Photo-current Measurement

First, we ascertained that our method works well. The samples were 150 nm thick oxide on the same silicon wafers albeit with the Al removed by etching. Contacts to the graphene were made with two Cu tapes. As demonstrated by Figure 4.1a, the I_{ds}-V_{ds} curve was linear. The curve for I_{ds}-V_{gs} exhibited the familiar upward inclination typical of graphene channels.

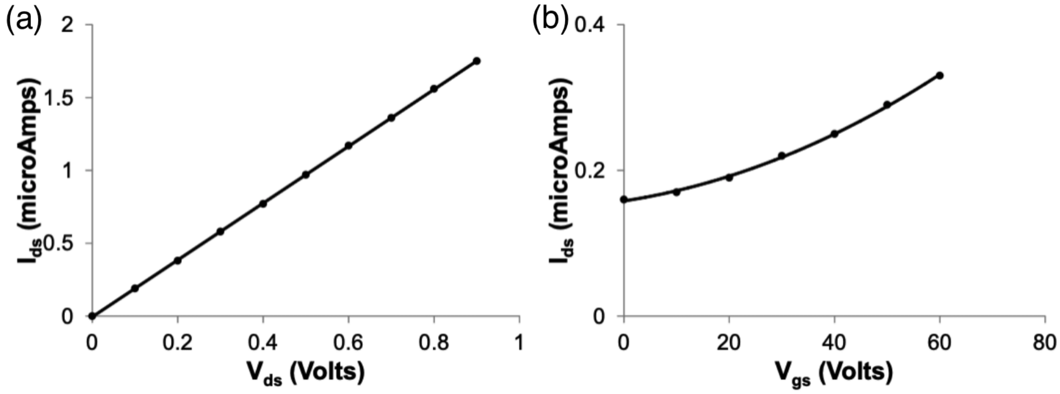

Figure 4.1 (a) Drain-Source current as a function of drain-source voltage, I_{ds}-V_{ds} on a flat oxidized Si surface at a given source-gate voltage, V_{gs}=0 V. (b) drain-source current as a function og gate-source voltage, I_{ds}-V_{gs} for a given drain-source voltage, V_{ds}=0.1 V

The I_{ds}-V_{ds} curve for graphene on AAO was linear, as well. It was similar to samples shown in Figure 4.1. The I_{ds}-V_{gs} curve for sample with QD in AAOs and graphene on top, however, exhibited a reverse trend as shown in Figure 4.2. One may observe some asymmetry in the curve, as well.

4.2 Under White Illumination

Under white light illumination, the current generally increased a bit. Nevertheless, the I_{ds}-V_{gs} curves exhibited a decrease as a function of V_{gs}. In Figure 4.3 we show maps of these trends. While not so apparent, the curves as a function of V_{gs} exhibited the downfall trend of Figure 4.2. The larger voltage range is attributed to a thicker alumina layer under the graphene.

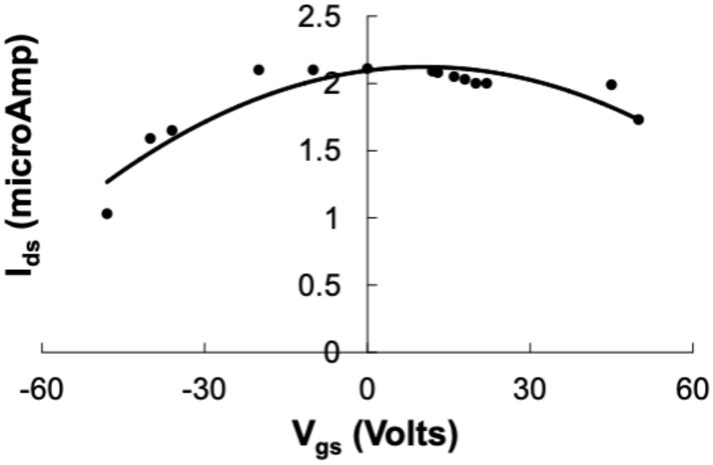

Figure 4.2 I_{ds}-V_{gs} at V_{ds}=0.1 Volts of sample with 520 nm QDs in AAO and graphene on top.

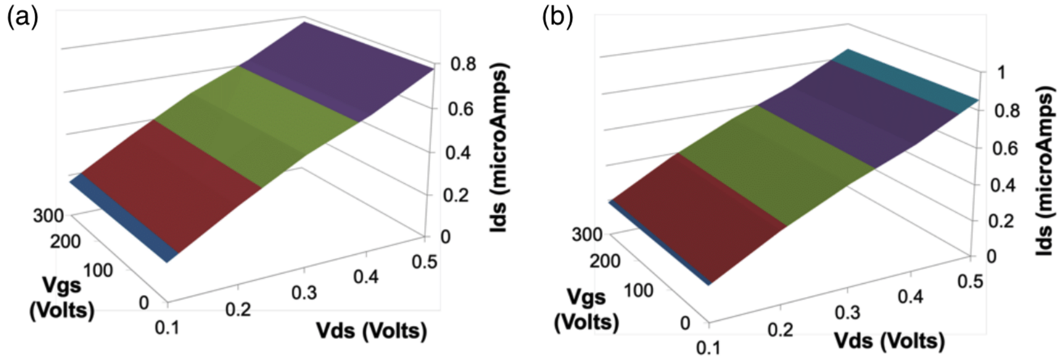

Figure 4.3 Maps of I_{ds}-V_{ds}-V_{gs}. (a) Without white light illumination on the sample. (b) Under 50 mW/cm^2 of white light illumination. The drain-source current has decreased as a function of V_{gs}.

Figure 4.3 may be better understood in terms of the difference and the relative difference in the I_{ds} response to light. In Figure 4.4 we show the current difference map between the illuminated and non-illuminated cases. Resonance may be seen at V_{ds} ~0.3 V. A clearer picture is obtained when we plot the relative differential current under illumination. The relative differential current is directly related to the relative differential channel resistance: specifically, $\delta I_{\mathrm{ds}}/I_{\mathrm{ds}} = \delta R/R$. The white light accentuated the relatively small effect noted in Figure 4.3a even further. One may identify the effect as related to negative differential resistance [15,76]. The effect may be attributed to charge localization under channel illumination.

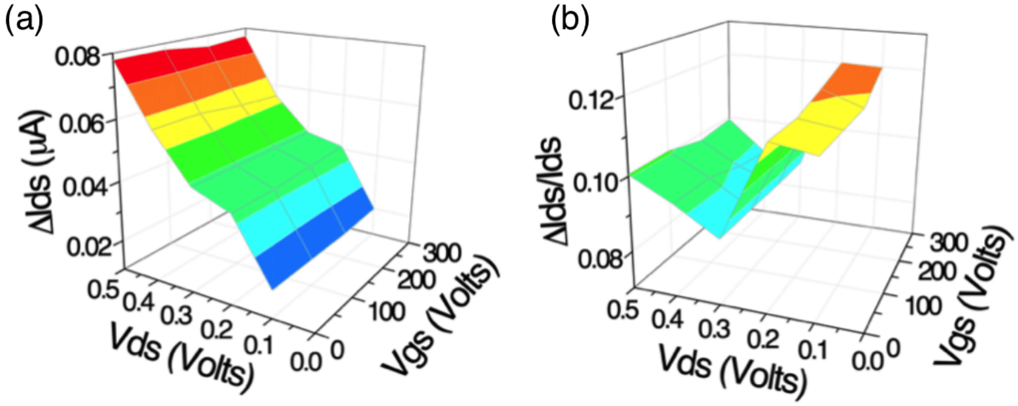

Figure 4.4 (a) Differential current [(I_{ds} under light)-(I_{ds} in dark)]. (b) Relative differential current [(I_{ds} under light) - ((I_{ds} in dark)]/(I_{ds} in dark).

The increase of current in ordinary FET graphene channels is typically explained in terms of an increase in channel doping by the biasing gate potential [110]. The symmetry in the I_{ds}-V_{gs} curve is related to the shift of the conduction and valence branches at the Dirac points in the presence (or absence) of impurities. Here, in contrast, we measure an opposite trend. We explain it as follows: the gate bias polarized the QDs, thus creating charge localization points. This charge localization increased the effective channel resistance. Graphene may be viewed as a lightly doped p-material and, hence, the effect is more pronounced for negative gate-bias values.

CHAPTER 5

ELECTRICAL AND PHOTO-INDUCED EFFECTS IN GRAPHENE CHANNELS INTERFACED WITH QUANTUM DOTS

In this chapter, the electrical characteristics of the graphene channel interfaced with well separated and precisely placed semiconductor quantum dot (QD) array under white light illumination and the device's photoluminescence (PL) properties at various biasing conditions, were studied. Changes in the PL were noted as a function of both the drain-source and gate-source potentials. The PL was more pronounced when the incident, or the emission wavelengths were coupled to surface plasmon/polariton (SPP) modes. The periodic array of the nano-porous structure led to the realization of the first visible surface plasmon laser [11, 84, 85]. Here, we revisit this topic by analyzing the effect of electrical bias on the PL of well-separated core/shell CdSe/ZnS semiconductor QDs when interfaced with graphene channels. Such arrangement may lead to new opto-electronic elements.

As described in Chapter 2, we started with the <100>p-type silicon substrates deposited with 150 nm of SiO_2. Aluminum, 250 nm thick layer, was deposited on top of the SiO_2. As a result of the two-step aluminum anodization, 50-100 nm thick perforated layer (AAO) was formed on top of the Si/SiO_2. The diameter of the holes was ranging between 25 and 30 nm. The pitch of the hole-array was ca 100 nm. Core-shell semiconductor CdSe/ZnS QDs were first suspended in acetone and then drop-casted into the AAO pores. Access QDs were wiped out from the surface. The GFETs were assembled by transferring the CVD growned graphene onto the top of the QD imbedded AAO. The current-voltage curve between the source and drain (I_{ds}-V_{ds} curve) was linear in the absence of light or the absence of gate bias (Figure 4.1).

Current-Voltage curves (I-V curves) were taken with a probe station with a resolution of 100 fA. The samples, with an area of approximately 1 cm^2, were illuminated by a white light tungsten source at various intensities. The fiber interfaced source was focused and placed approximately 20 cm from the samples. The source had two arms: one was used as a reference while the other was used to illuminate the sample. The PL data were obtained with a 35 mW Ar ion laser at 488 nm in a confocal arrangement and using a 20 cm monochromator, a PMT, an optical chopper and a lock-in amplifier. The peak fluorescence of the QDs was assessed at 590 nm (see Figure 5.3b). The sample was placed on a rotatable platform to enable coupling to SPP modes (see below).

5.1 Under White Light Illumination

The electrical characteristics of the GFETs were first studied under white light illumination. We compared the channel current under illumination and under dark conditions. This method is very effective in revealing small conductance changes. The channel current was plotted as a function of V_{ds} and V_{gs} for a fixed intensity value of white-light illumination and compared it with the non-illuminated cases. In Figure 5.1, we show such a map of the differential current [(I_{ds} under white light) - (I_{ds} in dark)] plotted as a function of the drain-source, V_{ds} and the gate-source, V_{gs} voltages. As can be seen from Figure 5.1a, the differential current ΔI_{ds} decreased as a function of V_{gs}. Similarly, varying V_{ds} also affected the differential current, ΔI_{ds}. The map is symmetrical with respect to V_{ds} as may be expected for a linear system. When the sample was exposed to a large intensity of white light (Figure 5.1b) the surface plot changed and became more regular. Here, the current difference became more pronounced as a function of V_{ds} and less pronounced as a function of V_{gs}.

A plot of the channel's current (as opposed to the differential current) as a function of white light intensity is shown in Figure 5.2. Maximum current is observed

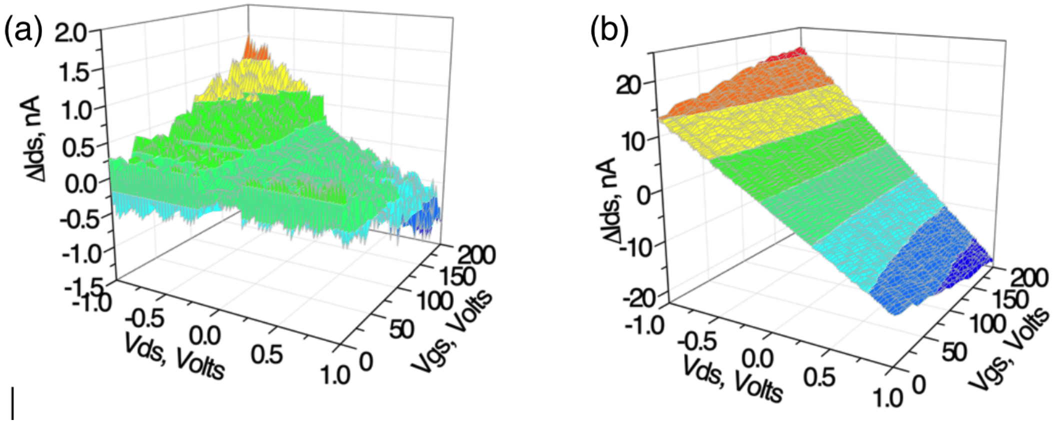

Figure 5.1 The difference in I_{ds} between illuminated and non-illuminated cases as a function of V_{ds} and V_{gs}. (a) The white light intensity was 320mW/cm^2 and (b) The white light intensity was 500mW/cm^2.

for 380mW/cm^2. Clearly, the channel conductance is bleached under strong light illumination. We attribute such behavior to the ionization of the QD, which increased the channel impedance.

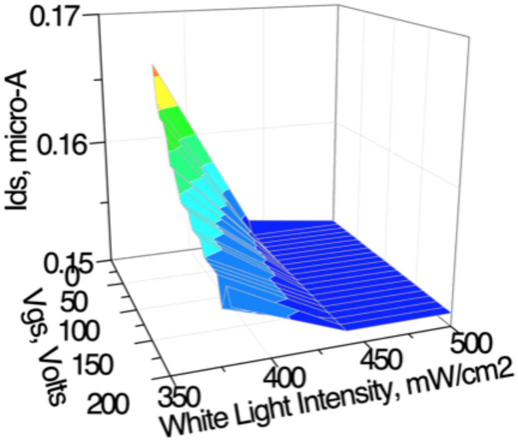

Figure 5.2 I_{ds} as a function of V_{gs} and white light intensity at V_{ds}=0.5V. Bleaching occurs at large white-light values.

5.2 Photoluminescence of the QDs

The photoluminescence of the QDs as a function of V_{ds} and V_{gs} was also assessed. The peak luminescence of QDs was at 590 nm (Figure 5.3b). The PL change was more pronounced when measured as a function of V_{gs}. Figure 5.3a indicates that the

PL peak decreased monotonously as a function of V_{gs}. A slight change was also noted as a function of V_{ds} (Figure 5.4).

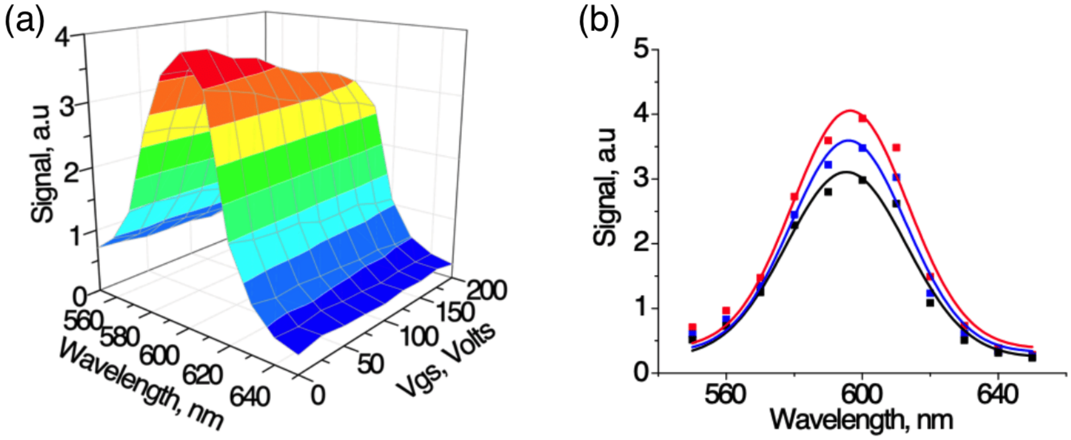

Figure 5.3 (a) PL of QDs as a function of V_{gs} at normal incidence and at V_{ds} =0.1 V. (b) PL as a function of wavelength at V_{gs} =0, 100, 200 V, respectively. V_{ds} =0.1 V and the intensity of the 488 nm laser was 35 mW.

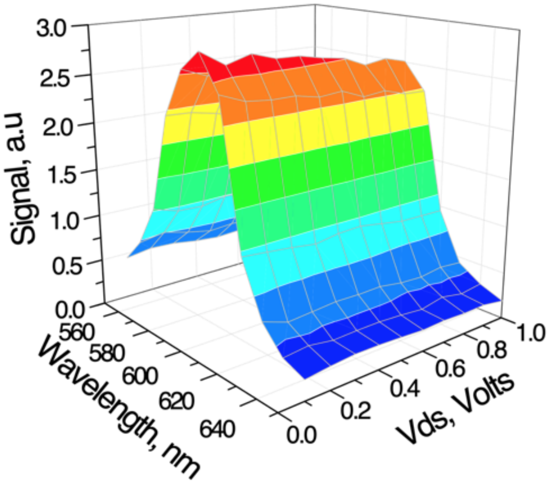

Figure 5.4 PL as a function of V_{ds} at normal incidence at V_{gs} =50 V.

One may postulate that since the QDs are imbedded in a periodic structure, which is bound by conductive surfaces (graphene above and silicon below), then light may be coupled into plasmonic modes. When the incident, or scattered or both wave-vectors are at resonance with the wave-vector of the perforated substrate, the

PL signal maximizes because of the large coupling between the plasmonic mode and the QD. The PL signal is also enhanced because the SPP mode is in phase with the position(s) of the QDs.

5.3 Surface Plasmon/ Polariton

In our case, the optimal launching conditions for a Surface Plasmon/ Polariton (SPP) mode is achieved by a small tilt and in-plane rotation of the perforated substrate with respect to the polarized incident beam. The tilt angle θ may be computed similarly to [50] as,

$$\sin(\theta) = \frac{\lambda_0}{a}\sqrt{(\frac{4}{3})({q_1}^2 - q_1 q_2 + {q_2}^2)} - n_{\text{eff}} \tag{5.1}$$

where λ_0 is the incident or emitted wavelength, a is the pitch for the holes array ($a \sim$ 100nm), q_1 and q_2 are sub-integers (e.g., 1/5, or 1/6) representing the ratio between the array pitch and the wavelength. The effective refractive index, n_{eff} is of order unity, $n_{\text{eff}} \sim 1$.

The plasmonic resonance was observed in the experiments. The GFETs sample was rotated in-plain to achieve maximum signal and then tilted with respect to the incident wave-vector. The incident beam was polarized such that it had a polarization component perpendicularly to the sample's surface (p-polarization). As observed from Figure 5.5, there are two signal peaks as a function of the tilt angle: one peak is situated at θ=0° and the other at $\theta \sim 8°$. The first peak may be attributed to the plasmonic mode for the excitation wavelength (λ=488 nm) while the other may be attributed to the emission wavelength (λ=590 nm). Using Equation 4.1, we obtain θ=7.668° with a=100 nm, n_{eff}=1.02, q=1/6 and λ=590 nm - in good agreement with the experimental data. A reference experiment made on flat glass showed that the PL signal monotonously decreased as a function of the tilt angle.

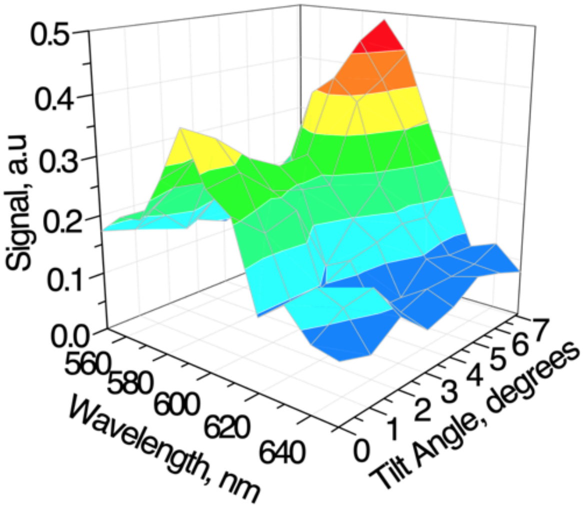

Figure 5.5 Photoluminescence as a function of the tilt angle.

5.4 Conclusions

In summary, the electrical and optical properties of graphene channels were studied when interfaced with well-separated and periodically placed quantum dots. Photoluminescence has peaked when either the incident or the emission wavelengths were effectively coupled to surface plasmon/polariton modes.

CHAPTER 6

PHOTOELECTRONIC EFFECTS OF GRAPHENE CHANNELS INTERFACED WITH AN ARRAY OF INDIVIDUAL QUANTUM DOTS

In this chapter, we report on negative differential photo-related conductance of surface graphene guides under light and a diminishing fluorescence effect as a function of bias. The graphene was interfaced with an array of individual semiconductor quantum dots, whose position was commensurate with the optical guide modes. The periodic structure suppressed coupling between the pump laser and its related surface modes, letting us study the effect of bias and fluorescence of only the surface propagating and standing modes as a function of bias. The surface guide served as a channel for a Field Effect Transistor (FET) while the dots were placed within the capacitor formed between the graphene channel and the gate electrode. We suggest that the quenched fluorescence may be hindered, to some degree, by incorporating the QD in a resonator, which is tuned to the emission wavelength.

6.1 Background

Early on, field effect transistors (FET) demonstrated its unique electrical properties [160]. One may also expect unique electrical effects when the graphene (or graphene oxide, GO) is interfaced with semiconductor quantum dots (QDs) [31, 75, 76, 148] or with dyes [92, 96, 103, 150]. In those experiments, the fluorophores were placed on top of the graphene substrates, contrary to the present design. Graphene quenched the fluorescence and recent interpretations attributed it to a physical transfer of electrons from the fluorophores to the graphene [75, 92], similarly to donor doping in semiconductors. Somewhat in support of that notion was given in [31]; the fluorescence quenching hindered as the distance between QD and GO increased.

Similar to SWCNT, the mobility of a graphene coated with an optically sensitive film ought to depend on the mobility of carriers in the film as well [82]. We note that: (a) the photo-induced transport as a function of light intensity involves the entire graphene channel and (b) the channel characteristics nearby the QD is more local and may directly affect the fluorescence process [15]. A different point of view was given in [29]; the energy transfer between the QD and graphene is attributed to FRET (frequency resonance energy transfer which is enabled through screening by the graphene). The problem is that near the Dirac point such screening is linearly diminishing [26] and the screening, if exists, should be non-linear and depending on the amount of charge placed within a small distance away from the graphene [37,138]. While not directly related to the quenching mechanism(s), we set here to investigate the effect of bias on the photo-conductivity and fluorescence of individual QD when placed within the gate-channel capacitor.

Electrical properties of graphene on periodic and porous substrates, such as anodized aluminum oxide was studied in the past [8, 10]. It was found that the periodic holes array may accentuate the Raman spectra of the graphene lines and led to the realization of the first visible surface plasmon laser [11, 84, 85]; there, one takes advantage of simultaneous resonating plasmon/polariton modes at both the pump and at the emission frequencies. Here, we go one step further and focus on the electro-optical and photoluminescence as a function of the device bias; by suppressing the coupling between the pump laser radiation and its related propagating surface modes we concentrate on only the emission radiation. Additionally, since the graphene is partially suspended over the substrate pores, the fine structure constant $\alpha = e^2/(\varepsilon\hbar\nu_{\mathrm{F}}){>}1$ with ε, the dielectric constant of the vacuum [37, 61]. Finally, the absorption of graphene (~2.3% per layer) is comparable to the absorption of monolayer of CdSe/ZnS QD (the linear absorption coefficient of QD is A$\sim 10^5$ /cm and a typical dot diameter is D=3 nm. If we assume that the absorption behaves as

$[1 - exp(A * L')] \sim A * L'$, where $L' \sim$D is the thickness of the absorption QD layer, then the absorption of a QD monolayer is ∼3%).

At visible and near-IR wavelengths, graphene acts as a lossy dielectric [18]. Since the graphene is atomically thin, we were able to realize a surface guide, sandwiched between two lower dielectric media: air/polymer on the top and silica/alumina at its bottom. At the same time, the graphene's conductivity may be tuned by biasing. This enabled us studying the effect of varying conductivity on the optically induced current and on the related QD photoluminescence.

The array of pores in the anodized aluminum oxide layer provided us with yet another advantage. Surface modes decay exponentially away from the thin guide and, hence are concentrated at the guide surface (and toward the QDs). The periodic pattern of pores enabled coupling between the free space radiation and the propagating surface modes. If properly designed, the array of pores may facilitate standing surface modes for a strong coupling between electromagnetic radiation and QDs [50].

6.2 Assembly

The schematic of the FET and an SEM picture of the porous substrate are shown in Figure 2.4 and Figure 3.6, respectively. 20 nm of SiO_2 (or in some cases, 150 nm) of oxide was deposited on a <100>p-type 1-10 Ohms.cm Si wafer; the Si served as a back gate electrode. For the anodization, a 1-micron Al film was deposited on top of the SiO_2 layer; the Al was later anodized completely per previous recipe - its final thickness was estimated as ∼50 nm. Anodization of the Al resulted in a hole-array with a pitch of ca 100 nm and a hole-diameter of less than 30 nm. The hexagonal hole-array was polycrystalline with a typical domain size of ∼10 microns. The CdSe/ZnS QD either with peak luminescence at 590 nm, or at 670 nm were suspended in toluene and drop-casted into the anodized porous substrate. The QDs were coated with octadecylamine to prevent agglomeration while in suspension. Mostly one QD occupied a filled AAO nano-hole (Figure 3.6). Excess dots lying on the substrate surface were washed away. The graphene was produced by chemical vapor deposition technique (CVD) on copper foil and was transfer onto the QD embedded substrate by use of 250 nm poly (methyl methacrylate), PMMA film [90]. We retained the PMMA film as a protective upper coating and as a dielectric layer. The deposition method yielded no more than a two-layer film, as determined by Raman spectroscopy. Raman spectroscopy of the QD interfaced graphene also revealed a large graphene defect line, situated at 1340 cm^{-1}. This line is rather small for a free-standing graphene, or graphene films deposited on quartz. The linear $\mathrm{I_{ds}}$-$\mathrm{V_{ds}}$ curve may be explained by the large surface states at the area of contact making it ohmic. Luminescence data were obtained in confocal arrangement. A 30 mW, CW, 532nm Nd:YAG laser was focused to a 25 μm^2 spot. The sample was tilted and rotated to produce optimal coupling with the surface modes as in ref. [84].

6.3 Photo-current Under White Light

The $\mathrm{I_{ds}}$-$\mathrm{V_{gs}}$ curve for QDs interfaced graphene channels under uniform white light illumination and under dark conditions is shown in Figure 6.1. Typically, a minimum in the $\mathrm{I_{ds}}$-$\mathrm{V_{gs}}$ curve signifies the condition where the Fermi level of the graphene is situated at the Dirac point ($\mathrm{E_F}$=0 eV; the conduction band is empty while the valence band is full). Here, the QDs are partially ionized at room temperature and the resulting gate effect makes the graphene channel more of an n-type at $\mathrm{V_{gs}}$=0 V. Illumination by a laser, or white light results in a Dirac point shift towards the negative $\mathrm{V_{gs}}$ values (namely, the channel becomes even more an n-type at $\mathrm{V_{gs}}$=0).

Figure 6.1 shows the effect of a channel under white light illumination at 380 and 440 mW/cm^2, respectively. The white-light beam illuminated the entire sample area. Shown is the current difference (current under white-light minus the current at dark conditions) as a function of V_{gs} and V_{ds}. The channel here was deposited on a 150 nm thick oxide, hence the relatively large V_{gs} values. As can be seen from the Figure 6.1(a,b), one can identify two trends: (1) when the light intensity is relatively small. The ΔI_{ds}-V_{ds} curve slop is constant and positive for smaller values of V_{gs} while negative for larger values of V_{gs}. This suggests that the photocurrent (which is proportional to the differential current) may have originated from the graphene rather than the QDs because, as the 'doping' of the graphene becomes larger and the conductive states become occupied, the photo-assisted transition of electrons require larger energies. (2) As we increase the white-light intensity, the overall trend of the ΔI_{ds}-V_{ds} curve is negative. This suggests a saturation of the photo-assisted transitions. Indeed, Figure 6.1c exhibits current saturation beyond intensity values of 440 mW/cm^2. We note that the FL experiments were conducted with a focused laser beams whose intensity was on the order of 10^5 W/cm^2 and hence, one may assume a larger degree of QD excitation and perhaps some ionization. Finally, we show another sample where the Dirac point was situated at $V_{gs}>0$ which could be attributed to the surface potential of the alumina.

6.4 Photo-current Under Laser Illumination

The electrical characteristics of the GFETs were also studied under the illumination of a 30 mW/cm^2, CW Nd:YAG laser. Compare to the white light illumination case, the graphene channel became more conductive as a function of both V_{gs} and V_{ds} when uniformly illuminated by the laser at 532 nm (Figure 6.2). This intensity is much smaller than had been used by either Ref. [75] or [92]. The major dip in the illuminated curve at V_{gs}=-2.3 V can be identified as the position of the Dirac point, which has been shifted from V_{gs}=-1.3 V for the non-illuminated case. The second dip, at V_{gs}=-2.7 V is shared by the channel under dark conditions and hence can be attributed to the effect of V_{gs} on the QD band structure itself. The third dip at

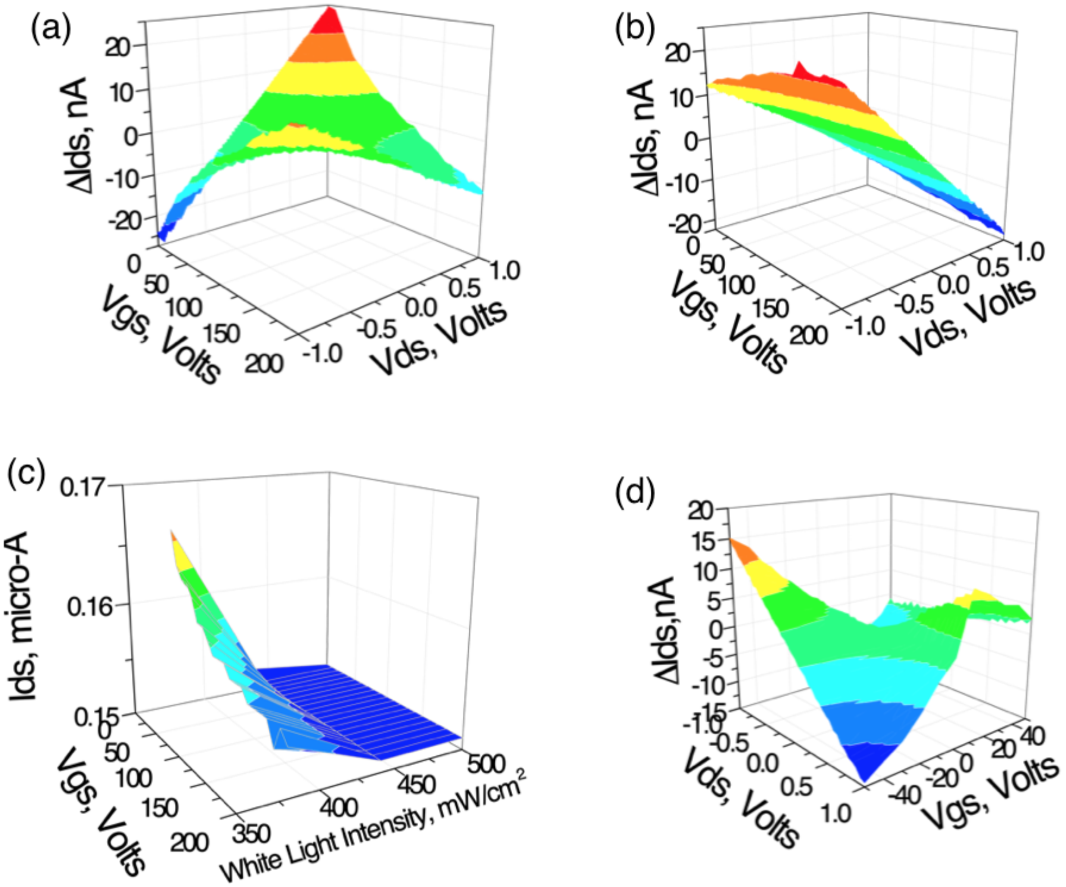

Figure 6.1 (a) Channel conductivity under white light (380 mW/cm^2) and dark conditions. Plotted is the difference in channel current as a function of V_{gs} and V_{ds}. The thicker oxide of 150 nm resulted in larger V_{gs} values. Compared with V_{gs}=0 V, V_{gs}=200 V the differential current changes direction. (b) The differential current at larger intensity of white light illumination (440 mW/cm^2); the differential current has a negative trend for both V_{gs}=0 and V_{gs}=200 V. (c) Channel current, Ids as a function of V_{gs} and white light intensity at V_{ds}=0.5V. (d) Another sample illuminated by white light: the negative trend in the differential current can be explained by the position of the Dirac point, close to V_{gs}=+20 V. Upon illumination, it has shifted towards the V_{gs} negative values.

V_{gs}=-4.6 V appears only for the illuminated curve (for all V_{ds} values) and may be attributed to negative differential photo-conductance [83].

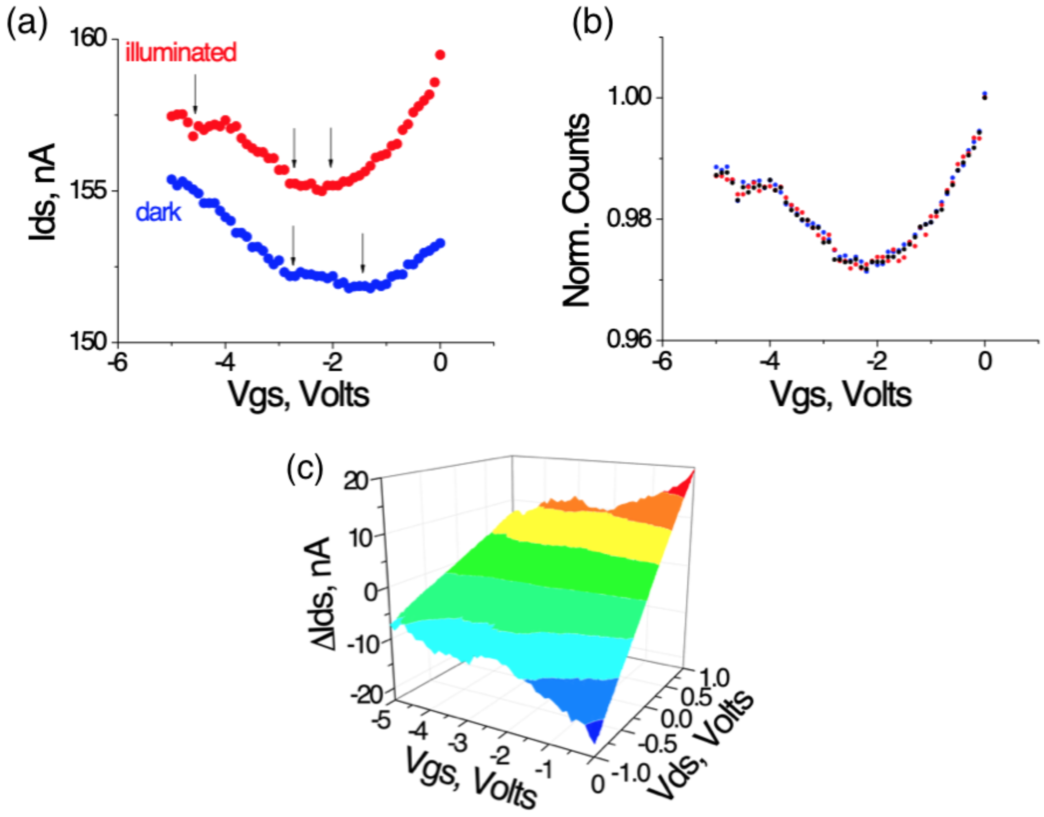

Figure 6.2 Channel conductivity under dark and under uniform illumination by a 532 CW laser at 30 mW/cm^2. (a) Comparison between illuminated and non-illuminated I_{ds}-V_{gs} curves. V_{ds}=0.3 V. The arrows point to the position of the various dips. (b) Normalized I_{ds}-V_{gs} curves: illuminated sample at V_{ds}=0.1, 0.2 and 0.3 V. (c) The differential current (channel current difference between illuminated and dark conditions).

We note that the background current in Figure 6.2a has been elevated; it is a combination of channel doping and varying channel mobility near the Dirac point. Away from the Dirac point, say at V_{gs}=0 V where the conductivity is almost solely controlled by the charge density and less by the nonlinear channel mobility this is translated to a charge increase of $(7 \times 10^{-9} A)/(1.6 \times 10^{-19} A) \rightarrow 4.4 \times 10^{10}/cm^2$ (since our sample area was 1 cm^2). This is approximately the number of carriers induced by 1 V of the gate (the so called geometrical effect) assuming an oxide thickness of 20 nm and alumina thickness of 50 nm. At the same time, the number of photons from a 30 mW/cm^2 laser at 532 nm is 10^{17} photons/s·cm^2. Another word, the graphene and the QDs each absorbed $\sim 10^{15}$ photons/s·cm^2. This is the number of excited carriers and at least for graphene, is larger than the saturation density at $\sim 10^{13}$ cm^{-2} [14] and not that far from the saturation of SWCNT [55]. At large white light intensities, the photo-current decreased and became saturated. All of these suggest that the channel photo-conductance and its carrier concentration is not solely dependent on the behavior of the QD but also on the photo-conductivity of the graphene itself.

6.5 Fluorescence Measurements

Enhanced peak luminescence at resonance and at off-resonance conditions are shown in Figure 6.3. Shown are the spectral curves at tilt angle of $\theta = -5°$ (close to emission minima) and at tilt angle of $\theta = -13°$ (close to the emission maxima). Clearly seen is a line broadening of more than 25% which is attributed to a Purcell's effect (namely, an increase in the density of states when the luminescing wavelength is at resonance with a cavity). The Purcell's effect alludes to a decrease of the life-time of the excited e-h pair in the QD as measured for a similar system of QD in AAO [51]. There is also a small but clear peak shift due to the particular hole-array pitch involved in the resonance condition.

Suppression of the fluorescence [29] as a function of $\mathrm{V_{gs}}$ may be attributed to the change in the channel conductivity [161]; as the channel became more conductive, the fluoresce quenches. This is a local effect due to the conductivity change of graphene at the vicinity of localized QD.

The change in FL as a function of $\mathrm{V_{ds}}$ may be understood with the model shown in Figure 6.4. The surface potential, $\mathrm{V_{ds}}$(x) on the graphene channel varies linearly from source (typically at ground) to drain (held at a potential $\mathrm{V_d}$). Since the waveguide is all but surface, one may consider the surface potential of the guide

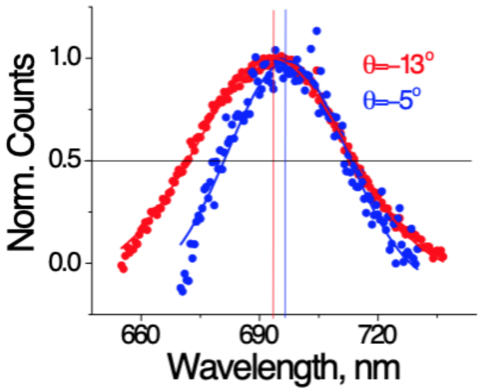

Figure 6.3 Comparison of normalized spectral curves at tilt angle of $\theta = -5°$ (close to emission minima) and at $\theta = -13°$ (close to the emission maxima) clearly exhibiting line broadening of FWHM from ca 32.3 to 41.5 nm. The solid lines are Gaussian fits to the curves. The peak shift was -4±0.3 nm

as a function of V_{ds}, as $V_{ds}(x)$=(V_d-V_s)(x/L) where L is the channel length. In general one may identify three effects: (1) the effect of the gate capacitor, C_g; the channel is considered as 'electrically doped'. (2) The effect of the ionized QD on the local gate bias via its own capacitor C_{QD}; the channel is further 'electrically doped'. (3) The effect of the local surface potential of the graphene guide itself. The latter is positive if the drain voltage, $V_d>0$; it is negative if $V_d<0$. Photo-excitation has two effects: (1) excitation of a dipole within the QD. The dipole is polarized by the gate bias similarly to artificial dielectrics and the overall effect is to increase C_g and hence the 'doping' of the graphene channel (see Figure 6.2). (2) Excitation of electrons within the graphene. The QDs have a shell barrier (ZnS) and are coated with a polymer (octadecylamine) to prevent agglomeration while in suspension and therefore, a direct contact between the QD and the graphene is less likely. In cases where the dot is in close proximity to the channel, then the probability of electron tunneling from the QD to the graphene may be written as, $\sim exp[-2d'_{B}(\Phi_b - eV)^{1/2}]$ where d'_{B} is the equivalent barrier width between graphene and QD, Φ_b is the barrier height, V=$V_{ds}(x)$ -V_g (the negative sign of Vg is due to the its sign at the graphene surface) and e is the electronic charge. Overall, tunneling negates the effect of charge polarization at the QD which is contrary to our experiments.

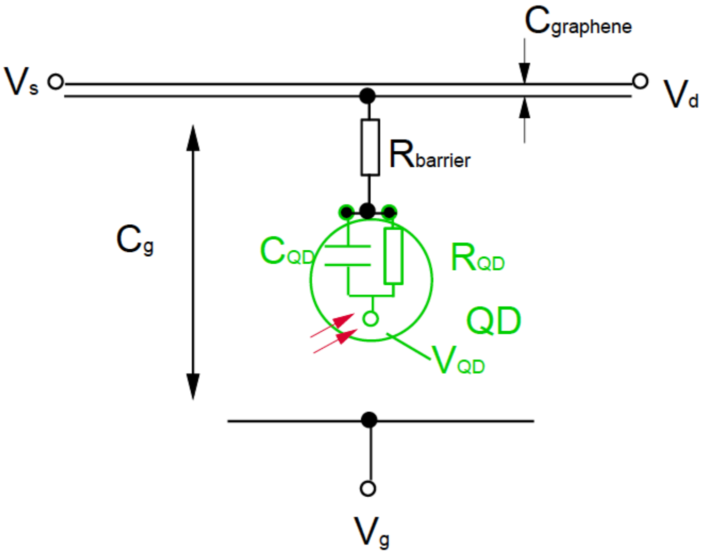

Figure 6.4 A circuit model that illustrates the various effects on the graphene channel. The source, V_s is typically grounded. C_g is the capacitor between the gate and the graphene channel; as the gate bias becomes more positive, the graphene guide becomes more negative (or more n-doped). C_{QD} is the equivalent dot capacitor (whose polarization negates that of the C_g) and R_g is the equivalent dot resistor (which is quite large). $R_{barrier}$ is the resistance between the dot and the graphene channel.

The effect of bias on the thicker oxide is shown in Figure 6.5.

Finally, we studied the FL as a function of V_{gs} at two tilt angles (namely, at on- and off-resonance with respect to the hole-array, Figure 6.6). At off-resonance, the FL exhibited a monotonous decline of overall 5% as a function of V_{gs}, whereas it was flat and reverse course at resonance conditions. Similar trend was found for FL vs V_{ds}, which suggests that graphene lost its conductance characteristics at large local fields due to the standing mode at emission wavelength.

6.6 Coupling to Surface Modes

The electromagnetic surface modes were bound on one side by the low index of perforated alumina/SiO$_2$ layer ($n_{Al_2O_3/SiO_2}$ ~2) at the sample's bottom, and a 250

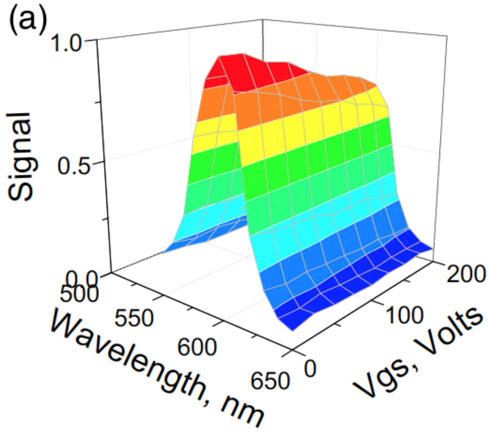

Figure 6.5 The effect of bias on QD interfaced graphene on a 150 nm thick oxide. (a) FL as a function of V_{gs}; (b) FL as a function of V_{ds}.

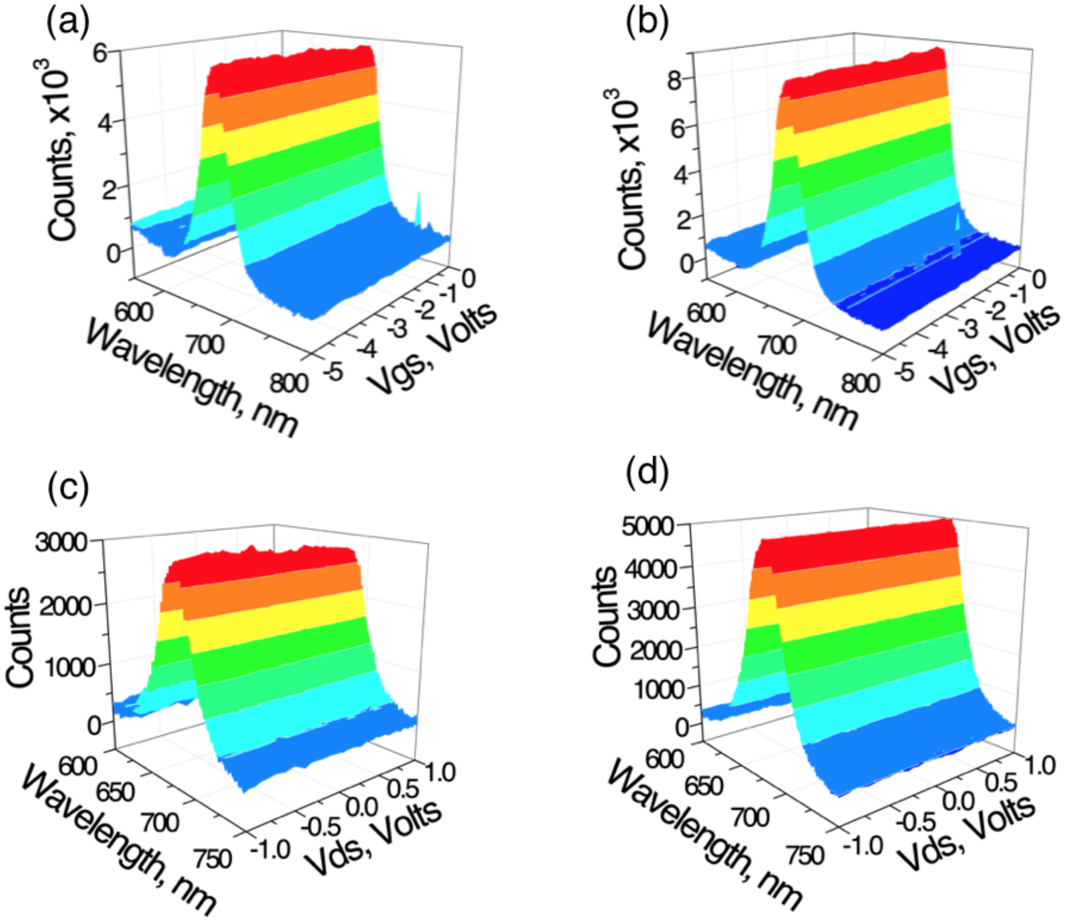

Figure 6.6 (a,b) FL as a function of V_{gs} (V_{ds}=0.3V) and (c,d) as a function of V_{ds} (V_{gs}=-5 V), at off-resonance (tilt at $\theta = 0°$) and at on-resonance (tilt at $\theta = -15°$), respectively. In (a,c), the FL change between minima and maxima is 5%±0.7%. In (c), there are two symmetric peaks at V_{ds}=±0.5V.

nm polymer/air layer from the sample's top (n_{air} ~1.15). An approximation for the refractive index of graphene may be taken as, $n_{\mathrm{graphene}} \sim 2.6 - 1.3i$ [29]. The electromagnetic radiation may be efficiently coupled into a surface mode when the wavevector of either the incident, or the scattered (or both) waves are at resonance with the wavevector of the perforated substrate [26]. Since the array pitch is smaller than the wavelength, a surface mode may become a standing wave, as well. The positions of the QDs are in-phase with the standing electromagnetic surface modes, resulting in an enhanced luminescence effect (Figure 6.7).

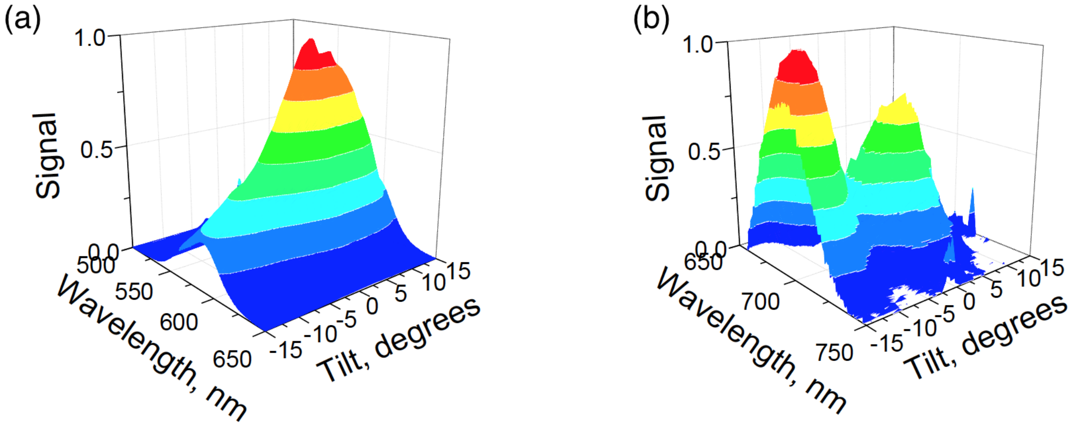

Figure 6.7 Fluorescence as a function of tilt angle. (a) For 590-nm QD. (b) For 670-nm QD. Note that the zero may be established at mid-point between the two symmetrical peaks. Thus, the peak tilt angle is situated at $\theta \sim \pm 2^\circ$ for (a) and at $\theta \sim \pm 10^\circ$ for (b).

The optimal launching conditions for a surface mode are achieved by a small tilt and in-plane rotation of the perforated substrate with respect to the p-polarized incident beam (The incident beam was polarized such that it had a polarization component perpendicularly to the sample's surface, or, consequently within the plane of incidence). Note that the array pitch is much smaller than the propagating wavelength and a bound surface mode is utilizing every other or even larger number of hole-planes. The tilt angle θ may be computed similarly to [50] as,

$$\sin(\theta) = \frac{\lambda_0}{a}\sqrt{(\frac{4}{3})({q_1}^2 - q_1 q_2 + {q_2}^2)} - n_{\mathrm{eff}} \tag{6.1}$$

where λ_0 is the incident or emitted wavelength, a is the pitch for the holes array ($a \sim 100\text{nm}$), q_1 and q_2 are sub-integers (e.g., 1/3) representing the ratio between the array pitch and the wavelength.

First, we note that the equation cannot be fulfilled for the pump wavelength of 532 nm and n_{eff} ~2.2 (which takes into account the refractive index of the graphene on the perforated alumina). Therefore, the peaks in Figure 6.7 may only be attributed to the resonance effect of the emission wavelengths. Upon tilting the sample, there are two symmetric peaks as per (1) and their mid-point is the true zero tilting point. The FL peak(s) in Figure 6.7a can be attributed to q_1=1/3, q_2=0 whereas, the peak(s) for Figure 6.7b may be attributed to q_1=1/3, q_2=1/4. Further proof of resonance condition is given in Section 6.5: The linewidth of the emitted radiation is seen to be clearly broaden and shifted at resonance conditions.

As a reference experiment, we measured QDs on a flat glass slide (not shown). Unlike Figure 6.7, the FL signal decreased monotonically as a function of the tilt angle: while the flat substrate is tilted, the illuminated area is increased and the intensity per area is decreased as $cos(\theta)$, leading to reduction in the overall FL signal.

Figure 6.8 shows the electrical and fluorescence (FL) data as a function of V_{ds} at V_{gs}=0 V (Figure 6.8a) and as a function of V_{gs} at V_{ds}=1 V (Figure 6.8b). The fluorescence monotonously decreased as a function of increasing V_{ds}. It also decreased as a function of increasing V_{gs} for this limited range of V_{gs}. Similar results were obtained for a thicker substrate as shown in Section 6.5. Most puzzling is the effect induced by V_{ds}. As we show in section 6.5, when the sample is at resonance with the optical surface mode then there seems to be no dependence of the fluorescence on either V_{ds} or V_{gs}. In the following, we attempt to explain these results by the effect of the various capacitors involved in the process.

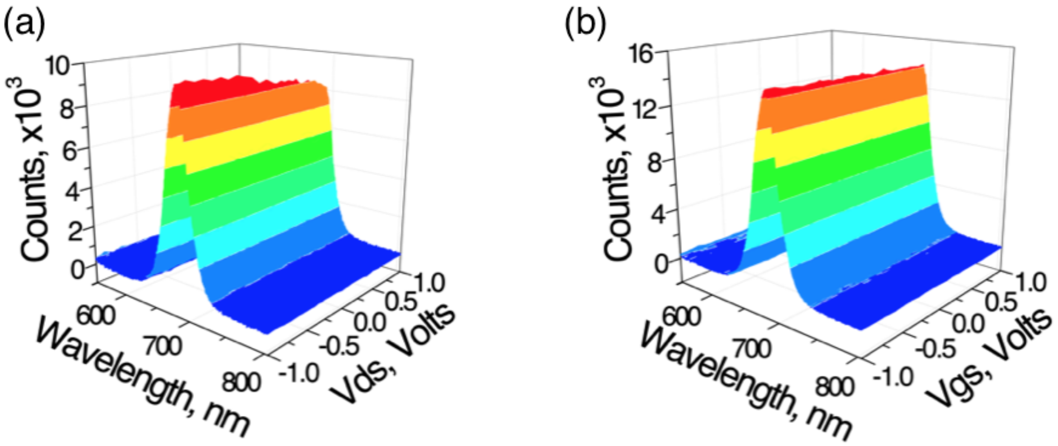

Figure 6.8 (a) FL as a function of V_{ds} at V_{gs}=0 V and normal incident angle, $\theta = 0°$. (b) FL as a function of V_{gs} at V_{ds}=1 V and normal incident angle, $\theta = 0°$. The oxide was 20 nm thick (hence, the relatively lower values for V_{gs}.

6.6.1 Dependence on V_{gs}

From Figure 6.7, it is clear that the graphene channel became even more n-type under uniform laser illumination at low laser intensity; the Dirac point has further shifted towards the negative V_{gs} values. This could suggest that actual transfer of carriers from the QD 'doped' the graphene. We note though that a positive gate bias polarizes the excited electrons in the QD away from the surface and hence the probability of electron tunneling (as opposed to hole tunneling) is substantially reduced. If at all, the graphene would have been p-doped [76].

When considering a dipole, such as the QD near the graphene channel, the key parameter is the ratio between the QD's diameter, d_0, to the distance of its surface from the graphene channel, d_B. For example, assume that the graphene behaves as an infinite metallic-like surface versus a small dot of radius d_0. Also assume that the dot can be replaced by a dipole of size d_0. The attraction energy between the dot's charge, Z_{QD} and its fictitious image is [55], $U_1 \approx -Z_{QD}Z_{QD} \cdot d_0/4d_B(d_B + d_0)$. If the dot diameter is much larger than d_{B} then the attraction energy behaves as $1/d_{\mathrm{B}}$. Similarly to conditional artificial dielectrics [49], these excited QD dipoles increase the gate-to-graphene capacitance and the result is a further 'doping' of the graphene channel. The induced charges are not diffused throughout the entire graphene channel but are more localized within a homas-Fermi distance of $Z_{\mathrm{QD}} \cdot d_{\mathrm{B}}$ [37]. This means that the charge density witin this localized area is rather large.

6.6.2 Dependence on $\mathbf{V_{ds}}$

The surface potential of the graphene varies linearly along the channel. Specifically, $V_{\mathrm{ds}}(x) \sim (x/L) \cdot (V_{\mathrm{d}} - V_{\mathrm{s}})$; here L is the channel length, x is any point along the channel in this quasi 1D model (the equivalent circuit model see Figure 6.4). If the graphene is treated as a single resistive layer, then a positive local surface bias counters the effect of a positive gate bias on the QDs and effectively de-polarizes QDs - this is not what we observe. If on the other hand, we treat the graphene as a capacitor with a self-capacitance of $\mu F/cm^2$, then positive $\mathrm{V_{ds}}$ injects positive charges to one layer of this capacitor and the other layer interfacing the gate further the impact of the gate bias. Thus, positive $\mathrm{V_{gs}}$ and $\mathrm{V_{ds}}$ values negatively dope the graphene and suppress the fluorescence via screening. Finally, we observed that when the emission radiation is at resonance with the porous substrate its signal was unaffected by the electrical bias (shown in Section 6.5). FRET is crucially depending on the life-time of the donors (QD in our case) which ought to be longer than the acceptor channel (the excited e-h pairs in the graphene). Specifically, $k_{\mathrm{FRET}} = 1/\tau_{\mathrm{DA}} - 1/\tau_{\mathrm{D}}$, where τ_{DA} and τ_{D} are the life-time of the donor-acceptor route and the fluorescence of a stand-alone donor's route, respectively. Increasing the emission rate for the QD, at resonance with the substrate hinders the energy transfer of energy to the graphene and increased fluorescence. Actual carrier transfer would not be affected by such resonance considerations at the emission frequencies.

The effect of leakage current has been assessed; it has been found that I_{ds} as a function of V_{gs} in the range of [-5,5] V at V_{ds}=0 V was at least a factor of 10 smaller (or on the order of 0.1 nA) than the current level at V_{ds}=0.01 V (which was on the order of nA).

6.7 Conclusion

In summary, by using graphene as an optical and electrical surface guide in an FET construction, and by coupling the graphene channels with commensurate, yet individual quantum semiconductor dot array, we have demonstrated a unique electro-photonic structure which may find applications in communication and sensing systems.

CHAPTER 7

LIFE-TIME AND LINE-WIDTH OF INDIVIDUAL QUANTUM DOTS INTERFACED WITH GRAPHENE

In this chapter, we report on the luminescence life-time and line-width from an array of individual quantum dots, interfaced with graphene surface guide and dispersed on a metal film. Our results are consistent with screening by charge carriers. Many use fluorescence quenching as a sign of interfacing the chromophore with a conductive surface; we found that QD interfaced with conductive layer exhibited shorter life-time and line-broadening but not necessarily fluorescence quenching as the latter may be impacted by molecular concentration, reflectivity and conductor imperfections.

Quenching of fluorescence in the vicinity of conductors is well documented [122], [16]. The growing interest in graphene has extended the study of fluorescence-quenching to this unique film [26, 29, 31, 37, 75, 92, 138]. Fluorescence quenching by graphene has been attributed by some to a physical transfer of electrons from the fluorophores to the graphene [31, 75, 92], similar to n-type doping in semiconductors. A different point of view was given in [29]; the energy transfer between a Quantum Dot (QD) and graphene was attributed to FRET (fluorescence resonance energy transfer, which could be enabled through screening by free-carriers in the graphene film). These theories do not fully explain the fluorescence quenching because near the Dirac point such screening is linearly diminishing [26] and the screening, if it exists, should be non-linear and dependent on the amount of charge placed within a small distance away from the graphene [37, 138]. Molecular concentration for each independently measured surface, as well as the local conductivity of the conductor are at issue. If fluorescence quenching is due to energy transfer between the chromophore and dipoles in the conductive film, then an increase in the density-of-states for such a radiation outlet is the ultimate proof. Large density-of-states results in shorter life-times and broadening of the fluorescence line [125].

We study isolated QDs: screening by relatively thick QD films and charge coupling between nearby dots may mask the local interaction with the conductor. In order to isolate the QDs from one another we placed each one of them in holes formed in anodized aluminum oxide (AAO) films. The properties of graphene on periodic and porous substrates, such as AAO have been studied in conjunction with Surface Enhanced Raman (SERS) [8, 10] and Surface Plasmon Polariton (SPP) lasers [11, 84, 85]. The graphene is partially suspended over the substrate pores. For the energy transfer between the chromophore and graphene to be effective, the characteristic parameter $\alpha = e^2/(\epsilon\hbar\nu_{\mathrm{F}})$ ought to be larger than 1 with ϵ, the dielectric constant of the vacuum [37]. Also, the absorption of graphene (~2.3% per layer) ought to be compatible to, or even larger than the ~3% absorption of the CdSe/ZnS QD monolayer so that the film of dots will not screen itself [80]. We set to measure life-times and spectral linewidths of QDs interfaced with graphene and with an aluminum film. QDs embedded in a bare AAO hole-array was used as a reference.

7.1 Surface Modes

We concentrate here on surface modes in the AAO regions because the periodic structure provides us with an effective way of coupling between them and the radiation modes. This coupling may affect the luminescence intensity as measured by a far-field detector and even its life-time constants. Electromagnetic surface modes along the periodic structures were bound here on one side by the effective low index of perforated alumina on the SiO_2 layer ($n_{\mathrm{Al_2O_3/SiO_2}} \sim 2$) at the sample's bottom. On the other side of the graphene surface guide, the mode was bound by the low index of either air, or a combination of 200 nm polymer/air layer ($n_{\mathrm{air/polymer}} \sim 1.15$) where the polymer was a remnant of the graphene transfer process. In calculating the effective indices, we used the relative thicknesses of the various films. An approximation for the refractive index of graphene surface guide may make use of $\varepsilon(\omega) = \varepsilon_\mathrm{b} + i\sigma_0/\omega d$: here ε_b=$5.8\varepsilon_0$ as the effective dielectric constant for graphene with a background material [50] and d=3.38 Angstroms for the effective graphene thickness.

Electromagnetic radiation may be efficiently coupled with a surface mode when the wavevector of either the incident, or scattered (or both) waves are at resonance with the wavevector of the perforated substrate [84]. Since the array pitch is smaller than the wavelength, a surface mode may become a standing wave, as well. The positions of the QDs are in-phase with the standing electromagnetic surface modes, resulting in enhanced luminescence (Figure 7.1).

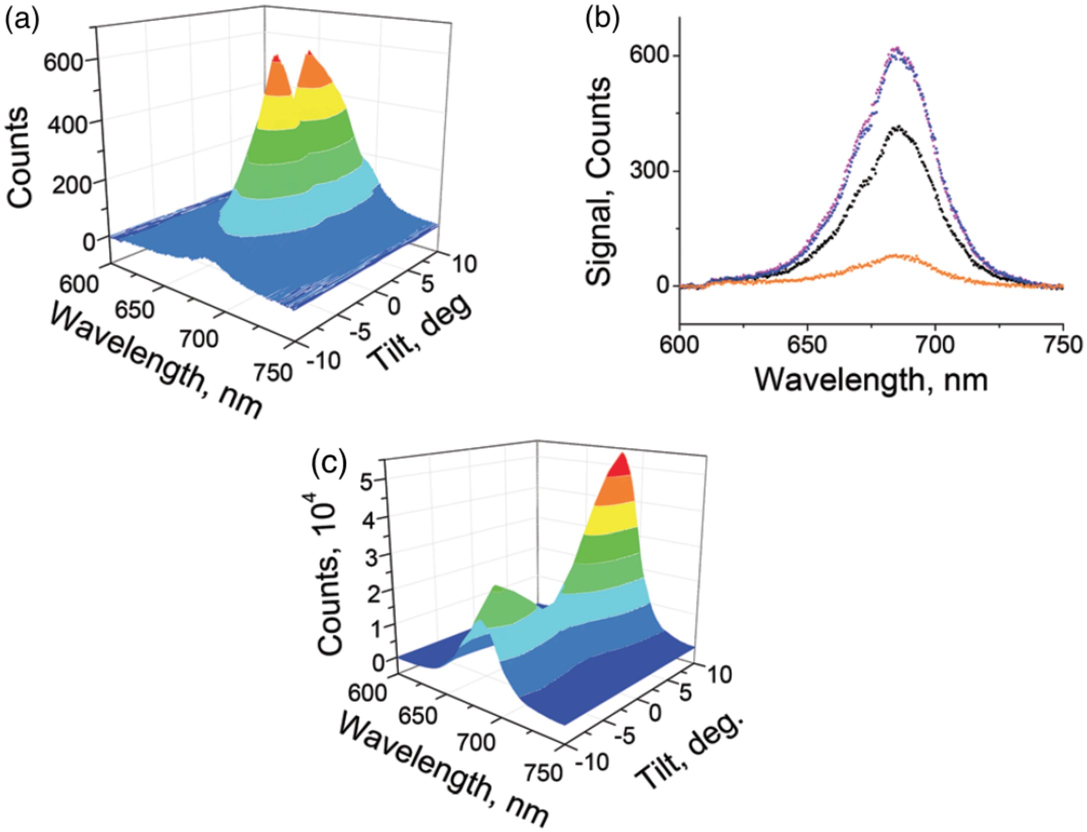

Figure 7.1 (a) Fluorescence of QD690 embedded in a graphene covered AAO hole array with a pitch of ca. 90 nm. (b) A few curves at some specific tilt angles - no meaningful change in the linewidths as a function of tilt angle has been noted. (c) Fluorescence of QD690 embedded in bare AAO.

The tilt angle θ may be computed similarly to [138] as,

$$\sin(\theta) = \frac{\lambda_0}{a}\sqrt{(\frac{4}{3})({q_1}^2 - q_1 q_2 + {q_2}^2)} - n_{\text{eff}} \tag{7.1}$$

where λ_0 is the incident or emitted wavelength, a is the pitch for the hole array ($a \sim$ 90 nm), q_1 and q_2 are sub-integers (e.g., 1/3) representing the ratio between the array pitch and the propagating wavelength. Equation 7.1 cannot be fulfilled for a pump wavelength of 488 nm and n_{eff} ~2.4 for the graphene guide in the range of tilt angles of $-8° < \theta < 8°$. Therefore, the fluorescence peaks in Figure 7.1 ought to be attributed to the resonances at only emission wavelengths. Upon tilting the sample, there are two symmetric peaks in the fluorescence emission as per equation 7.1 at ca. ±2°.

For the QDs embedded in bare AAO, the position of the FL peaks has changed to ca. ±8° (Figure 7.1c). This is consistent with equation 7.1; in the absence of graphene, the effective refractive index has reduced, and the angle that satisfies equation 7.1 becomes larger.

7.2 Results and Discussion

The successful transfer of graphene to the QD loaded AAO hole array was confirmed by measuring the Raman spectrum of the graphene as shown in Figure 7.2. The spectrum was recorded at normal incidence. The relatively small 2D line could be attributed in part to the diminishing quantum efficiency of the Si-based CCD array. In general, the lines have been somewhat blue shifted [118] and could point to the effect of the hole-array.

The photoluminescence life-time measurements were first conducted at normal incidence. Within the measurement error, no substantial change in the emission linewidth was noted as a function of tilt angle (Figure 7.3b). The data have been fitted with three time-constants, which fell into three categories: $\tau_1 < 1$ ns; $\tau_2 \sim 1$ ns and $\tau_3 \sim 10$ ns. In order to ensure the quality of the fit, the adjusted or standard

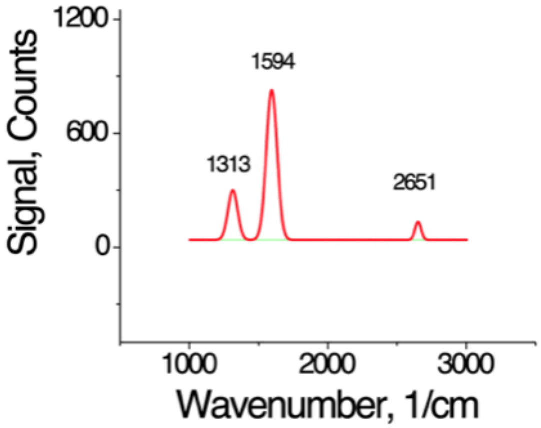

Figure 7.2 Raman spectrum of graphene, interfaced with QDs. Data were taken with 11.5 mW 785 nm laser and an ×50 LF objective. The small 2D peak is attributed to relatively large defect line at 1313 1/cm (due to contact with the QDs) and the low detector efficiency at that long wavelength (2700 1/cm translates to ∼ 950 nm Stokes line).

Table 7.1 Transition Values on Electrode, in AAO Hole-array Covered with Graphene and in Bare AAO Hole-array.

	on electrode	in AAO/graphene	in bare AAO
b	8.7±1.4	2.56±0.07	1.18±0.04
c	0.78±0.04	0.38±0.012	0.22±0.007
d	0.10±0.001	0.07±0.001	0.06±0.001

R^2 value has to be near 1 and the residuals have to be symmetrical. The very short lifetime (of the order of 200 ps) is similar to laser pulse duration and hence could be identified as a system response or a stimulated effect. The very long time constant (of the order of 10 ns) is typical of QDs albeit it is a bit shorter compared to the literature [39] and our own data on glass. Its amplitude was typically half of the medium lifetime constant (of the order of 1 ns). We attribute the latter to the coupling of the radiation mode to the structured substrate (see below on the local energy density and its impact on the radiation lifetime). These lifetime constants correspond to transition rates b, c, and d (Figure 7.3 and Table 7.1).

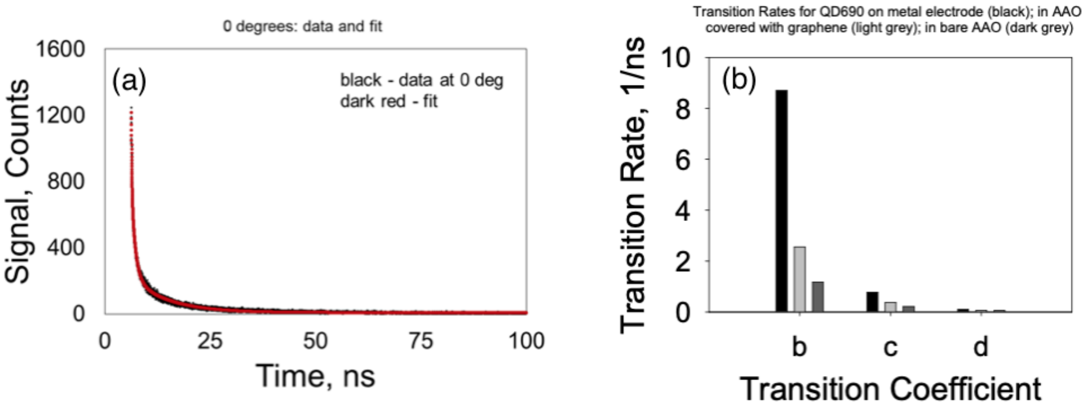

Figure 7.3 (a) A typical temporal data and its fit at normal incidence (tilt angle, 0°). (b) Various transition rates for QDs: on electrode (black) in AAO hole-array covered with graphene (light grey) and in bare AAO hole-array. The longest life-time was measured for QD embedded in bare AAO where the shortest one was obtained for QD on the aluminum electrode. The table 7.1 provides with the transition values in $1/\text{ns}^{-1}$. The transition values for QDs on the metal are associated with the larger luminescence signal of Figure 7.4b. The values for the 'quenched' case (Figure 7.4a) are respectively, $\text{b}=2.58/\text{ns}^{-1}$; $\text{c}=0.37/\text{ns}^{-1}$ and $\text{d}=0.07/\text{ns}^{-1}$; they are comparable to the graphene values but larger than the values for QDs embedded in bare AAO.

As noted in [67, 97], the local density of states may be modified by the immediate environment at the chromophore. Thus, our concept of quenching may well be determined by unknown molecular concentration and layer conductivity and the properties of the surface mode. Two examples are shown below: (a) a large transition rates (Figure 7.4b) which also portrayed unusual large luminesce; (b) a 'quenched' luminescence (Figures 7.4a and 7.3) which was associated with smaller transition rates. The metal films were not perfect. 'Quenched' signals were typically obtained for QDs on a smooth metal environment. 'Enhanced' signals were typically obtained from relatively rough metal surfaces. The enhanced signals cannot be attributed to QDs situated at distances larger than the Förster length, because as the chromophores are placed away from the quenching layer, their related lifetimes should become longer (and not shorter, as observed here) when compared to their quenched signal counterparts [65]. Thus, these two cases represent uncertainties in the local QD environment. The QDs interfaced with conductive surfaces such as

Table 7.2 Linewidths and Peaks for QDs on Electrode, in AAO/Graphene and Covered with Graphene in the 'Quenched' case.

width(nm)	on Al electrode	peak(nm)	in AAO/graphene	peak(nm)	in bare AAO	peak(nm)
w1	50.1±0.51	675.36	39.63±0.20	680.26	37.98±0.17	682.6
w2	25.07±0.25	686.72	19.85±0.27	686.98	18.47±0.22	787.75

Table 7.3 Linewidths and Peaks for QDs on Electrode, in AAO/Graphene and Covered with Graphene in the 'Enhanced' case.

width(nm)	on Al electrode	peak(nm)	in AAO/graphene	peak(nm)	in bare AAO	peak(nm)
w1	39.99±0.10	683.17	39.63±0.20	680.26	37.98±0.17	682.6
w2	20.58±0.10	687.62	19.85±0.27	686.98	18.47±0.22	787.75

graphene and metal do exhibit overall shorter emission lifetimes when compared to their non-interfaced counterpart.

Complementary experiments were conducted on the line broadening of the fluorescence emission (Figure 7.4). The spectrum was fitted with two Gaussian peaks whose position and width are provided by the accompanying table. Within the measurement error, no substantial change in the emission linewidth was noted as a function of tilt angle (Figure 7.1b). However, as will be seen below, there is a marked change in the related emission lifetimes. One may observe two cases measured for two spots on the aluminum electrode: the one shown in Figure 7.4a is a 'quenched' case, whereas the one shown in Figure 7.4b is an 'enhanced' case. The fluorescence intensity was quenched as expected when the QDs were interfaced with the graphene or the aluminum electrode. This was accompanied by a clear linewidth broadening but its relative emission rates are smaller than the 'enhanced' case. We point out that the linewidth of the QDs is masked by an inhomogeneous broadening, attributed to size dispersion.

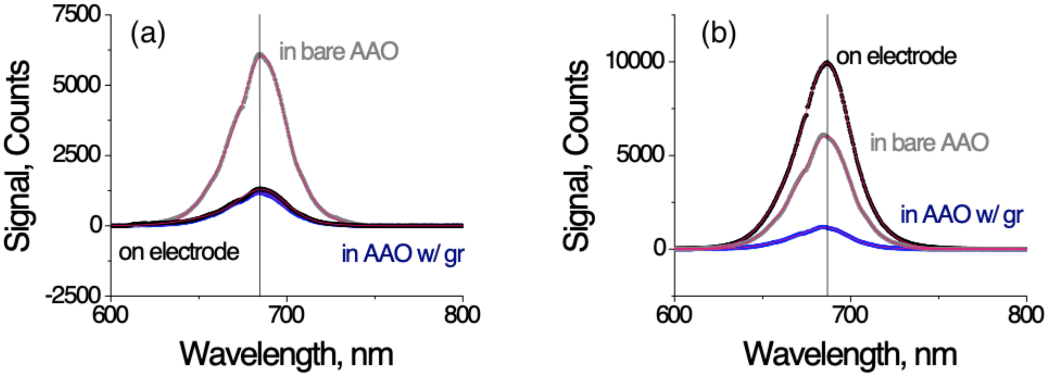

Figure 7.4 (a) Linewidth of luminescence by QDs on aluminum electrode, in AAO hole-array covered with graphene and in bare AAO hole-array. Quenching of the fluorescence by the graphene and metal is clearly seen. The linewidths for QDs on the electrode or covered with graphene is wider than for QDs imbedded in bare AAO holes. Table 7.2 and Table 7.3 summarizes the results. Molecular concentration might be an issue when dealing with luminescence quenching as shown in (b) QDs on a 'hot' metal spot exhibited a much larger signal than the other two cases; nevertheless, the lines widths were respectively, ca 40 nm and 20.6 nm, still larger than the width of QDs in bare AAO. The corresponding life-time constants were shorter, as well (Table 7.1).

Most puzzling is the increase in the emission photon life-time for QDs interfaced with graphene at tilt angles that seem to be associated with resonance coupling between the surface and the emission modes. In Figure 7.5, we show the various rate coefficients as a function of tilt angle. One expects that when at resonance, the measured emission would exhibit a shorter lifetime due to an increase in the density of states of its surface modes [124]. Similar experiments with QDs in bare AAO yielded much smaller luminescence changes (less than 3% in the transition coefficients compared with a larger than 10% change for the luminescence of the QDs interfaced with graphene coated AAO) and therefore deemed inconclusive. Nevertheless, coupling to the radiation modes is strong as observed in Figure 7.1c.

Fermi's Golden rule relates the transition rate of the QDs to the final density of states at the emission frequency. In principle, the emission from a QD may be funneled through several radiation venues (waveguide modes, resonance modes, surface modes, etc.,) each of which has a different local, or global density-of-states (DOS). These

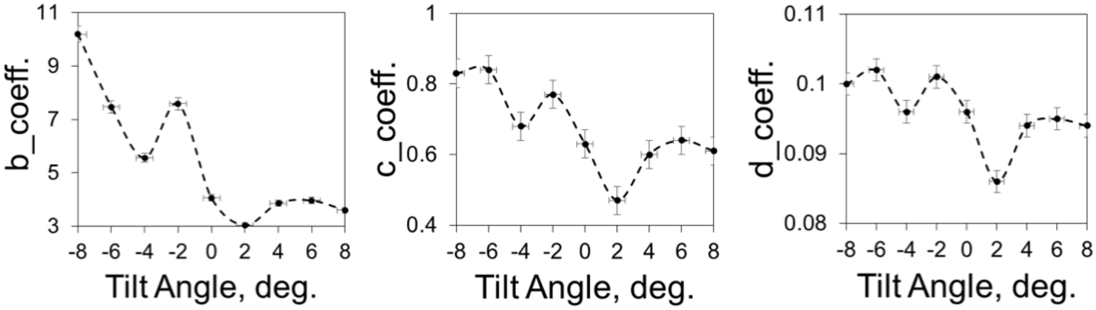

Figure 7.5 The rate coefficients as a function of tilt angle. Close to resonance coupling, these coefficients are at the minimum (suggesting longer photon time). While there are variations due to local imperfections, the trend, as judged by the coefficients on either side of the minimum is nonetheless clear. The connecting dash curves are only guide to the eye.

venues are not necessarily coupled together and their density-of-states may not be simply summed up as was done in [62]; the photon has a finite probability to decay via each of these outlets. By tilting the sample, we captured a subset of these venues, e.g., decay through a collective surface guiding mode, whose density of states is smaller than the one that was measured at off-resonance [25]. Specifically, the DOS for a two-dimensional propagating surface guide is proportional to the radial frequency, ω, whereas the DOS for a three-dimensional free space radiation mode is proportional to ω^2. Thus, in principle, at off-resonance conditions, the emission from a single QD emitter may couple to a larger density of states pool, and therefore exhibits a shorter life-time. As stated before, inhomogeneous line broadening as a result of QD size dispersion may have obscured linewidth effects as a function of tilt. This issue, requires further studies.

7.3 Summary

In summary, we measured the lifetime and linewidth for QDs on an aluminum electrode, in an AAO hole array interfaced with graphene and compared it with the QDs embedded in a bare AAO hole array. Indeed, the QDs interfaced with conductive films portrayed shorter lifetime and line-broadening but not necessarily fluorescence quenching.

CHAPTER 8

CONCLUSION

Photo-induced properties of well separated QDs, interfaced with graphene channels in FET devices have been investigated in this dissertation. SEM, Raman spectroscopy fluorescence and electrical characterization methods were used in this study. The transfer characteristics of the graphene channel in FET were obtained by the probe electric measurement station under different level of illuminations. The photoluminescence property of the GFET device was assessed with confocal laser system. Surface modes and surface plasmon/polariton (SPP) modes were interrogated by a small tilt and in-plane rotation of the perforated substrate with respect to the polarized incident beam.

In the microelectronics fields, the exceptional properties of graphene continue to hold high promise for various applications. Graphene-based transistor have the advantage of rapid response, high sensitivity, and low-cost. Besides, the nanoscale channel will empower testing multiple targets with ultra-fast speed by arranging thousands of GETs on one small chip. Overall, graphene-based transistors have the potential to replace the silicon sensors in many areas ranging from drug discovery and chemical detection applications to the electrical logic systems. Here we added another dimension to these applications - the optoelectronic dimension - by interfacing the high fluorescing QD with graphene channels. Biochemical detection may be enhanced by the present studies.

In order to transition the GFET from research labs to the commercial market, more effort need to be devoted to explaining the fundamental physics and mechanics behind the behavior of the devices. Although some significant progress has been made in the fabrication and application of graphene-based devices, there are still various challenges ahead of us. Various device architectures, gate material and structures should be taken into consideration. The effect of number of the graphene layers and surface defects need to be further investigated. A good model will also help to bridge the differences between the theoretical expectation and the experimental data.

In this dissertation, the electrical and optical properties of a new graphene-based transistor structure were investigated. The mechanism behind the interaction between the graphene channels and the distributed QDs requires further exploration and research. Some future studies are summarized here:

- Measurements of GFET at various sizes in order to explore size-dependent behavior (especially, lateral channel width).
- To further understand the interaction between the QDs and graphene, spectral photoconductivity should be undertaken.
- Simulations will elucidate the interaction between the QDs and the graphene channel under various bias conditions.
- Other graphene derivatives may be used as a replacement of the channel material, such as graphene oxide and reduced graphene oxide.
- Other functional composites such as graphene/bio conjugates may be investigated.

APPENDIX

CROSSLIGHT APSYS SIMULATION RESULTS

In this appendix, Crosslight APSYS, a semiconductor device simulation software was used to simulate the optoelectronic properties of graphene channel interfaced with with an array of QDs.

A 2-D model of single quantum dot was built with the APSYS software and the electron wavefunction of one QD obtained with the wave equation solver, as shown in Figure A.1. In the figure, the rectangular section from 0 to 0.005 μm is used to define a 5nm InGaAs quantum dot, and the surrounding material is set as air ($\sim$ 95 nm)

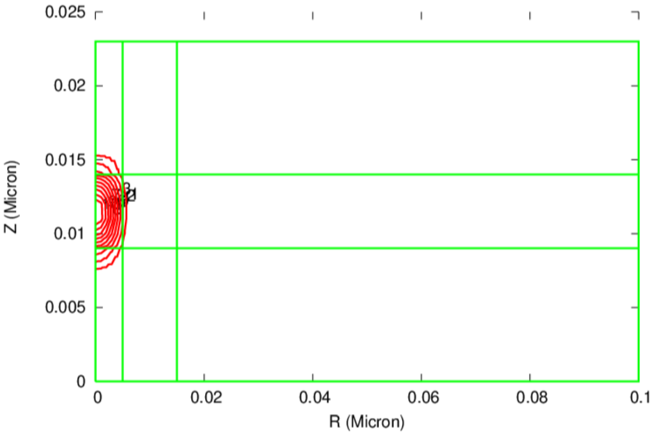

Figure A.1 Cross section of a ground state wavefunction of one QD surrounded by air.

Figure A.2 shows the energy band diagram of a layer, which is made of an array of QDs without graphene (Figure A.2a) and the band diagram of the same array QDs when in contact with the graphene channel (Figure A.2b). The thickness of the QD layer is about 10 nm. The pitch of the QD array is 100 nm and each QD is surrounded by a $\sim$ 3 nm QD ligand. Air layers were placed below and above the QDs. The graphene was simulated as a 0.3 nm thick metal.

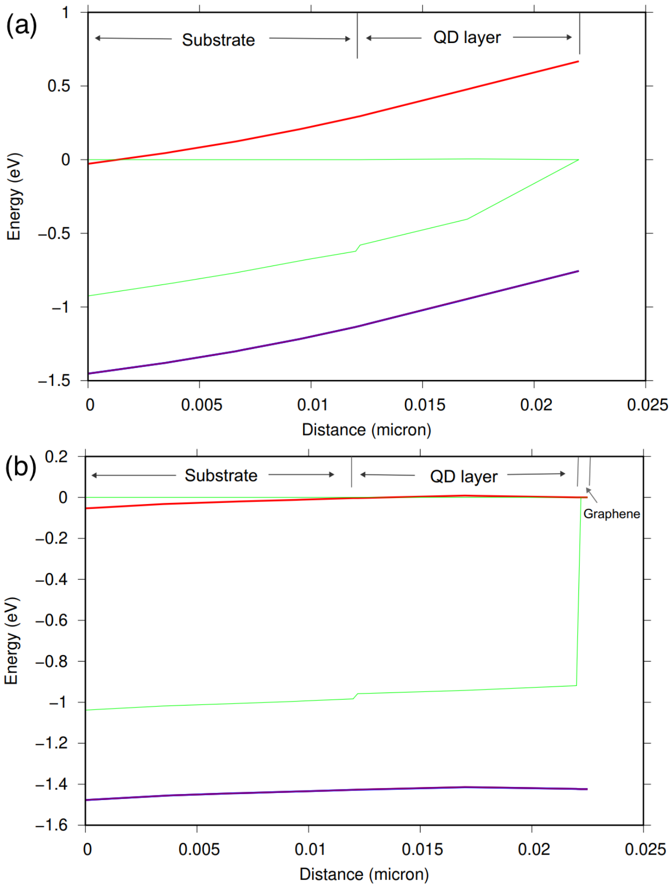

Figure A.2 (a) Band diagram of the QD layer. (b) band diagram of isolated QDs in contact with graphene sheet. The diagram shows the conduction band on top (red) and valence band at the bottom (purple) along with electron/hole quasi-Fermi levels in Green.

The simulated Shockley-Read-Hall (SRH) recombination rate, which is related to the lifetime is shown in Figure A.3. Contrary to experiment, the presence of graphene does not seem to have an effect in the model, probably because the radiation and non-radiation components cannot be separated by the software.

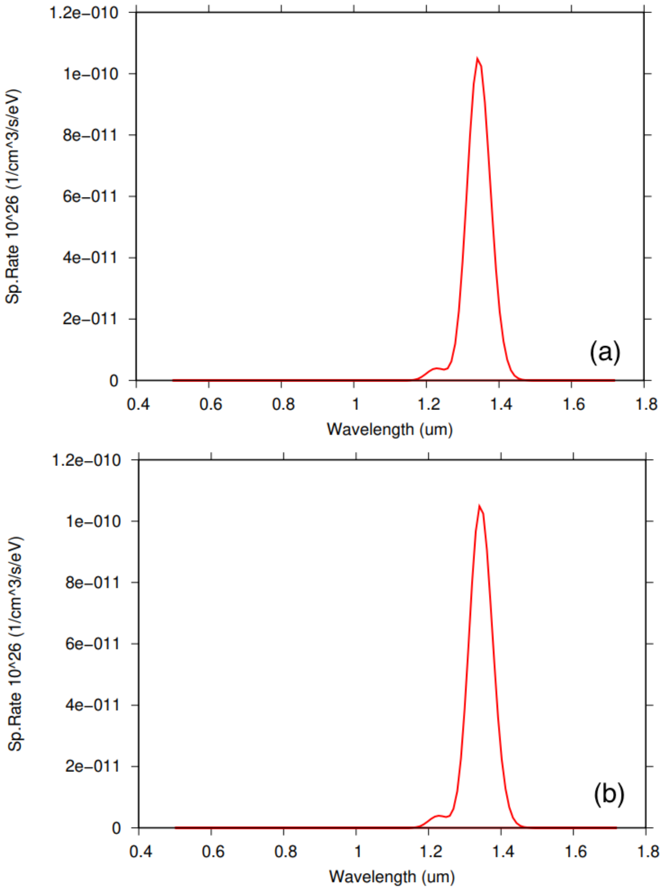

Figure A.3 (a) The simulated SRH recombination rate of QDs and (b) The simulated SRH rate of QDs interfaced with graphene. No apparent change is recorded in the two cases which is due to the limitation of the software.

BIBLIOGRAPHY

[1] A. P. Alivisatos, W. Gu, and C. Larabell. Quantum dots as cellular probes. *Annual Review of Biomedical Engineering*, 7(1):55–76, August 2005. PMID: 16004566.

[2] V. Alzari, D. Nuvoli, S. Scognamillo, M. Piccinini, E. Gioffredi, G. Malucelli, S. Marceddu, M. Sechi, V. Sanna, and A. Mariani. Graphene-containing thermoresponsive nanocomposite hydrogels of poly(n-isopropylacrylamide) prepared by frontal polymerization. *Journal of Materials Chemistry*, 21:8727–8733, May 2011.

[3] P. O. Anikeeva, J. E. Halpert, M. G. Bawendi, and V. Bulović. Quantum dot light-emitting devices with electroluminescence tunable over the entire visible spectrum. *Nano Letters*, 9(7):2532–2536, June 2009. PMID: 19514711.

[4] R. C. Ashoori. Electrons in artificial atoms. *Nature*, 379(6564):413–419, February 1996.

[5] S. Bae, H. Kim, Y. Lee, X. Xu, J. S. Park, Y. Zheng, J. Balakrishnan, T. Lei, H. Ri Kim, Y. Il Song, Y. J. Kim, K. S. Kim, B. Özyilmaz, J. H. Ahn, B. H. Hong, and S. Iijima. Roll-to-roll production of 30-inch graphene films for transparent electrodes. *Nature Nanotechnology*, 5:574–578, June 2010.

[6] A. A. Balandin, S. Ghosh, W. Bao, I. Calizo, D. Teweldebrhan, F. Miao, and C. N. Lau. Superior thermal conductivity of single-layer graphene. *Nano Letters*, 8(3):902–907, March 2008.

[7] B. Ballou, B. C. Lagerholm, L. A. Ernst, M. P. Bruchez, and A. S. Waggoner. Noninvasive imaging of quantum dots in mice. *Bioconjugate Chemistry*, 15(1):79–86, January 2004. PMID: 14733586.

[8] A. Banerjee and H. Grebel. Depositing graphene films on solid and perforated substrates. *Nanotechnology*, 19(36):365303, July 2008.

[9] A. Banerjee and H. Grebel. Nonlinear behavior of vibrating molecules on suspended graphene waveguides. *Optics Letters*, 38(2):226–228, January 2013.

[10] A. Banerjee, R. Li, and H. Grebel. Raman spectroscopy with graphenated anodized aluminum oxide substrates. *Nanotechnology*, 20(29):295502, July 2009.

[11] A. Banerjee, R. Li, and H. Grebel. Surface plasmon lasers with quantum dots as gain media. *Applied Physics Letters*, 95(25):251106, December 2009.

[12] Q. Bao and K. P. Loh. Graphene photonics, plasmonics, and broadband optoelectronic devices. *ACS Nano*, 6(5):3677–3694, May 2012. PMID: 22512399.

[13] Q. Bao, H. Zhang, B. Wang, Z. Ni, C. H. Y. X. Lim, Y. Wang, D. Y. Tang, and K. P. Loh. Broadband graphene polarizer. *Nature Photonics*, 5:411–415, May 2011.

[14] Q. Bao, H. Zhang, Y. Wang, Z. Ni, Y. Yan, Z. X. Shen, K. P. Loh, and D. Y. Tang. Atomiclayer graphene as a saturable absorber for ultrafast pulsed lasers. *Advanced Functional Materials*, 19(19):3077–3083, October 2009.

[15] J. H. Bardarson, M. Titov, and P. W. Brouwer. Electrostatic confinement of electrons in an integrable graphene quantum dot. *Physical Review Letters*, 102:226803, June 2009.

[16] W. L. Barnes. Fluorescence near interfaces: The role of photonic mode density. *Journal of Modern Optics*, 45(4):661–699, July 1998.

[17] V. Berry. Impermeability of graphene and its applications. *Carbon*, 62:1 – 10, October 2013.

[18] P. Blake, E. W. Hill, A. H. Castro Neto, K. S. Novoselov, D. Jiang, R. Yang, T. J. Booth, and A. K. Geim. Making graphene visible. *Applied Physics Letters*, 91(6):063124, August 2007.

[19] U. Bockelmann and G. Bastard. Phonon scattering and energy relaxation in two-, one-, and zero-dimensional electron gases. *Physical Review B*, 42:8947–8951, November 1990.

[20] A. Bostwick, T. Ohta, J. L. McChesney, K. V. Emtsev, T. Seyller, K. Horn, and E. Rotenberg. Symmetry breaking in few layer graphene films. *New Journal of Physics*, 9(10):385–385, October 2007.

[21] L. E. Brus. Electron-electron and electronhole interactions in small semiconductor crystallites: The size dependence of the lowest excited electronic state. *The Journal of Chemical Physics*, 80(9):4403–4409, August 1984.

[22] J. Cai, P. Ruffieux, R. Jaafar, M. Bieri, T. Braun, S. Blankenburg, M. Muoth, A. P. Seitsonen, M. Saleh, X. Feng, K. Müllen, and R. Fasel. Atomically precise bottom-up fabrication of graphene nanoribbons. *Nature*, 466:470–473, July 2010.

[23] A. Calogeracos and N. Dombey. History and physics of the klein paradox. *Contemporary Physics*, 40(5):313–321, November 1999.

[24] J. M. Caruge, J. E. Halpert, V. Wood, V. Bulović, and M. G. Bawendi. Colloidal quantum-dot light-emitting diodes with metal-oxide charge transport layers. *Nature Photonics*, 2:247–250, March 2008.

[25] E. V. Castro, K. S. Novoselov, S. V. Morozov, N. M. R. Peres, J. M. B. L. dos Santos, J. Nilsson, F. Guinea, A. K. Geim, and A. H. C. Neto. Biased bilayer graphene: Semiconductor with a gap tunable by the electric field effect. *Physical Review Letters*, 99:216802, November 2007.

[26] A. H. Castro Neto, F. Guinea, N. M. R. Peres, K. S. Novoselov, and A. K. Geim. The electronic properties of graphene. *Reviews of Modern Physics*, 81:109–162, January 2009.

[27] A. Chakrabarti, J. Lu, J. C. Skrabutenas, T. Xu, Z. Xiao, J. A. Maguire, and N. S. Hosmane. Conversion of carbon dioxide to few-layer graphene. *Journal of Materials Chemistry*, 21:9491–9493, June 2011.

[28] W. C.W Chan Chan, D. J Maxwell, X. Gao, R. E. Bailey, M. Han, and S. Nie. Luminescent quantum dots for multiplexed biological detection and imaging. *Current Opinion in Biotechnology*, 13(1):40 – 46, February 2002.

[29] Z. Chen, S. Berciaud, C. Nuckolls, T. F. Heinz, and L. E. Brus. Energy transfer from individual semiconductor nanocrystals to graphene. *ACS Nano*, 4(5):2964–2968, May 2010. PMID: 20402475.

[30] J. L. Cheng, N. Vermeulen, and J. E. Sipe. Third order optical nonlinearity of graphene. *New Journal of Physics*, 16(5):053014, May 2014.

[31] H. Dong, W. Gao, F. Yan, H. Ji, and H. Ju. Fluorescence resonance energy transfer between quantum dots and graphene oxide for sensing biomolecules. *Analytical Chemistry*, 82(13):5511–5517, July 2010. PMID: 20524633.

[32] L. X. Dong and Q. Chen. Properties, synthesis, and characterization of graphene. *Frontiers of Materials Science in China*, 4(1):45–51, March 2010.

[33] S. Dwarakanath, J. G. Bruno, A. Shastry, T. Phillips, A. John, A. Kumar, and L. D. Stephenson. Quantum dot-antibody and aptamer conjugates shift fluorescence upon binding bacteria. *Biochemical and Biophysical Research Communications*, 325(3):739 – 743, December 2004.

[34] A.I. Ekimov, Al.L. Efros, and A.A. Onushchenko. Quantum size effect in semiconductor microcrystals. *Solid State Communications*, 56(11):921 – 924, December 1985.

[35] J. Farlow, D. Seo, K. E Broaders, M. J Taylor, Z. J. Gartner, and Y. W. Jun. Formation of targeted monovalent quantum dots by steric exclusion. *Nature Methods*, 10:1203–1205, October 2013.

[36] A. C. Ferrari, J. C. Meyer, V. Scardaci, C. Casiraghi, M. Lazzeri, F. Mauri, S. Piscanec, D. Jiang, K. S. Novoselov, S. Roth, and A. K. Geim. Raman spectrum of graphene and graphene layers. *Physical Review Letters*, 97:187401, October 2006.

[37] M. M. Fogler, D. S. Novikov, and B. I. Shklovskii. Screening of a hypercritical charge in graphene. *Physical Review B*, 76:233402, December 2007.

[38] A. Fu, W. Gu, C. Larabell, and A. P. Alivisatos. Semiconductor nanocrystals for biological imaging. *Current Opinion in Neurobiology*, 15(5):568 – 575, October 2005.

[39] A. Gaigalas, P. Derose, L. Wang, and Y.-Z. Zhang. Optical properties of cdse/zns nanocrystals. *Journal of research of the National Institute of Standards and Technology*, 119:610–628, December 2014.

[40] N. R. Gall, E. V. Rut'kov, and A. Y. Tontegode. Influence of surface carbon on the formation of silicon-refractory metal interfaces. *Thin Solid Films*, 266(2):229 – 233, October 1995.

[41] N. R. Gall, E. V. Rut'kov, and A. Ya. Tontegode. Two dimensional graphite films on metals and their intercalation. *International Journal of Modern Physics B*, 11(16):1865–1911, June 1997.

[42] C. Galup-Montoro and M. C. Schneider. *Mosfet Modeling for Circuit Analysis and Design*. Singapore, Singapore: World Scientific, February 2007.

[43] L. Gao, W. Ren, F. Li, and H. M. Cheng. Total color difference for rapid and accurate identification of graphene. *ACS Nano*, 2(8):1625–1633, August 2008. PMID: 19206365.

[44] A. K. Geim and K. S. Novoselov. The rise of graphene. *Nature Materials*, 6:183–191, March 2007.

[45] G. Giovannetti, P. A. Khomyakov, G. Brocks, P. J. Kelly, and J. van den Brink. Substrate-induced band gap in graphene on hexagonal boron nitride: Ab initio density functional calculations. *Physical Review B*, 76:073103, August 2007.

[46] M. M. Glazov and S. D. Ganichev. High frequency electric field induced nonlinear effects in graphene. *Physics Reports*, 535(3):101 – 138, February 2014.

[47] L. Gomez De Arco, Y. Zhang, C. W. Schlenker, K. Ryu, M. E. Thompson, and C. Zhou. Continuous, highly flexible, and transparent graphene films by chemical vapor deposition for organic photovoltaics. *ACS Nano*, 4(5):2865–2873, May 2010. PMID: 20394355.

[48] D. Granados and J. M. Garca. In(ga)as self-assembled quantum ring formation by molecular beam epitaxy. *Applied Physics Letters*, 82(15):2401–2403, April 2003.

[49] H. Grebel. Surface-enhanced raman scattering: phenomenological approach. *Journal of the Optical Society of America B*, 21(2):429–435, February 2004.

[50] H. Grebel. *Structured Surfaces as Optical Metamaterials*. Cambridge, UK: Cambridge University Press, June 2011.

[51] H. Grebel. Surface plasmon lasers. *Proceeding SPIE*, 7922:7922–7922–11, February 2011.

[52] H. Grebel, L. Stan, A. V. Sumant, Y. Liu, D. Gosztola, L. Ocola, and B. Fisher. Transfer of graphene with protective oxide layers. *ChemEngineering*, 2(4), December 2018.

[53] F. Guo, G. Silverberg, S. Bowers, S. Kim, D. Datta, V. Shenoy, and R. H. Hurt. Graphene-based environmental barriers. *Environmental Science and Technology*, 46(14):7717–7724, July 2012.

[54] A. Gupta, G. Chen, P. Joshi, S. Tadigadapa, and Eklund. Raman scattering from high-frequency phonons in supported n-graphene layer films. *Nano Letters*, 6(12):2667–2673, December 2006. PMID: 17163685.

[55] H. Han, S. Vijayalakshmi, A. Lan, Z. Iqbal, H. Grebel, E. Lalanne, and A. M. Johnson. Linear and nonlinear optical properties of single-walled carbon nanotubes within an ordered array of nanosized silica spheres. *Applied Physics Letters*, 82(9):1458–1460, February 2003.

[56] M. Y. Han, B. Ozyilmaz, Y. Zhang, and P. Kim. Energy band-gap engineering of graphene nanoribbons. *Physical Review Letters*, 98:206805, May 2007.

[57] S. J. Han, K. A. Jenkins, A. Valdes Garcia, A. D. Franklin, A. A. Bol, and W. Haensch. High-frequency graphene voltage amplifier. *Nano Letters*, 11(9):3690–3693, September 2011. PMID: 21805988.

[58] Q. He, S. Wu, Z. Yin, and H. Zhang. Graphene-based electronic sensors. *Chemical Science*, 3:1764–1772, May 2012.

[59] E. Hendry, P. J. Hale, J. Moger, A. K. Savchenko, and S. A. Mikhailov. Coherent nonlinear optical response of graphene. *Physical Review Letters*, 105:097401, August 2010.

[60] Y. Hernandez, V. Nicolosi, M. Lotya, F. M. Blighe, Z. Sun, S. De, I. T. McGovern, B. Holland, M. Byrne, Y. K. Gun'Ko, J. J. Boland, P. Niraj, G. Duesberg, S. Krishnamurthy, R. Goodhue, J. Hutchison, V. Scardaci, A. C. Ferrari, and J. N. Coleman. High-yield production of graphene by liquid-phase exfoliation of graphite. *Nature Nanotechnology*, 3:563–568, August 2008.

[61] C. Hwang, D. A. Siegel, S. Mo, W. Regan, A. Ismach, Y. Zhang, A. Zettl, and A. Lanzara. Fermi velocity engineering in graphene by substrate modification. *Scientific Reports*, 2:590, August 2012.

[62] E. H. Hwang and S. Das Sarma. Dielectric function, screening, and plasmons in two-dimensional graphene. *Physical Review B*, 75:205418, May 2007.

[63] C. Itzykson and J. B. Zuber. *Quantum Field Theory*. Dover Books on Physics. Mineola, NY: Dover Publications, June 2006.

[64] M. Jablan, H. Buljan, and M. Soljačić. Plasmonics in graphene at infrared frequencies. *Physical Review B*, 80, December 2009.

[65] S. Jander, A. Kornowski, and H. Weller. Energy transfer from cdse/cds nanorods to amorphous carbon. *Nano Letters*, 11(12):5179–5183, December 2011. PMID: 22017456.

[66] G. Jo, S. Na, S.-H. Oh, S. Lee, T.-S. Kim, G. Wang, M. Choe, W. Park, J. Yoon, D.-Y. Kim, Y. H. Kahng, and T. Lee. Tuning of a graphene-electrode work function to enhance the efficiency of organic bulk heterojunction photovoltaic cells with an inverted structure. *Applied Physics Letters*, 97(21):213301, November 2010.

[67] K. Joulain, R. Carminati, J. P. Mulet, and J. J. Greffet. Definition and measurement of the local density of electromagnetic states close to an interface. *Physical Review B*, 68:245405, December 2003.

[68] C. R. Kagan, E. Lifshitz, E. H. Sargent, and D. V. Talapin. Building devices from colloidal quantum dots. *Science*, 353(6302), August 2016.

[69] P. V. Kamat. Quantum dot solar cells. semiconductor nanocrystals as light harvesters. *The Journal of Physical Chemistry C*, 112(48):18737–18753, October 2008.

[70] M. I. Katsnelson. Minimal conductivity in bilayer graphene. *European Physical Journal B*, 52(2):151–153, July 2006.

[71] M. I. Katsnelson and K. S. Novoselov. Graphene: New bridge between condensed matter physics and quantum electrodynamics. *Solid State Communications*, 143(1):3 – 13, July 2007.

[72] D. Y. Kim, S. Sinha-Ray, J. J. Park, J. G. Lee, Y. H. Cha, S. H. Bae, J. H. Ahn, Y. C. Jung, S. M. Kim, A. L. Yarin, and S. S. Yoon. Self-healing reduced graphene oxide films by supersonic kinetic spraying. *Advanced Functional Materials*, 24(31):4986–4995, May 2014.

[73] K. Kim, J. Choi, T. Kim, S. H. Cho, and H. J. Chung. A role for graphene in silicon-based semiconductor devices. *Nature*, 479:338–344, November 2011.

[74] K. S. Kim, Y. Zhao, H. Jang, S. Y. Lee, J. M. Kim, K. S. Kim, J. H. Ahn, P. Kim, J. Y. Choi, and B. H. Hong. Large-scale pattern growth of graphene films for stretchable transparent electrodes. *Nature*, 457:706–710, January 2009.

[75] A. V. Klekachev, M. Cantoro, M. H. van der Veen, A. L. Stesmans, M. M. Heyns, and S. De Gendt. Electron accumulation in graphene by interaction with optically excited quantum dots. *Physica E Low-Dimensional Systems and Nanostructures*, 43(5):1046–1049, March 2011.

[76] G. Konstantatos, M. Badioli, L. Gaudreau, J. Osmond, M. Bernechea, F. P. G. de Arquer, F. Gatti, and F. H. L. Koppens. Hybrid graphene–quantum dot phototransistors with ultrahigh gain. *Nature Nanotechnology*, 7:363–368, May 2012.

[77] F. H. L. Koppens, D. E. Chang, and F. J. García de Abajo. Graphene plasmonics: A platform for strong light–matter interactions. *Nano Letters*, 11(8):3370–3377, July 2011. PMID: 21766812.

[78] F. V. Kusmartsev, W. M. Wu, M. P. Pierpoint, and K. C. Yung. Application of graphene within optoelectronic devices and transistors. *Applied Spectroscopy and the Science of Nanomaterials*, pages 191–221, October 2014.

[79] J. R. Lakowicz. *Principles of Fluorescence Spectroscopy.* NYC, New York: Springer US, 3rd edition, March 2011.

[80] C. A. Leatherdale, W. K. Woo, F. V. Mikulec, and M. G. Bawendi. On the absorption cross section of cdse nanocrystal quantum dots. *The Journal of Physical Chemistry B*, 106(31):7619–7622, August 2002.

[81] C. Lee, X. Wei, J. W. Kysar, and J. Hone. Measurement of the elastic properties and intrinsic strength of monolayer graphene. *Science*, 321(5887):385–388, July 2008.

[82] S. W. Lee, H. Grebel, A. K., and D. Lopez. Electrical and optical properties of carbon nanotube/polypyrrole addressable intra-connects. *Synthetic Metals*, 159(5):462 – 466, March 2009.

[83] S. W. Lee, A. Kornblit, D. Lopez, S. V. Rotkin, A. A. Sirenko, and H. Grebel. Negative differential resistance: Gate controlled and photoconductance enhancement in carbon nanotube intraconnects. *Nano Letters*, 9(4):1369–1373, April 2009. PMID: 19253997.

[84] R. Li, A. Banerjee, and H. Grebel. The possibility for surface plasmons lasers. *Optics Express*, 17(3):1622–1627, February 2009.

[85] R. Li and H. Grebel. Surface enhanced fluorescence (sef): Polarization characteristics. *Sensors Journal, IEEE*, 10:465 – 468, March 2010.

[86] X. Li, W. Cai, J. An, S. Kim, J. Nah, D. Yang, R. Piner, A. Velamakanni, I. Jung, E. Tutuc, S. K. Banerjee, L. Colombo, and R. S. Ruoff. Large-area synthesis of high-quality and uniform graphene films on copper foils. *Science*, 324(5932):1312–1314, June 2009.

[87] X. Li, C. W. Magnuson, A. Venugopal, R. M. Tromp, J. B. Hannon, E. M. Vogel, L. Colombo, and R. S. Ruoff. Large-area graphene single crystals grown by low-pressure chemical vapor deposition of methane on copper. *Journal of the American Chemical Society*, 133(9):2816–2819, March 2011. PMID: 21309560.

[88] X. Li, X. Wang, L. Zhang, S. Lee, and H. Dai. Chemically derived, ultrasmooth graphene nanoribbon semiconductors. *Science*, 319(5867):1229–1232, February 2008.

[89] X. Li, G. Zhang, X. Bai, X. Sun, X. Wang, E. Wang, and H. Dai. Highly conducting graphene sheets and langmuir–blodgett films. *Nature Nanotechnology*, 3:538–542, August 2008.

[90] X. Li, Y. Zhu, W. Cai, M. Borysiak, B. Han, D. Chen, R. D. Piner, L. Colombo, and R. S. Ruoff. Transfer of large-area graphene films for high-performance transparent conductive electrodes. *Nano Letters*, 9(12):4359–4363, December 2009. PMID: 19845330.

[91] X. Liang, Z. Fu, and S. Y. Chou. Graphene transistors fabricated via transfer-printing in device active-areas on large wafer. *Nano Letters*, 7(12):3840–3844, December 2007.

[92] W. Lin, B. Tian, P. Zhuang, J. Yin, C. Zhang, Q. Li, T Shih, and W. Cai. Graphene-based fluorescence-quenching-related fermi level elevation and electron-concentration surge. *Nano Letters*, 16(9):5737–5741, September 2016. PMID: 27513317.

[93] Y. M. Lin, C. Dimitrakopoulos, K. A. Jenkins, D. B. Farmer, H.-Y. Chiu, A. Grill, and Ph. Avouris. 100-ghz transistors from wafer-scale epitaxial graphene. *Science*, 327(5966):662–662, February 2010.

[94] Y. M. Lin, A. Valdes-Garcia, S. J. Han, D. B. Farmer, I. Meric, Y. Sun, Y. Wu, C. Dimitrakopoulos, A. Grill, P. Avouris, and K. A. Jenkins. Wafer-scale graphene integrated circuit. *Science*, 332(6035):1294–1297, June 2011.

[95] M. Liu, X. Yin, E. Ulin-Avila, B. Geng, T. Zentgraf, L. Ju, F. Wang, and X. Zhang. A graphene-based broadband optical modulator. *Nature*, 474:64–67, May 2011.

[96] C. H. Lu, H. H. Yang, C. L. Zhu, X. Chen, and G. N. Chen. A graphene platform for sensing biomolecules. *Angewandte Chemie International Edition*, 48(26):4785–4787, June 2009.

[97] P. Lunnemann and A. F. Koenderink. The local density of optical states of a metasurface. *Scientific Reports*, 6:20655, February 2016.

[98] S. Mahajan. *Encyclopedia of Materials: Science and Technology*, volume 10. Oxford, UK: Pergamon, October 2001.

[99] S. Mao, S. Cui, G. Lu, K. Yu, Z. Wen, and J. Chen. Tuning gas-sensing properties of reduced graphene oxide using tin oxide nanocrystals. *Journal of Materials Chemistry*, 22:11009–11013, April 2012.

[100] J. C. Meyer, A. K. Geim, M. I. Katsnelson, K. S. Novoselov, T. J. Booth, and S. Roth. The structure of suspended graphene sheets. *Nature*, 446:60–63, March 2007.

[101] X. Michalet, F. F. Pinaud, L. A. Bentolila, J. M. Tsay, S. Doose, J. J. Li, G. Sundaresan, A. M. Wu, S. S. Gambhir, and S. Weiss. Quantum dots for live cells, in vivo imaging, and diagnostics. *Science*, 307(5709):538–544, January 2005.

[102] J. Millman. *Electronic devices and circuits.* Number 384-385. Singapore, Singapore: McGraw Hill, January 1967.

[103] N. Mohanty and V. Berry. Graphene-based single-bacterium resolution biodevice and dna transistor: Interfacing graphene derivatives with nanoscale and microscale biocomponents. *Nano Letters*, 8(12):4469–4476, December 2008. PMID: 18983201.

[104] H. Montón, C. Nogués, E. Rossinyol, O. Castell, and M. Roldán. Qds versus alexa: reality of promising tools for immunocytochemistry. *Journal of Nanobiotechnology*, 7(1):4, May 2009.

[105] C. B. Murray, C. R. Kagan, and M. G. Bawendi. Synthesis and characterization of monodisperse nanocrystals and close-packed nanocrystal assemblies. *Annual Review of Materials Science*, 30(1):545–610, August 2000.

[106] R. R. Nair, P. Blake, A. N. Grigorenko, K. S. Novoselov, T. J. Booth, T. Stauber, N. M. R. Peres, and A. K. Geim. Fine structure constant defines visual transparency of graphene. *Science*, 320(5881):1308–1308, January 2008.

[107] T. R. Nayak, H. Andersen, V. S. Makam, C. Khaw, S. Bae, X. Xu, P. R. Ee, J. H. Ahn, B. H. Hong, G. Pastorin, and B. Özyilmaz. Graphene for controlled and accelerated osteogenic differentiation of human mesenchymal stem cells. *ACS Nano*, 5(6):4670–4678, June 2011. PMID: 21528849.

[108] Z. H. Ni, H. M. Wang, J. Kasim, H. M. Fan, T. Yu, Y. H. Wu, Y. P. Feng, and Z. X. Shen. Graphene thickness determination using reflection and contrast spectroscopy. *Nano Letters*, 7(9):2758–2763, September 2007. PMID: 17655269.

[109] K. S. Novoselov, V. I. Falko, L. Colombo, P. R. Gellert, M. G. Schwab, and K. Kim. A roadmap for graphene. *Nature*, 490:192–200, October 2012.

[110] K. S. Novoselov, A. K. Geim, S. V. Morozov, D. Jiang, Y. Zhang, S. V. Dubonos, I. V. Grigorieva, and A. A. Firsov. Electric field effect in atomically thin carbon films. *Science*, 306(5696):666–669, October 2004.

[111] A. J. Nozik, M. C. Beard, J. M. Luther, M. Law, R. J. Ellingson, and J. C. Johnson. Semiconductor quantum dots and quantum dot arrays and applications of multiple exciton generation to third-generation photovoltaic solar cells. *Chemical Reviews*, 110(11):6873–6890, November 2010. PMID: 20945911.

[112] D. Nuvoli, L. Valentini, V. Alzari, S. Scognamillo, S. B. Bon, M. Piccinini, J. Illescas, and A. Mariani. High concentration few-layer graphene sheets obtained by liquid phase exfoliation of graphite in ionic liquid. *Journal of Materials Chemistry*, 21:3428–3431, December 2011.

[113] T. Ohta, A. Bostwick, J. L. McChesney, T. Seyller, K. Horn, and E. Rotenberg. Interlayer interaction and electronic screening in multilayer graphene investigated with angle-resolved photoemission spectroscopy. *Physical Review Letters*, 98:206802, May 2007.

[114] T. Ohta, A. Bostwick, T. Seyller, K. Horn, and E. Rotenberg. Controlling the electronic structure of bilayer graphene. *Science*, 313(5789):951–954, August 2006.

[115] J. B. Oostinga, H. B. Heersche, X. Liu, A. F. Morpurgo, and L. M. K. Vandersypen. Gate-induced insulating state in bilayer graphene devices. *Nature Materials*, 7:151–157, December 2007.

[116] R. Osovsky, D. Cheskis, V. Kloper, A. Sashchiuk, M. Kroner, and E. Lifshitz. Continuous-wave pumping of multiexciton bands in the photoluminescence spectrum of a single cdte-cdse core-shell colloidal quantum dot. *Physical Review Letters*, 102:197401, May 2009.

[117] D. Pan, S. Wang, B. Zhao, M. Wu, H. Zhang, Y. Wang, and Z. Jiao. Li storage properties of disordered graphene nanosheets. *Chemistry of Materials*, 21(14):3136–3142, July 2009.

[118] C. Paraskevaidis, T. Kuykendall, M. Melli, A. Weber-Bargioni, P. J. Schuck, A. Schwartzberg, S. Dhuey, S. Cabrini, and H. Grebel. Gain and raman line-broadening with graphene coated diamond-shape nano-antennas. *Nanoscale*, 7:15321–15331, August 2015.

[119] R. E. Peierls. Bemerkungen über umwandlungstemperaturen. *Helvetica Physica Acta*, 7:81–83, 1934.

[120] J. Peña-Bahamonde, H. N. Nguyen, S. K. Fanourakis, and D. F. Rodrigues. Recent advances in graphene-based biosensor technology with applications in life sciences. *Journal of Nanobiotechnology*, 16(1):75, September 2018.

[121] F. Perreault, A. Fonseca de Faria, and M. Elimelech. Environmental applications of graphene-based nanomaterials. *Chemical Society Reviews*, 44:5861–5896, March 2015.

[122] B. N. J. Persson and N. D. Lang. Electron-hole-pair quenching of excited states near a metal. *Physical Review B*, 26:5409–5415, November 1982.

[123] L. A. Ponomarenko, F. Schedin, M. I. Katsnelson, R. Yang, E. W. Hill, K. S. Novoselov, and A. K. Geim. Chaotic dirac billiard in graphene quantum dots. *Science*, 320(5874):356–358, April 2008.

[124] E. M. Purcell. Spontaneous emission probabilities at radio frequencies. *Physical Review*, 69:681, June 1946.

[125] E. M. Purcell, H. C. Torrey, and R. V. Pound. Resonance absorption by nuclear magnetic moments in a solid. *Physical Review*, 69:37–38, January 1946.

[126] J. Rafiee, X. Mi, H. Gullapalli, A. V. Thomas, F. Yavari, Y. Shi, P. M. Ajayan, and N. A. Koratkar. Wetting transparency of graphene. *Nature Materials*, 11:217–222, January 2012.

[127] N. Ray, S. Shallcross, S. Hensel, and O. Pankratov. Buffer layer limited conductivity in epitaxial graphene on the si face of sic. *Physical Review B*, 86:125426, September 2012.

[128] A. Reina, X. Jia, J. Ho, D. Nezich, H. Son, V. Bulovic, M. S. Dresselhaus, and J. Kong. Large area, few-layer graphene films on arbitrary substrates by chemical vapor deposition. *Nano Letters*, 9(1):30–35, January 2009. PMID: 19046078.

[129] X. Ren, C. Chen, M. Nagatsu, and X. Wang. Carbon nanotubes as adsorbents in environmental pollution management: A review. *Chemical Engineering Journal*, 170(2):395 – 410, June 2011.

[130] U. Resch-Genger, M. Grabolle, S. Cavaliere, R. Nitschke, and T. Nann. Quantum dots versus organic dyes as fluorescent labels. *Nature methods*, 5:763–75, October 2008.

[131] D. Rodrigo, O. Limaj, D. Janner, D. Etezadi, F. J. García de Abajo, V. Pruneri, and H. Altug. Mid-infrared plasmonic biosensing with graphene. *Science*, 349(6244):165–168, July 2015.

[132] B. Román-Manso, E. Domingues, F. M. Figueiredo, M. Belmonte, and P. Miranzo. Enhanced electrical conductivity of silicon carbide ceramics by addition of graphene nanoplatelets. *Journal of the European Ceramic Society*, 35(10):2723 – 2731, September 2015.

[133] M. Sabaeian and A. Khaledi-Nasab. Size-dependent intersubband optical properties of dome-shaped inas/gaas quantum dots with wetting layer. *Applied Optics*, 51(18):4176–4185, June 2012.

[134] V. C. Sanchez, A. Jachak, R. H. Hurt, and A. B. Kane. Biological interactions of graphene-family nanomaterials: An interdisciplinary review. *Chemical Research in Toxicology*, 25(1):15–34, January 2012. PMID: 21954945.

[135] F. Schedin, A. K. Geim, S. V. Morozov, E. W. Hill, P. Blake, M. I. Katsnelson, and K. S. Novoselov. Detection of individual gas molecules adsorbed on graphene. *Nature Materials*, 6:652–655, July 2007.

[136] F. Schwierz. Graphene transistors. *Nature Nanotechnology*, 5:487–496, May 2010.

[137] B. Sensale, T. Fang, R. Yan, M. M. Kelly, D. Jena, L. Liu, and H. Xing. Unique prospects for graphene-based terahertz modulators. *Applied Physics Letters*, 99:113104, September 2011.

[138] K. W. K. Shung. Dielectric function and plasmon structure of stage-1 intercalated graphite. *Physical Review B*, 34:979–993, July 1986.

[139] R. Sitko, B. Zawisza, and E. Malicka. Graphene as a new sorbent in analytical chemistry. *TrAC Trends in Analytical Chemistry*, 51:33 – 43, November 2013.

[140] E. A. De Souza, M. C. Nuss, W. H. Knox, and D. A. B. Miller. Wavelength-division multiplexing with femtosecond pulses. *Optics Letters*, 20(10):1166–1168, May 1995.

[141] C. Stampfer, S. Fringes, J. Güttinger, F. Molitor, C. Volk, B. Terrés, J. Dauber, S. Engels, S. Schnez, A. Jacobsen, S. Dröscher, T. Ihn, and K. Ensslin. Transport in graphene nanostructures. *Frontiers of Physics*, 6(3):271–293, September 2011.

[142] M. D. Stoller, S. Park, Y. Zhu, J. An, and R. S. Ruoff. Graphene-based ultracapacitors. *Nano Letters*, 8(10):3498–3502, October 2008.

[143] L. Sun, J. J. Choi, D. Stachnik, A. C. Bartnik, B. R. Hyun, G. G. Malliaras, T. Hanrath, and F. W. Wise. Bright infrared quantum-dot light-emitting diodes through inter-dot spacing control. *Nature Nanotechnology*, 7:369–373, May 2012.

[144] P. Sutter. How silicon leaves the scene. *Nature Materials*, 8:171–172, March 2009.

[145] D. V. Talapin, J. S. Lee, M. V. Kovalenko, and E. V. Shevchenko. Prospects of colloidal nanocrystals for electronic and optoelectronic applications. *Chemical Reviews*, 110(1):389–458, January 2010. PMID: 19958036.

[146] P. Tassin, T. Koschny, and C. M. Soukoulis. Graphene for terahertz applications. *Science*, 341(6146):620–621, August 2013.

[147] S. A. Thiele, J. A. Schaefer, and F. Schwierz. Modeling of graphene metal-oxide-semiconductor field-effect transistors with gapless large-area graphene channels. *Journal of Applied Physics*, 107(9):094505, May 2010.

[148] S. Trivedi and H. Grebel. Field-effect transistors with graphene channels and quantum dots: Gate control and photo-induced effects. In *2011 11th IEEE International Conference on Nanotechnology*, pages 1584–1587, August 2011.

[149] V. C. Tung, M. J. Allen, Y. Yang, and R. B. Kaner. High-throughput solution processing of large-scale graphene. *Nature Nanotechnology*, 4:25–29, November 2008.

[150] N. Varghese, U. Mogera, A. Govindaraj, A. Das, P. K. Maiti, A. K. Sood, and C. N. R. Rao. Binding of dna nucleobases and nucleosides with graphene. *ChemPhysChem*, 10(1):206–210, January 2009.

[151] P. R. Wallace. The band theory of graphite. *Physical Review*, 71:622–634, May 1947.

[152] F. Wang, Y. Zhang, C. Tian, C. Girit, A. Zettl, M. Crommie, and Y. R. Shen. Gate-variable optical transitions in graphene. *Science*, 320(5873):206–209, April 2008.

[153] H. Wang, A. Hsu, J. Kong, D. A. Antoniadis, and T. Palacios. Compact virtual-source current-voltage model for top- and back-gated graphene field-effect transistors. *IEEE Transactions on Electron Devices*, 58(5):1523–1533, May 2011.

[154] Y. Wang, S. W. Tong, X. F. Xu, B. Özyilmaz, and K. P. Loh. Interface engineering of layer-by-layer stacked graphene anodes for high-performance organic solar cells. *Advanced Materials*, 23(13):1514–1518, January 2011.

[155] Y. Y. Wang, Z. H. Ni, T. Yu, Z. X. Shen, H. M. Wang, Y. H. Wu, W. Chen, and A. T. Shen Wee. Raman studies of monolayer graphene: The substrate effect. *The Journal of Physical Chemistry C*, 112(29):10637–10640, July 2008.

[156] D. Wei, Y.i Liu, Y. Wang, H. Zhang, L. Huang, and G. Yu. Synthesis of n-doped graphene by chemical vapor deposition and its electrical properties. *Nano Letters*, 9(5):1752–1758, May 2009. PMID: 19326921.

[157] Z. Wu and Z Ni. Spectroscopic investigation of defects in two-dimensional materials. *Nanophotonics*, 6(6):1219–1237, April 2017.

[158] F. Xia, T. Mueller, Y. M. Lin, A. Valdes-Garcia, and P. Avouris. Ultrafast graphene photodetector. *Nature Nanotechnology*, 4:839–843, October 2009.

[159] Y. Xu, K. Sheng, C. Li, and G. Shi. Self-assembled graphene hydrogel via a one-step hydrothermal process. *ACS Nano*, 4(7):4324–4330, July 2010. PMID: 20590149.

[160] Y. Zhang, J. P. Small, M. E. S. Amori, and P. Kim. Electric field modulation of galvanomagnetic properties of mesoscopic graphite. *Physical Review Letters*, 94:176803, May 2005.

[161] Y. Zhang, Y. W. Tan, H. L Stormer, and P. Kim. Experimental observation of the quantum hall effect and berry's phase in graphene. *Nature*, 438:201–4, December 2005.

[162] S. Y. Zhou, G. H. Gweon, J. Graf, A. V. Fedorov, C. D. Spataru, R. D. Diehl, Y. Kopelevich, D. H. Lee, Steven G. Louie, and A. Lanzara. First direct observation of dirac fermions in graphite. *Nature Physics*, 2:595–599, August 2006.

[163] Y. Zhu, S. Murali, M. D. Stoller, A. Velamakanni, R. D. Piner, and R. S. Ruoff. Microwave assisted exfoliation and reduction of graphite oxide for ultracapacitors. *Carbon*, 48(7):2118 – 2122, June 2010.